PROCEEDINGS
OF THE
INTERNATIONAL SCHOOL OF PHYSICS
Enrico Fermi

Lectures on Pulsed NMR

(2nd Edition)

L. Emsley and A. Pines

PROCEEDINGS
OF THE
INTERNATIONAL SCHOOL OF PHYSICS
Enrico Fermi

Lectures on Pulsed NMR

(2nd Edition)

L. Emsley and A. Pines

The Authors

Alex Pines is widely considered the most influential figure in solid state NMR spectroscopy. He grew up in Southern Rhodesia (now Zimbabwe). He studied mathematics and chemistry at the Hebrew University of Jerusalem in 1968 and a PhD in chemical physics at MIT in 1972. Pines joined the faculty at Berkeley the same year and awarded tenure in 1975.

In his graduate work Pines demonstrated the surprising time reversal of spin diffusion in many-body dipole-dipole systems, and his technique of proton-enhanced cross polarization for dilute spins such as ^{13}C in solids launched in the modern era of high-resolution solid-state NMR in chemistry.

Pines' further contributions include multiple-quantum spectroscopy, icosahedral double magic-angle spinning for quadrupolar nuclei, zero-field NMR, demonstration of Berry's phase, and remote detection. He has combined laser pumping, optical magnetometry detection and cross polarization to hyperpolarize nuclei which enhances contrast in MRI, and introduced a novel xenon biosensor. The Pines group continues to pursue development of theory, methodology and instrumentation for hyperpolarization via parahydrogen and nitrogen-vacancy centers in nanodiamonds with application to quantum sensors as well technology for tabletop NMR devices and microfluidic chips.

Pines' awards and honors include the 1991 Wolf Prize in Chemistry, the UC Berkeley Distinguished Teaching Award, ACS Irving Langmuir Award, Faraday Medal of the Royal Society, and The Berkeley Citation. He is a Member of the US National Academy of Sciences and Foreign Member of the Royal Society (London). Over two hundred self-dubbed 'Pinenuts' have passed through his lab, many including his co-author here, hold leading positions worldwide in academia, national labs, industry and beyond.

Lyndon Emsley is currently a Professor of Physical Chemistry at the École Polytéchnique Fédérale de Lausanne (EPFL) in Switzerland. After undergraduate studies at Imperial College, he completed a PhD with Geoffrey Bodenhausen developing new methods for selective excitation in liquid-state NMR. He was introduced to solid state NMR in 1991 when he began a Miller Fellowship at UC Berkeley with Alex Pines. In 1994 he moved to the Ecole Normale supérieure de Lyon as a Professor of Chemistry, and was appointed project director for the European Laboratory for Very High Field NMR which delivered the world's highest field NMR spectrometer operating at 1 GHz.

At the EPLF Emsley's focus is the development of solid-state NMR methodology for the determination of atomic-scale molecular structures in a wide variety of systems including pharmaceuticals, crystals, molecules on surfaces, hybrid inorganic structures, and amorphous materials. His work in to improve NMR crystallography, where in contrast to x-ray methods a single crystal is not necessary, demonstrate the potential for strutural determination of organic molecules by a combination of solid state NMR and density functional theory. Emsley and co-workers also employed Dyamic Nuclear Polarization (DNP) and isotopic labling to introduce Surface Enhanced NMR Spectrocospy (SENS) which improves the signal from material surfaces or near-surface species by three orders of magnitude over previous techniques.

Emsley's achievements have been recognized by international awards and honours including the Grand Prix Charles-Léopold Meyer from the French Académie des Sciences, the 2012 AMPERE Prize, the 2015 Bourke Award of the Royal Society of Chemistry, and the 2023 Günther Laukien Prize.

Lectures on Pulsed NMR (2^{nd} Ed), Lyndon Emsley and Alexander Pines

ITALIAN PHYSICAL SOCIETY

PROCEEDINGS
OF THE
INTERNATIONAL SCHOOL OF PHYSICS
«ENRICO FERMI»

Course CXXIII

edited by B. Maraviglia
Director of the Course
VARENNA ON LAKE COMO
VILLA MONASTERO
13-21 October 1992

Nuclear Magnetic Double Resonance

1993

NORTH-HOLLAND
AMSTERDAM - OXFORD - NEW YORK - TOKYO

PUBLISHED BY
North-Holland
Elsevier Science Publishers B.V.
P.O. Box 211
1000 AE Amsterdam
The Netherlands

SOLE DISTRIBUTORS FOR THE USA AND CANADA:
Elsevier Science Publishing Company, Inc.
655 Avenue of the Americas
New York, N.Y. 10010
U.S.A.

Technical Editor
P. PAPALI

Library of Congress Cataloging-in-Publication Data

International School of Physics "Enrico Fermi" (1992 : Varenna, Italy)
Nuclear magnetic double resonance : Varenna on Lake Como, Villa Monastero, 13-21 October 1992 / edited by B. Maraviglia.
p. cm. -- (Proceedings of the International School of Physics "Enrico Fermi" ; course 123)
Title on added t.p.: Doppia risonanza magnetica nucleare.
At head of title: Italian Physical Society.
ISBN 0-444-81823-5
1. Electron nuclear double resonance--Congresses. I. Maraviglia, B. II. Società italiana di fisica. III. Title. IV. Title: Doppia risonanza magnetica nucleare. V. Series: International School of Physics "Enrico Fermi." Proceedings of the International School of Physics "Enrico Fermi" ; course 123.
QC762.6.E45I58 1992
538'.362--dc20 93-48564
CIP

Printed in Italy

Lectures on Pulsed NMR (2nd Edition).

L. EMSLEY and A. PINES

Materials Sciences Division, Lawrence Berkeley Laboratory, and
Department of Chemistry, University of California - Berkeley, CA 94720

Introduction.

These lectures are an expanded version of those given at the Fermi School in 1986 and published in 1988[1]. The combined lectures of the two authors at the present school encompass, first of all, the previous topics of multiple-quantum NMR, spin decoupling, interactions of spins with quantized fields, cross-polarization, coherent averaging and zero-field NMR. Secondly, in addition to expanding the discussion on some of the above topics, the present lectures treat several other topics (including some recent developments), among them new sample spinning techniques, group theory and molecular dynamics, unitary bounds on spin dynamics and geometric phases. Within the scope of this school it is impossible to provide a comprehensive treatment of all the topics above, and we apologize, therefore, in advance that we have omitted important concepts and contributions from many workers in the field. Our hope is that we can provide a glimpse into some of the fundamental physics of pulsed NMR, with examples, mainly from our own laboratory, of the applications of modern techniques to condensed-matter problems.

1. – Multiple-quantum NMR.

1·1. *Dipolar couplings and molecular structure.* – In high magnetic field, the dipolar coupling d_{jk} between two spins j and k on a molecule depends on the distance r_{jk} between the spins and on the angle θ_{jk} of the j-k vector relative to the field[2-5]:

$$d_{jk} \sim \frac{1}{r_{jk}^3}(3\cos^2\theta_{jk} - 1)\,. \tag{1.1}$$

Measurements of time-averaged dipolar couplings from the NMR spectrum, therefore, can provide information about molecular structure and dynamics[6-

8]. Figure 1.1 illustrates the sensitivity of NMR spectra to structure by showing an experimental spectrum of benzene oriented in a liquid crystal, as well as simulated spectra for different possible structures of symmetric six-carbon frameworks. This figure, provided by Z. LUZ of the Weizmann Institute of Science, demonstrates clearly how precise the determination of the authentic hexagonal structure is in this simple pedagogical case.

1·2. *Onset of spectral complexity.* – The case of benzene, with six proton spins, exemplifies a resolved tractable spectrum of dipolar couplings [9, 10]. The situation rapidly becomes more complex, however, as the number of spins is increased. This effect is illustrated in fig. 1.2, also courtesy of Z. LUZ. Beyond ten or so spins, depending on symmetry, the exponential increase in the number of NMR transitions renders the spectrum intractably complex. The

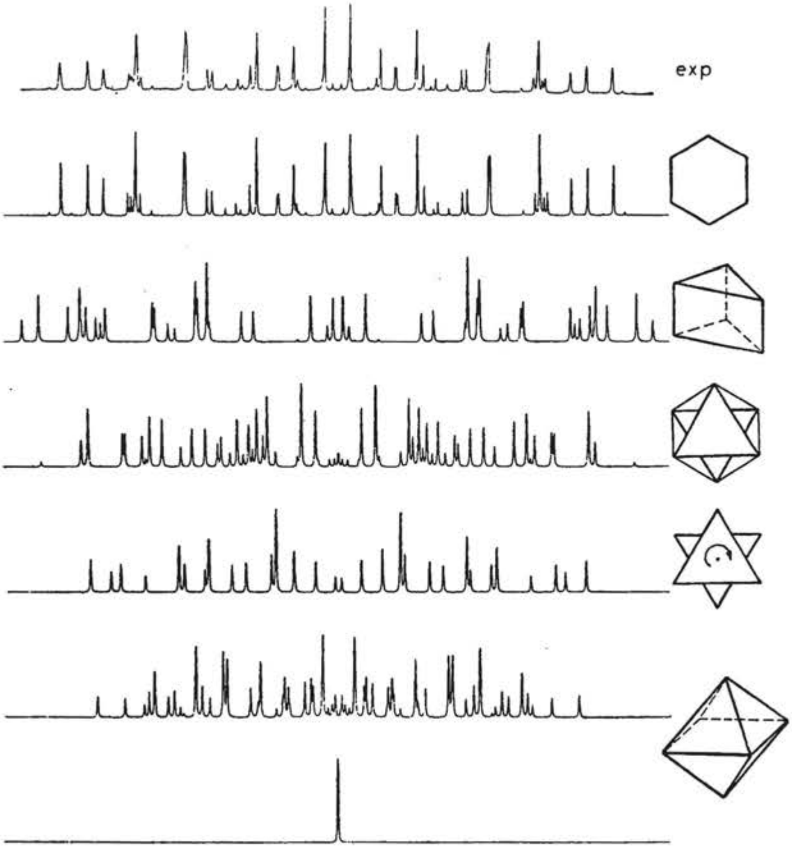

Fig. 1.1. – Experimental (exp) one-quantum proton NMR spectrum of benzene oriented in a liquid crystal, compared with simulated spectra of symmetric six-carbon structures. The isotropic spectrum, consisting of one line (bottom), is compatible with all these structures. (Courtesy of Z. LUZ.)

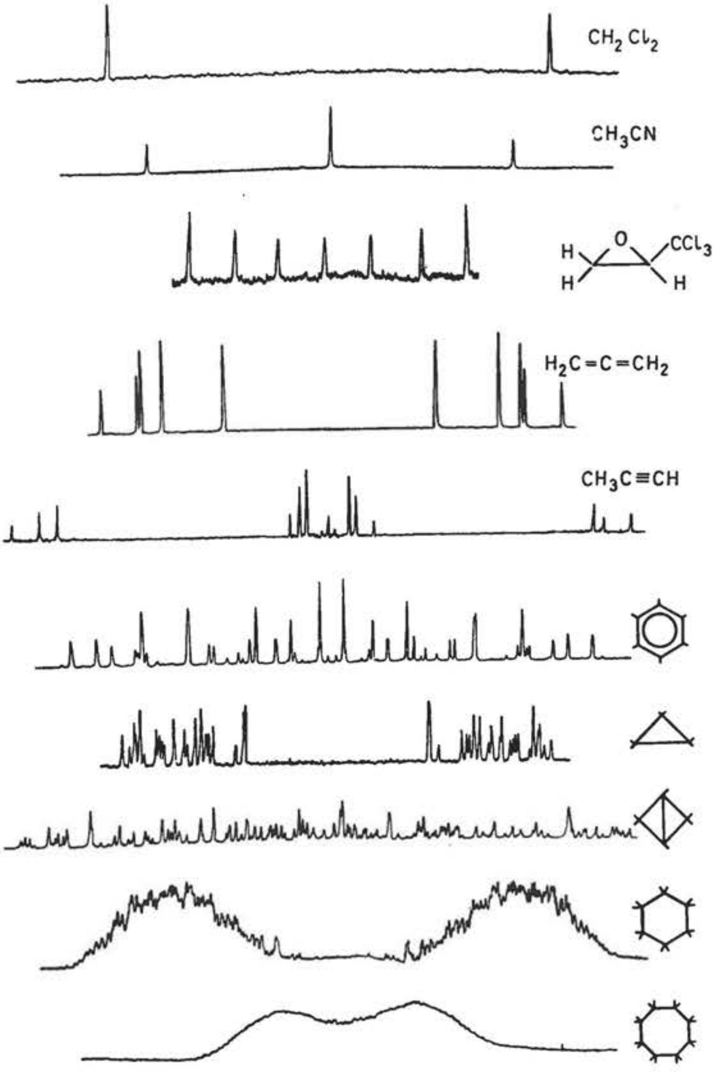

Fig. 1.2. – Proton NMR spectra of oriented molecules with various numbers of spins. The spectral complexity increases exponentially with the size of the spin system. (Courtesy of Z. LUZ.)

case of eight spins is illustrated in fig. 1.3 and 1.4, which show the spectrum of n-hexane-d_6 (methyl groups deuterated) in isotropic solution (fig. 1.3), where the dipolar couplings are averaged to zero (and where, at this resolution, the chemical shifts are essentially the same), compared to the spectrum of the same molecule oriented in a liquid crystal (fig. 1.4).

A rough estimate of the complexity can be made by looking at fig. 1.5, which shows the energy level diagram for a group of N coupled spins $I = 1/2$ in high

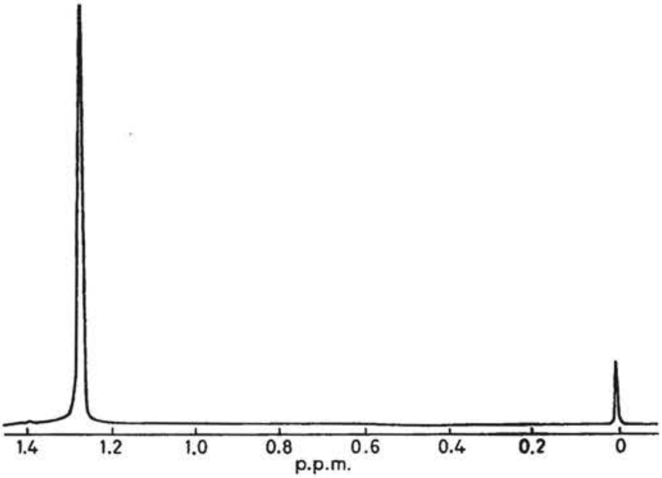

Fig. 1.3. – Proton NMR spectrum of n-hexane-d_6 in isotropic solution. All protons have roughly the same chemical shift, and give one line at this level of resolution. The line at the right is from a TMS standard. (Adapted from *Chem. Phys.*, **108**, 179 (1986), with permission.)

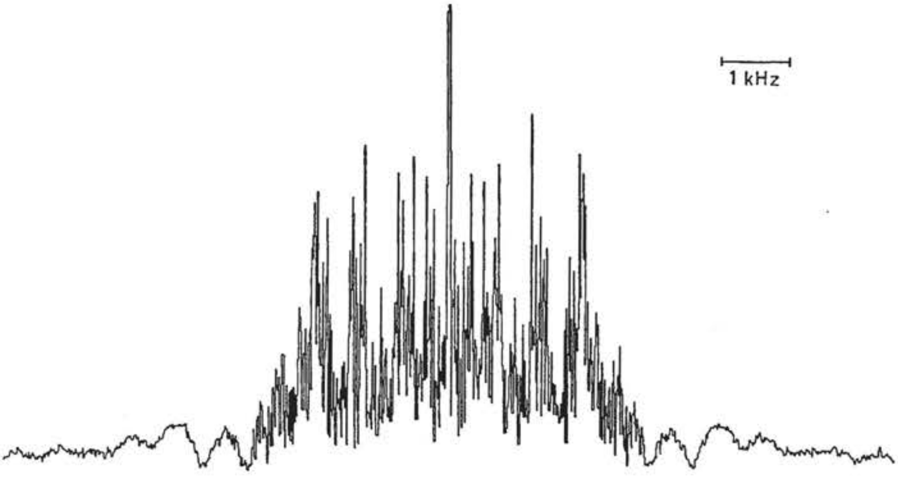

Fig. 1.4. – Proton NMR spin echo spectrum of oriented n-hexane-d_6 (deuterated methyls) with deuterium spin decoupling, to be compared with the isotropic spectrum in fig. 1.3. Even for this system of eight protons, there are about three thousand transitions, and the spectrum is intractable. (Adapted from *Chem. Phys.*, **108**, 179 (1986), with permission.)

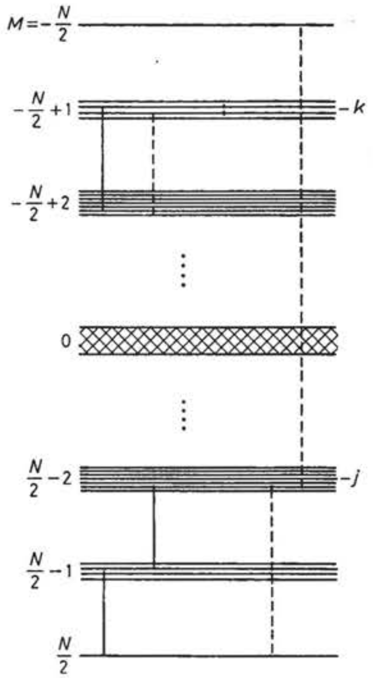

Fig. 1.5. – Energy level diagram of a system of N coupled spins $I = 1/2$ in high magnetic field. The groups of energy levels are characterized by the magnetic Zeeman quantum number M. The splittings in each group are due to chemical shifts and couplings between the spins. The solid vertical lines indicate allowed ($\Delta M = \pm 1$) one-quantum transitions and the dashed vertical lines depict some «forbidden» multiple-quantum ($\Delta M = \pm n$, $n = 0, 1, \ldots, N$) transitions. (Adapted from *J. Chem. Phys.*, **73**, 2084 (1980), with permission.)

field. The conventional one-quantum NMR transitions, shown as solid vertical lines, are subject to the selection rule

$$|\Delta M| = 1\,. \tag{1.2}$$

The number of energy levels with magnetic quantum number M is $\binom{N}{N/2+M}$ and, if one is restricted to transitions between neighboring M's, then

$$Z_1 = \sum_M \binom{N}{N/2+M}\binom{N}{N/2+M+1} = \binom{2N}{N+1} \tag{1.3}$$

is an upper bound to the number of one-quantum transitions. For $N = 4$ this number is 56, for $N = 8$ it is 11440, and for $N = 12$ it is 2496144 [11].

1·3. *Simplification by multiple-quantum transitions.* – Having encountered the problem of spectral complexity, we may also discern in fig. 1.5 a possible solution. The dashed vertical lines indicate *multiple-quantum* transitions [12-18] in which several spins flip together subject to the general rule

$$|\Delta M| = n\,. \tag{1.4}$$

As n, the number of quanta, increases, the number of transitions decreases and the spectra should, therefore, become simpler. Generalization of eq. (1.3) to n-quantum transitions yields

$$Z_n = \binom{2N}{N+n}, \tag{1.5}$$

and for zero-quantum transitions

$$Z_0 = \binom{2N}{N} - 2^N\,. \tag{1.6}$$

Examining these expressions, we can see that the dependence of the number of transitions on N for high n ($n = N, N-1, N-2$) is roughly

$$\begin{cases} Z_N \sim 1\,, \\ Z_{N-1} \sim N\,, \\ Z_{N-2} \sim N^2\,. \end{cases} \tag{1.7}$$

Thus the number of $(N-2)$-quantum transitions is quadratic in the number of spins, and, since the maximum number of couplings is

$$Z_d = \frac{N(N-1)}{2} \sim N^2\,, \tag{1.8}$$

the $(N-2)$- and $(N-1)$-quantum spectra should contain sufficient information to determine the d_{jk}.

1·4. *Analogy to chemical isotopic labeling.* – There are other ways to simplify spectra. One conceptually simple but synthetically demanding method is to isotopically label spins at selected positions in the molecule. For example, deuteration of all but two positions on a molecule dramatically reduces the number of lines in the proton spectrum and thus facilitates the direct determination of the d_{jk}'s. We may then ask about the relationship of this simplification to the simplification realized in multiple-quantum spectra. Note that the number of isotopically substituted species with single labels is at most N and that the number of isotopically doubly labeled species is at most $N(N-1)/2$, the same as the number of $(N-1)$- and $(N-2)$-quantum transitions, respectively. In effect, when we flip $N-1$ out of N spins, the remaining spin (or, equivalently, the one labeled spin) can be in any one of N positions. When we flip $N-2$, the remaining two can be in $N(N-1)/2$ configurations. Hence the $(N-p)$-quantum spectrum is a superposition of spectra from all possible arrangements of p isotopic labels.

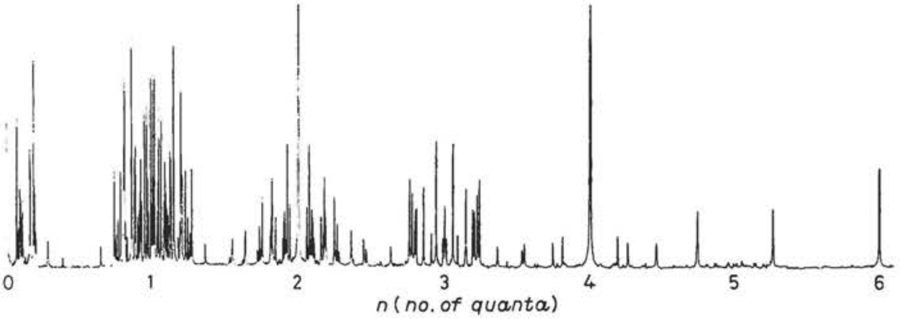

Fig. 1.6. – Multiple-quantum NMR spectra of oriented benzene, showing the progressive simplifications as the number of quanta increases from 1 to 6. The spectra were averaged over a range of preparation and mixing times. We can see one six-quantum transition, two five-quantum transitions and seven four-quantum transitions, as anticipated in the text. (Courtesy of G. DROBNY.)

As an example, consider oriented benzene, whose one-quantum spectrum was shown in fig. 1.1. The 6-quantum spectrum should contain one line, since there is only one way to absorb six quanta and thereby flip all six spins. The 5-quantum spectrum arises from, roughly speaking, flips of five spins in the field of a sixth. Since this last spin may be up or down, and since all positions on the molecule are equivalent, the 5-quantum spectrum should contain just one doublet. In general there will be a doublet for each inequivalent position or each different singly labeled species. Next we have the 4-quantum spectrum, which involves the flip of four spins in the field of the remaining two. These two can be ortho, meta, or para (the three doubly labeled isomers), so we expect three triplets (seven lines). Figure 1.6 clearly shows these predictions realized in the multiple-quantum NMR spectra of oriented benzene.

1·5. *Obtaining multiple-quantum spectra.* – Since multiple-quantum transitions are not directly observable with an NMR coil, they must be detected indirectly using coherence transfer [19, 20] by two-dimensional spectroscopic methods [5, 16]. The general scheme of such an experiment is

$$\text{preparation}(\tau)\text{-evolution}(t_1)\text{-mixing}(\tau')\text{-detection}(t_2)\,. \tag{1.9}$$

During the time period t_2, direct detection of allowed one-quantum frequencies provides information about the multiple-quantum frequencies in the earlier time period t_1. Two-dimensional Fourier transform then yields a spectrum which contains the directly detected one-quantum spectrum parallel to the frequency axis ω_2 and the multiple-quantum spectrum parallel to the frequency axis ω_1. An example is shown in fig. 1.7. The multiple-quantum spectrum of fig. 1.6 is the projection of such a two-dimensional spectrum, in absolute-value mode, onto the ω_1 axis. Figure 1.7*b*) clearly shows the seven four-quantum lines of benzene and their connections to the one-quantum transitions. Note that, to

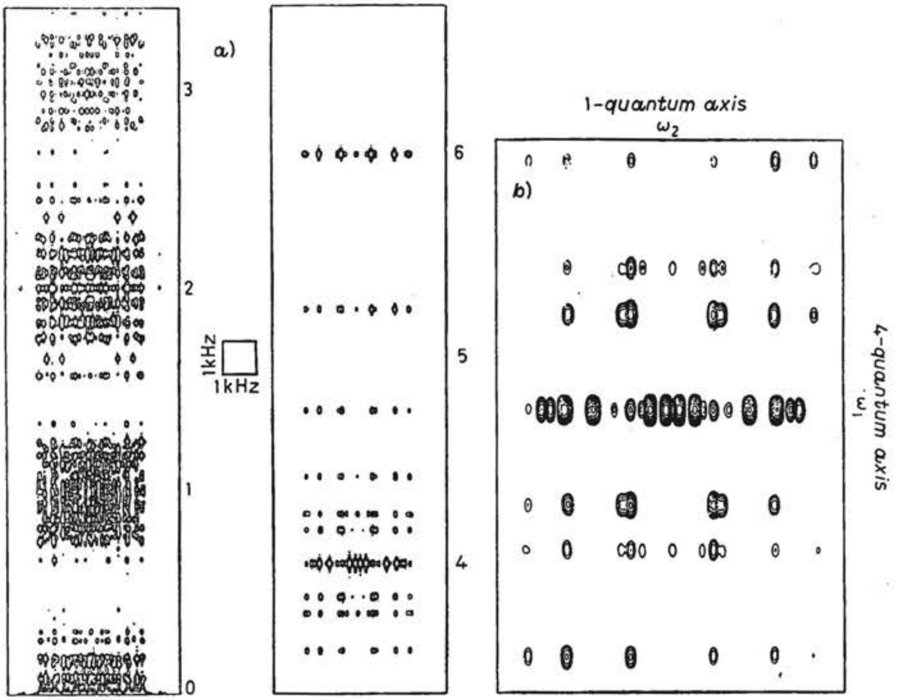

Fig. 1.7. – Contour plot of the two-dimensional multiple-quantum spectrum of oriented benzene and expansion of the four-quantum region. These plots show how coherence is transferred between the multiple-quantum evolution period (vertical axis) and the one-quantum detection period (horizontal axis). The preparation and mixing times were nine milliseconds. (Courtesy of G. DROBNY.)

obtain uniform multiple-quantum intensities, multiple-quantum spectra are typically averaged over a range of values of the preparation time $\tau(=\tau')$ [21].

1·6. *Theory of multiple-quantum* NMR: *preliminaries.* – Since we will be interested only in the multiple-quantum spectrum, that is, the projection onto the ω_1 axis, we need detect just the integrated ω_2 signal, which is given by the value of the magnetization at the first point in t_2. Furthermore, since the system usually begins in equilibrium at high temperature and in high field, where its density operator is proportional to I_z, we shall find it convenient to monitor I_z at $t_2 = 0$ following the mixing. This formulation, outlined in fig. 1.8, frames the problem in its most symmetric form with no loss of generality. $\boldsymbol{U}$ is the preparation propagator, $\boldsymbol{V}(t_1)$ the evolution propagator, and $\boldsymbol{U}'$ the mixing propagator. The value of $\langle I_z\rangle$ is detected at $t_2 = 0$ as a function of t_1. For simplicity of notation, we suppress the subscript in t_1 and write t, since only this one dimension will be relevant to the remaining discussion.

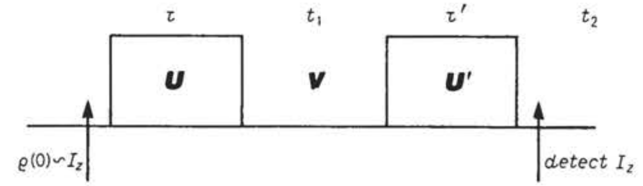

Fig. 1.8. – Timing diagram for basic multiple-quantum sequence. The multiple-quantum coherences are prepared from an initial high-temperature equilibrium state $\rho(0) \sim I_z$ by the propagator $\boldsymbol{U}(\tau)$; they evolve under the propagator $\boldsymbol{V}(t_1)$, and after mixing by $\boldsymbol{U}'(\tau')$ they are detected indirectly as z magnetization. This scheme is analogous to detecting x and y components in t_2 by adding or omitting pulses from $\boldsymbol{U}'$. By using different $\boldsymbol{U}'$, quadrature phases can be detected in t_1.

In general [22, 23], the initial quantum statistical state of a system is characterized by a density operator $\rho(0)$, which we depict as a *ket* $|\rho(0)\rangle$ (and its dual *bra* $\langle\rho(0)|$) in Liouville space. Under the influence of the propagator $\boldsymbol{U}(t)$ the system develops into a state $|\rho(t)\rangle$, *i.e.*

$$|\rho(t)\rangle = \boldsymbol{U}(t)|\rho(0)\rangle\,. \tag{1.10}$$

Diagrammatically, this transformation looks as follows:

$$|\rho(0)\rangle \bigcirc \xrightarrow{\quad \boldsymbol{U}(t) \quad} \bigcirc\ |\rho(t)\rangle\,. \tag{1.11}$$

$\boldsymbol{U}(t)$ is a superoperator [24], or superpropagator, which we shall continue to term propagator for short. (This usage should be distinguished from the propagator $U(t)$ that acts on quantum-mechanical kets in Hilbert space; context will normally render this distinction evident, but, for clarity, superoperators will be denoted in bold type.) $\boldsymbol{U}(t)$ is derived from the Hamiltonian superoperator or Liouvillian $\boldsymbol{H}$ by

$$\boldsymbol{U}(t) = \boldsymbol{T}\exp\left[(-i/\hbar)\int_0^t \boldsymbol{H}(t')\,\mathrm{d}t'\right], \tag{1.12}$$

where $\boldsymbol{T}$ is the Dyson time-ordering operator [25].

We recall that the density operator

$$\rho = \overline{|\psi\rangle\langle\psi|} \tag{1.13}$$

is the ensemble average of the projectors of the states ψ for the constituent members of the ensemble, and furthermore that the ensemble average expectation value of any observable Q (what we measure or observe) is given by

$$\overline{\langle Q\rangle} = \mathrm{Tr}\,\{\rho Q\} = \langle\rho|Q\rangle\,, \tag{1.14}$$

where

$$\langle A|B\rangle = \mathrm{Tr}\,\{A^{\dagger}B\} \tag{1.15}$$

is the scalar product in Liouville space.

1'7. *Multiple-quantum signal.* – We shall be concerned with the detection of the normalized signal $\langle I_z\rangle$ as a function of the evolution time t which yields the multiple-quantum free-induction decay $f(t)$ which will contain τ and τ' as parameters. In the superoperator notation, the state of the system $|\rho(t)\rangle$ at the end of the mixing in the scheme of fig. 1.8 is given by

$$|\rho(t)\rangle = \boldsymbol{U}'(\tau')\,\boldsymbol{V}(t)\,\boldsymbol{U}(\tau)\,|\rho(0)\rangle. \tag{1.16}$$

If we now assume a high-temperature, high-field equilibrium initial condition [26],

$$|\rho(0)\rangle = |I_z\rangle, \tag{1.17}$$

and detect $\langle I_z\rangle$, then eq. (1.16) yields the multiple-quantum free-induction decay

$$f(t) = \frac{\langle I_z|\boldsymbol{U}'(\tau')\,\boldsymbol{V}(t)\,\boldsymbol{U}(\tau)|I_z\rangle}{\langle I_z|I_z\rangle}\,. \tag{1.18}$$

Henceforth, we assume the signal to be normalized $(\langle I_z|I_z\rangle = 1)$, so that

$$f(t) = \langle I_z|\boldsymbol{U}'(\tau')\,\boldsymbol{V}(t)\,\boldsymbol{U}(\tau)|I_z\rangle. \tag{1.19}$$

So now you see the general rule with superoperators: begin on the right with a ket for the original state, propagate from right to left, and end on the left with a bra for the detected state. From eq. (1.19), given the Hamiltonians for the three periods (τ, t, τ'), $f(t)$ can be evaluated, and from the Fourier transform of this signal the multiple-quantum spectrum can be obtained. Let us examine some examples.

1'8. *Special case: one-quantum* FID *point by point.* – First we consider a «normal» one-quantum free-induction decay (FID) within the framework of fig. 1.8 and eq. (1.19). In such a normal FID, the transverse magnetization, say $\langle I_x\rangle$, is detected directly. However, we assume that the experiment is performed in a silly way, indirectly and point by point, by making $\boldsymbol{U}(\tau)$ a $(\pi/2)_y$ pulse, $\boldsymbol{U}'(\tau')$ a $(\pi/2)_{\bar{y}}$ pulse, and then detecting $\langle I_z\rangle$. This procedure is equivalent to detecting $\langle I_x\rangle$ *vs.* t. The scheme of fig. 1.8 then becomes

$$\boldsymbol{P}\text{-}t\text{-}\boldsymbol{P}^{\dagger}\text{-detect}\,\langle I_z\rangle, \tag{1.20}$$

where $\boldsymbol{P}$ and $\boldsymbol{P}^{\dagger}$ are the $\pi/2$ pulse superoperators. We now insert these expressions into eq. (1.19) and expand in a basis set of kets in Liouville space. Several basis sets may be considered, such as fictitious spin operators [2, 27-29], product operators [30-33], spherical tensors or multipole operators [34], and eigenoperators [16]. The non-Hermitian eigenoperators of $V(i)$, $|j\rangle\langle k|$, are in fact particularly well suited to these problems. For $j \neq k$ these correspond to coherences and for $j = k$ they correspond to populations. We represent the eigenoperators of $V(t)$ as kets written $|j-k\rangle$, so that

$$V(t)|j-k\rangle = \exp[-i\omega_{jk}t]|j-k\rangle, \tag{1.21}$$

where ω_{jk} is the frequency of the transition between eigenstates j and k of the (time-dependent) evolution Hamiltonian. Hence, we have

$$f(t) = \langle I_z|P^\dagger V(t) P|I_z\rangle = \sum_{j,k}\langle I_z|P^\dagger|j-k\rangle\langle j-k|V(t)|j-k\rangle\langle j-k|P|I_z\rangle. \tag{1.22}$$

We now use eq. (1.21) and evaluate the other matrix elements in eq. (1.22), for example,

$$\langle j-k|P|I_z\rangle = \mathrm{Tr}\left\{|k\rangle\langle j|PI_zP^\dagger\right\} = \langle j|PI_zP^\dagger|k\rangle = (PI_zP^\dagger)_{jk} = I_{xjk}\,, \tag{1.23}$$

where I_{xjk} is the (j, k)-th matrix element of the operator I_x. In this way we obtain the well-known result

$$f(t) = \sum_{jk}|I_{xjk}|^2\exp[-i\omega_{jk}t] \tag{1.24}$$

with its Fourier transform

$$y(\omega) = \sum_{jk}|I_{xjk}|^2\delta(\omega-\omega_{jk}), \tag{1.25}$$

giving the spectrum of $\langle I_x|I_x(t)\rangle$ the time autocorrelation function of I_x [35]. This spectrum yields the one-quantum frequencies, since $I_{xjk} \neq 0$ only for one-quantum transitions; consequently, we term I_x a one-quantum operator. An important point to note is that all lines in the spectrum have the same phase because of the appearance of squares of the absolute magnitudes of $(PI_zP^\dagger)_{jk} = I_{xjk}$.

1·9. *General case: multiple-quantum* FID. – We now expand eq. (1.19) in the $|j-k\rangle$ basis set for general U, U' to obtain

$$\begin{aligned} f(t) &= \langle I_z|U'(\tau')V(t)U(\tau)|I_z\rangle = \\ &= \sum_{jk}\langle I_z|U'(\tau')|j-k\rangle\langle j-k|V(t)|j-k\rangle\langle j-k|U(\tau)|I_z\rangle = \\ &= \sum_{jk}(I_z(-\tau'))_{kj}(I_z(\tau))_{jk}\exp[-i\omega_{jk}t], \end{aligned} \tag{1.26}$$

where

$$I_z(\tau) = U(\tau)I_zU^\dagger(\tau) \quad \text{and} \quad I_z(-\tau') = U'^\dagger(\tau')I_zU'(\tau') \tag{1.27}$$

are the effective preparation and mixing operators. These operators, however, are multiple-quantum operators, unlike I_x. As a consequence, the phases vary from line to line since $(I_z(-\tau')_{kj}(I_z(\tau))_{jk}$ are, in general, *complex* numbers.

As an example, consider the simplest and most widely used multiple-quantum sequence, the three-pulse sequence

$$\left(\frac{\pi}{2}\right)_y\text{-}\tau\text{-}\left(\frac{\pi}{2}\right)_{\bar{y}}\text{-}t\text{-}\left(\frac{\pi}{2}\right)_y\text{-detect}\,\langle I_x\rangle . \tag{1.28}$$

In the present framework, if the detection is to be matched to the preparation so that $\tau = \tau'$, then an additional $(\pi/2)_{\bar{y}}$ pulse must be inserted a time τ after the third $(\pi/2)_y$ to create

$$\boldsymbol{U}(\tau) = \boldsymbol{U}'(\tau). \tag{1.29}$$

Here both $\boldsymbol{U}$ and $\boldsymbol{U}'$ derive from the Hamiltonian H_{xx}, transformed by the y pulses from the normal bilinear (*e.g.*, dipolar) Hamiltonian H_{zz}.

Inserting eq. (1.29) into eq. (1.26) yields

$$f(t) = \sum_{jk} (I_z(\tau)_{jk})^2 \exp[-i\omega_{jk} t]. \tag{1.30}$$

Note that we have $(\dots)^2$ not $|\dots|^2$ for the matrix element in eq. (1.30). For closely spaced multiple-quantum lines, the arbitrary phases will cause a cancellation of intensity, a crucial problem in complex molecules and solids that is illustrated schematically in fig. 1.9*a*).

1'10. *Time-reversal (conjugate) detection.* – One solution to the phase problem mentioned above follows from the realization that the integrated intensity of the multiple-quantum frequency spectrum is given by the first point, $f(t = 0)$, of the free-induction decay, *i.e.*

$$f(0) = \langle I_z | \boldsymbol{U}'(\tau')\, \boldsymbol{U}(\tau) | I_z \rangle. \tag{1.31}$$

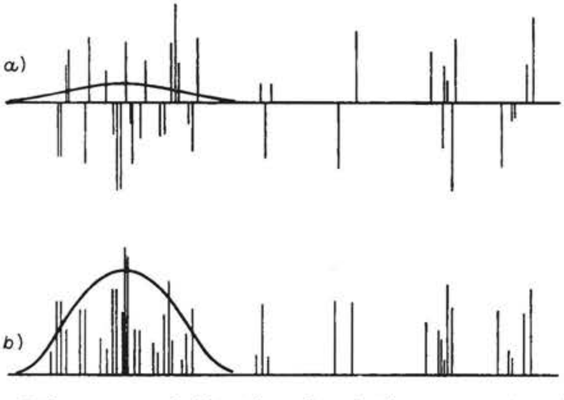

Fig. 1.9. – Effect of time-reversal detection. In *a*), the propagators $\boldsymbol{U}$ and $\boldsymbol{U}'$ are not conjugate (for example, $\boldsymbol{U} = \boldsymbol{U}'$ in the three-pulse multiple-quantum experiment $(x\text{-}\tau\text{-}\bar{x}\text{-}t_1\text{-}x\text{-}t_2)$), and the uncorrelated phases of nearby transitions can reduce the integrated intensity. In *b*), with time-reversal detection, $\boldsymbol{U} = \boldsymbol{U}'^{\dagger}$ and the lines are all in phase, thus restoring the full intensity.

Clearly, if we ensure that

$$\boldsymbol{U}'(\tau')\,\boldsymbol{U}(\tau) = 1\,, \tag{1.32}$$

then we can recover the full intensity as in a spin echo [36], and all the lines will be necessarily in phase [37]. This phasing happened naturally in the one-quantum case of eq. (1.24), and for the multiple-quantum case the same effect can be achieved if *the Hamiltonian for the preparation period* τ *is the negative of that for the mixing period* τ', namely

$$\boldsymbol{U}'(\tau') = \boldsymbol{U}^{\dagger}(\tau)\,. \tag{1.33}$$

Given eq. (1.32), we can evaluate eq. (1.26) as

$$f(t) = \sum_{jk} \left|(I_z(\tau)_{jk})^2\right| \exp[-i\omega_{jk}t] \tag{1.34}$$

to yield «in-phase» lines with the maximum integrated intensity, as depicted schematically in fig. 1.9*b*). (We shall see later that a more general condition, allowing all lines within a multiple-quantum order to be in phase, is also possible.)

1·11. *Effect of phase shifts.* – Consider the effect of a phase shift of φ, *i.e.* a rotation by φ around the z-axis. For example, if $\boldsymbol{U}(\tau)$ derives from a secular (high-field) Hamiltonian plus r.f. pulses, then such a phase shift is induced by changing the phases of all r.f. pulses by φ. We define

$$\boldsymbol{U}_{\varphi} = \boldsymbol{R}_z^{\dagger}(\varphi)\,\boldsymbol{U}\boldsymbol{R}_z(\varphi)\,, \tag{1.35}$$

where $\boldsymbol{R}_z(\varphi)$ is a z rotation superoperator

$$\boldsymbol{R}_z(\varphi) = \exp[-i\varphi \boldsymbol{I}_z]\,, \tag{1.36}$$

and we see that its effect on the eigenoperators is

$$R_z(\varphi)|j-k\rangle = \exp[-i\varphi n_{jk}]\,|j-k\rangle\,, \tag{1.37}$$

where

$$n_{jk} = M_k - M_j \tag{1.38}$$

is the number of quanta, or order, of the coherence or transition j-k. Thus *a phase shift of* φ *in any radiation that induces multiple-quantum transitions will be «seen» by an* n*-quantum transition as* $n\varphi$ [29].

Suppose we now perform a multiple-quantum experiment with time-reversal detection as in subsect. **1·10** but modify eq. (1.33) to obtain

$$\boldsymbol{U}(\tau) = \boldsymbol{U}_{\varphi}'^{\dagger}(\tau) = \boldsymbol{R}_z^{\dagger}(\varphi)\,\boldsymbol{U}'^{\dagger}(\tau)\,\boldsymbol{R}_z(\varphi)\,, \tag{1.39}$$

so that the phase of the preparation sequence is shifted by φ. Inserting this propagator into eq. (1.26) and using eq. (1.37), we find that eq. (1.33) now becomes

$$f_{\varphi}(0) = \sum_{jk} |I_z(\tau)_{jk}|^2 \exp[-i\omega_{jk}t]\exp[-i\varphi n_{jk}]\,. \tag{1.40}$$

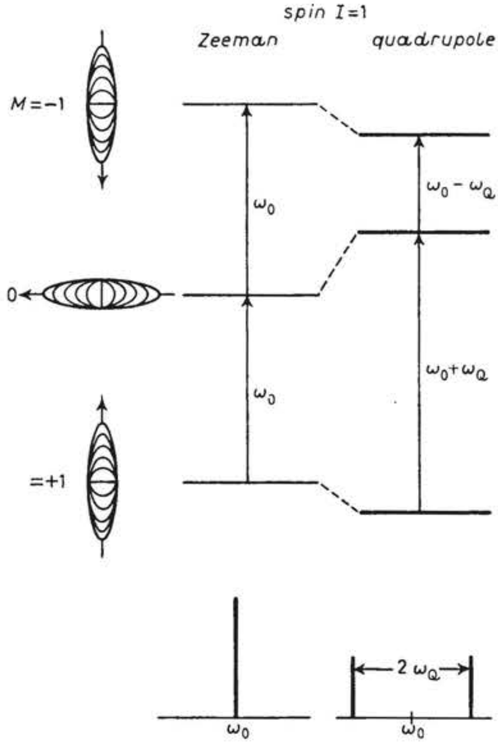

Fig. 1.10. – Deuterium energy levels in the laboratory frame showing the splitting of the one-quantum transitions by the electric-quadrupole interaction.

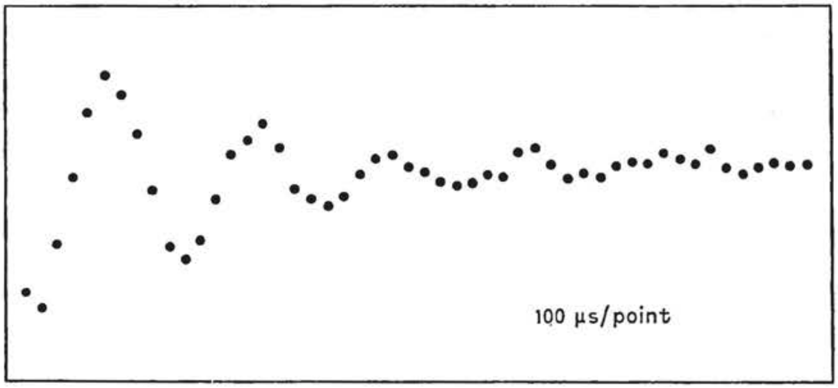

Fig. 1.11. – Double-quantum free-induction decay of deuterium in solid benzene-d_1 doped (10%) into benzene at – 40 °C, with proton decoupling. In contrast, the normal one-quantum deuterium free-induction signal decays in tens of microseconds. (Courtesy of S. VEGA.)

Thus each complete n-quantum spectrum is phase shifted by $n\varphi$. For $t=0$, we have

$$f_\varphi(0) = \sum_{jk} |I_z(\tau)_{jk}|^2 \exp[-i\varphi n_{jk}], \tag{1.41}$$

so the integrated intensities of the multiple-quantum spectra for each τ may be determined by Fourier transformation with respect to φ. This determination may be made more efficiently by varying φ proportionately to τ to yield the full τ-dependence of the n-quantum intensities in one experiment[38].

1'12. *Time-proportional phase incrementation* (TPPI). – The phase behavior above provides a convenient way to separate multiple-quantum coherences from each other (as shown, for example, in the benzene spectrum of fig. 1.6)[39, 40]. In eq. (1.40), if we set

$$\varphi = \Delta\omega t, \tag{1.42}$$

then we have

$$f(t) = \sum_{jk} |I_z(\tau)_{jk}|^2 \exp[-it(\omega_{jk} + \Delta\omega n_{jk})], \tag{1.43}$$

so each n-quantum line is shifted by $n\Delta\omega$, thereby allowing a clear separation of orders in one experiment.

1'13. *Double-quantum* NMR *in solids.* – One area where double-quantum NMR has played a particularly useful role is in spin $I = 1$ systems, *e.g.* deuterium. The appropriate energy level diagram is depicted in fig. 1.10. Owing to electric quadrupolar coupling the nonspherical deuterium nucleus experiences an orientation-dependent splitting of its resonance lines leading to broad powder signals (~ 100 kHz) in solids. This inhomogeneous broadening obscures the small chemical shifts, a problem that can be overcome by detecting the double-quantum spectrum[41, 42] (transitions between $M = \pm 1$), which is unencumbered by electric-quadrupole broadening. This approach allowed the first measurement of the chemical-shielding anisotropy (~ −6 p.p.m.) of hydrogen in benzene[27]. An example of these effects is provided in fig. 1.11 and 1.12, which show the double-quantum free-induction decay and spectrum of solid benzene-d_1. The double-quantum coherence was prepared by irradiating the center of the spectrum with a weak pulse, for which the r.f. amplitude ω_1 is much less than the quadrupole coupling ω_Q, resonant only with the double-quantum transition at ω_0. The effective $\pi/2$ pulse is then characterized by the condition

$$\frac{\omega_1^2}{\omega_Q}\tau = \frac{\pi}{2}, \tag{1.44}$$

where τ is the pulse length. We shall expand on this idea later when we get to double-quantum decoupling in subsect. 3'3 and double-quantum excitation in subsect. 4'8.

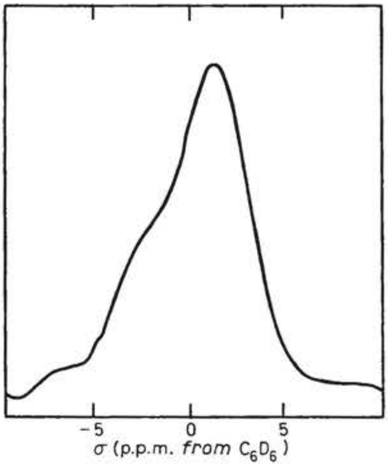

Fig. 1.12. – Fourier transform of the signal in fig. 1.11, showing the chemical-shift anisotropy of deuterium in benzene-d_1. The left edge of the spectrum corresponds to the benzene plane normal aligned with the magnetic field; the right peak corresponds to the perpendicular direction. (Courtesy of S. VEGA.)

The double-quantum transition of a single spin $I = 1$ is analogous to the full N-quantum spectrum of N coupled spins $I = 1/2$. We recall that the N-quantum spectrum arises from just one transition, unaffected by any spin-spin coupling.

1·14. *Double-quantum spin locking.* – Spin locking is a widely used technique for extending the lifetimes of coherences in the rotating frame, and is essential in various relaxation and cross-polarization experiments. It can be performed by applying a $(\pi/2)_y$ r.f. pulse to the z magnetization, and then shifting the r.f. phase by $\pi/2$ to x while irradiating continuously. The magnetization is thus aligned along the r.f. field and hence the term locking. The decay of the magnetization order now depends on spin-lattice processes in the rotating frame. An appealing question is whether one can lock *double-quantum* coherence in a similar fashion, even though the one-quantum spectrum may be extremely broad. In other words, can we create double-quantum coherence and then apply radiation to lock it? Suppose the double-quantum coherence is prepared with a weak pulse applied at the center of resonance. From the discussion in subsect. 1·11 we know a $\pi/4$ phase shift in the radiation is needed to deliver an effective phase shift of $\pi/2$ to the double-quantum transition. A pictorial representation of this behavior appears in fig. 1.13. The dipolar one-quantum coherences of fig. 1.13*a*) act like vectors (*i.e.* first-rank tensors), which are shown in the diagram as p_x and p_y orbitals that are created from a p_z orbital representing the equilibrium magnetization. In these circumstances, a $\pi/2$ phase shift takes p_x into p_y. The quadrupolar double-quantum coherences of fig. 1.13, however, act like second-rank tensors or $d_{x^2-y^2}$ and d_{xy} orbitals. A $\pi/4$ phase shift interchanges these orbitals, whereas a $\pi/2$ phase shift changes their

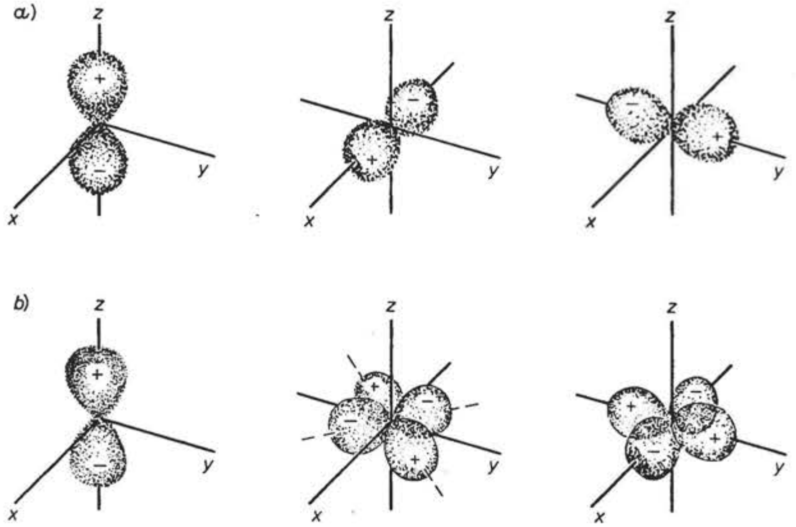

Fig. 1.13. – *a*) Symmetry of one-quantum dipole operators (analogous to *p* orbitals). They transform like vectors: a phase shift of $\pi/2$ interchanges p_x and p_y, and a phase shift of π changes their signs. *b*) Symmetry of double-quantum, quadrupole operators (analogous to p_z, d_{xy} and $d_{x^2-y^2}$ orbitals) involved in the fictitious spin $I = 1/2$ double-quantum transition ± 1 in fig. 1.10. The p_z orbital corresponds to z magnetization, and the two in-plane orbitals, corresponding to double-quantum coherence, transform like second-rank tensors: a phase shift of $\pi/4$ interchanges d_{xy} and $d_{x^2-y^2}$, and a phase shift of $\pi/2$ changes their signs. (Courtesy of J. MURDOCH.)

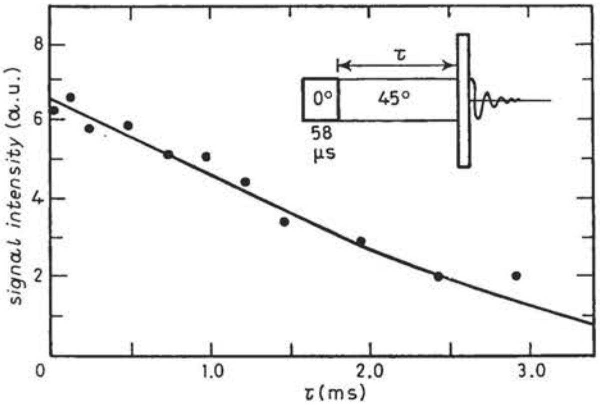

Fig. 1.14. – Double-quantum spin locking of deuterium in solid benzene-d_1. A «soft» $\pi/2$ pulse was applied at the ± 1 transition to create double-quantum coherence. The r.f. phase was then shifted by $\pi/4$ to spin lock the coherence for a prolonged period; the coherence was detected by a strong pulse which transformed it into observable one-quantum magnetization. (Courtesy of S. VEGA.)

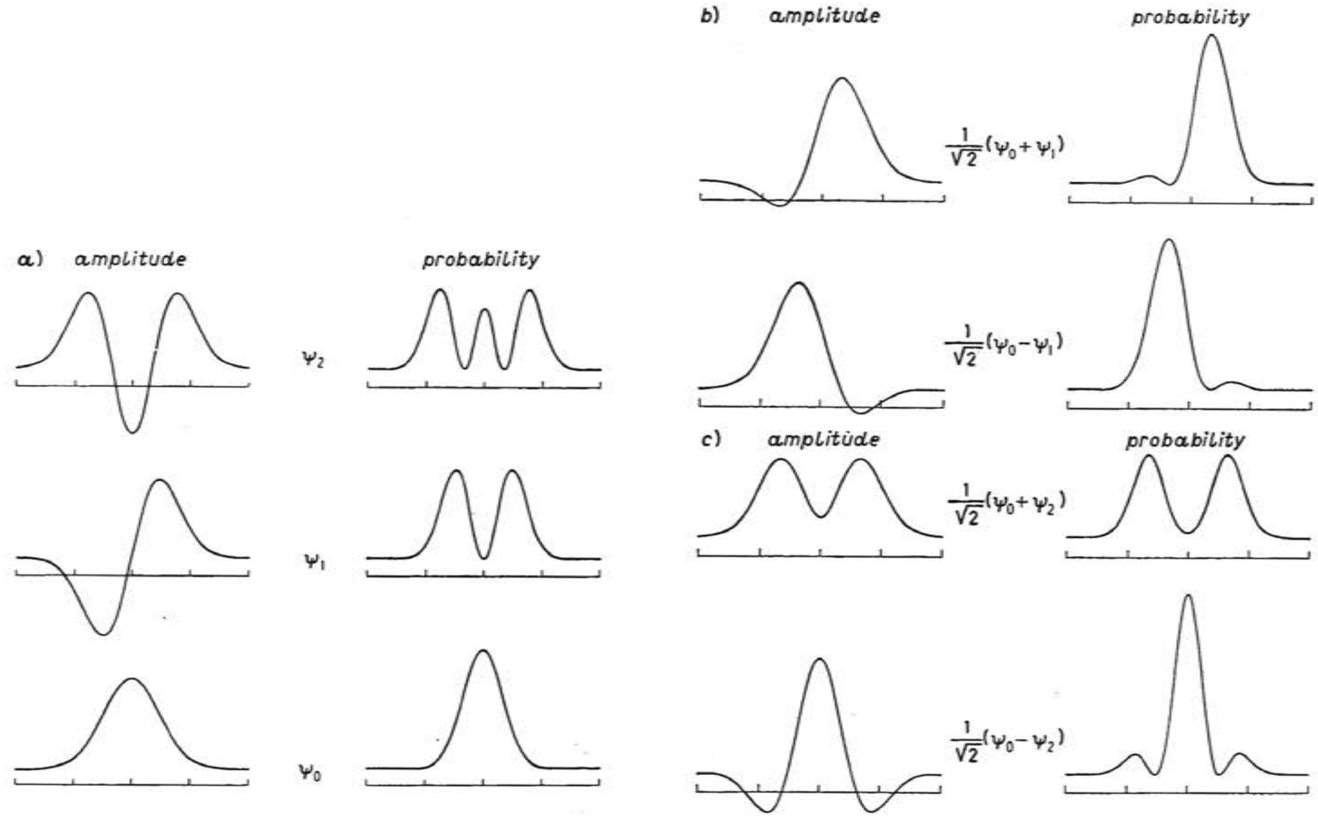

Fig. 1.15. – *a*) Three lowest wave functions $\psi_n(x)$ and probabilities $|\psi_n(x)|^2$ for a one-dimensional harmonic oscillator. *b*) Coherent superposition of ψ_0 and ψ_1 oscillating between $\psi_0+\psi_1$ and $\psi_0-\psi_1$. The probability density oscillates between left and right in analogy to the dipolar fictitious spin $I=1/2$ discussed in the text. *c*) Coherent superposition of ψ_0 and ψ_2 displaying quadrupolelike oscillations. (Courtesy of E. L. HAHN.)

sign [43]. (Here recall our earlier discussion (subsect. 1·10) of time reversal.)

The extension of a double-quantum free-induction decay time from a few hundred microseconds to a few milliseconds by a spin-locking experiment of this sort is shown in fig. 1.14. The technique has been used in double-quantum cross-polarization of broad deuterium and ^{14}N resonances in solids [27, 28]. A related technique involves the cross-polarization of the ^{14}N overtone [44].

Of course, these types of coherences do not occur exclusively in spin systems, but rather they are a general manifestation of the superposition of stationary states, which results in real or fictitious multipolar oscillations. For example, as shown in fig. 1.15, a coherent superposition between the ψ_0 and the ψ_1 states of a one-dimensional harmonic oscillator exhibits «dipolarlike» oscillations, and a coherent superposition between the ψ_0 and ψ_2 states exhibits «quadrupolarlike» oscillations as the superpositions evolve between the ± combinations [45].

1·15. *Molecular structure by multiple-quantum* NMR. – In our previous discussions of multiple-quantum NMR, oriented benzene served as a convenient pedagogical prototype. Another example, perhaps closer to «real life», is given in fig. 1.16, which shows the normal one-quantum spectrum of a cyanobiphenyl liquid-crystal molecule containing 8 protons [18]. The result is to be contrasted with the six-quantum spectrum in fig. 1.17, where an analysis of the spectrum in terms of dipole couplings may be made to study the structure and dynamics of this flexible molecule. Using the structure

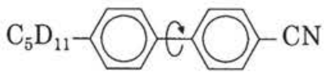

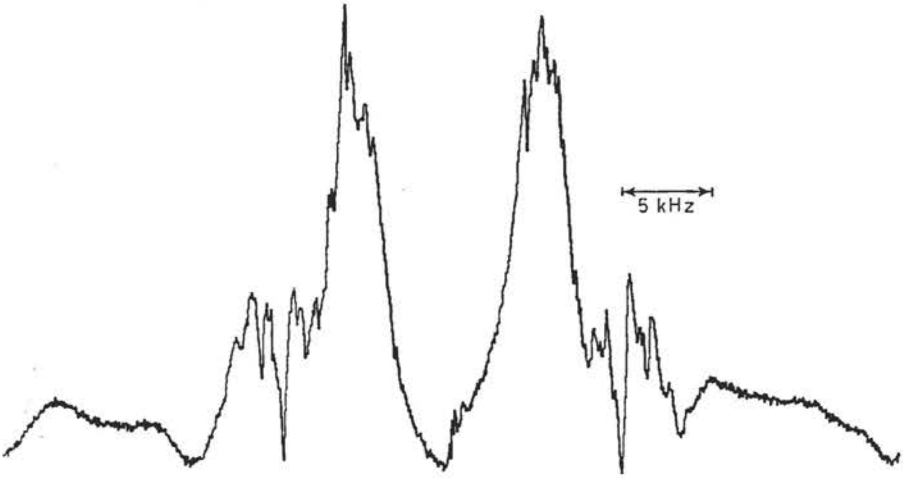

Fig. 1.16. – One-quantum NMR spectrum of the nematic liquid crystal *p*-pentyl-*p*-cyanobiphenyl-d_{11} (5CB) at 26.0 °C. The total frequency bandwidth is 50 kHz. (Adapted from *Mol. Phys.*, 53, 333 (1984), with permission.)

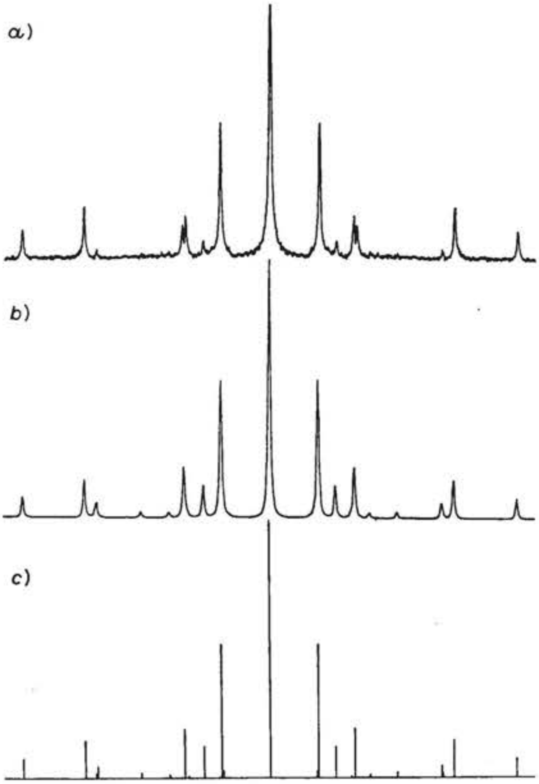

Fig. 1.17. – Six-quantum spectrum of 5CB, to be compared with fig. 1.16. This spectrum could be analyzed to yield the order tensor as well as the structure and dynamics of the biphenyl group. The lower plots are simulations (stick spectrum and slightly broadened spectrum) based on this structure assuming D_z symmetry for the spin Hamiltonian. The total frequency bandwidth is 44.2 kHz. Several spectra with different mixing times were used to obtain more uniform intensities for the lines. (Adapted from *Mol. Phys.*, **53**, 333 (1984), with permission.)

with jumps between the four equivalent conformations, the five-quantum spectrum can also be simulated, and this spectrum is compared with experiment in fig. 1.18.

A further application of multiple-quantum methods combines multiple-quantum filtering with two-dimensional correlation spectroscopy to investigate randomly deuterated molecules in liquid crystals. This method allows a separation of the different proton-containing isotopomers in situations where the normal proton spectra might be too complex (recall, for example, hexane-d_6 in fig. 1.4). An example of such simplified spectra, obtained for 80% randomly deuterated hexane, is shown in fig. 1.19[46]. Spectrum 1.19*a*) was obtained with the

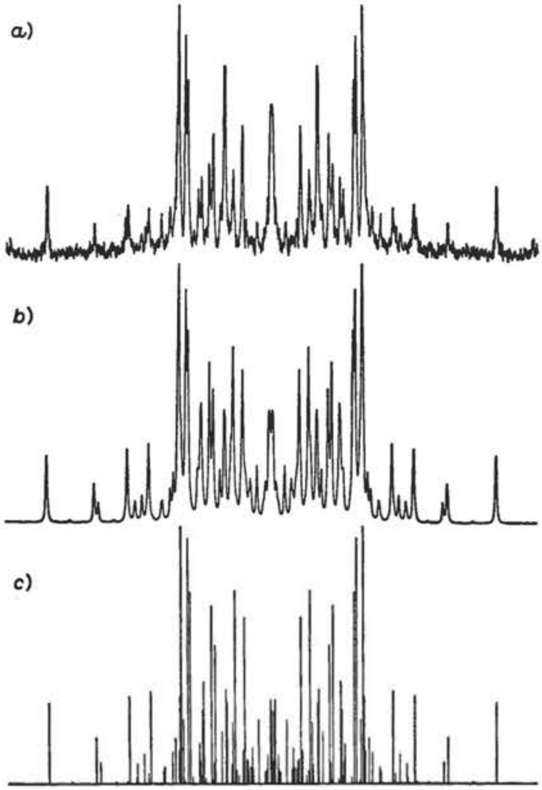

Fig. 1.18. – Five-quantum spectrum of 5CB showing the onset of complexity as we progress (or regress) from six quanta (fig. 1.17) towards one quantum (fig. 1.16). The simulation in the lower plots was produced from the structural and dynamic parameters derived from the six-quantum spectrum. The total frequency bandwidth is 62.5 kHz. Here, too, spectra from a range of preparation and mixing times were averaged together. (Adapted from *Mol. Phys.*, **53**, 333 (1984), with permission.)

pulse sequence

$$\left(\frac{\pi}{2}\right)_{\varphi}\text{-}t_1\text{-}\left(\frac{\pi}{2}\right)_{\varphi}\text{-}\frac{\tau_1}{2}\text{-}\pi_x\text{-}\frac{\tau_1}{2}\text{-}\left(\frac{\pi}{2}\right)_{x}\text{-}\frac{\tau_2}{2}\text{-}\pi_x\text{-}\frac{\tau_2}{2}\text{-sample}\,, \tag{1.45}$$

where φ is incremented in 90° steps while alternating the detector phase between 0° and 180° and increasing τ_1 after every fourth shot to reduce contributions from three-spin systems. Spectrum 1.19*b*) was obtained with the sequence

$$\left(\frac{\pi}{2}\right)_{\varphi}\text{-}\frac{\tau_1}{2}\text{-}\pi_{\varphi}\text{-}\frac{\tau_1}{2}\text{-}\left(\frac{\pi}{2}\right)_{\varphi}\text{-}t_1\text{-}\left(\frac{\pi}{2}\right)_{x}\text{-}\frac{\tau_2}{2}\text{-}\pi_x\text{-}\frac{\tau_2}{2}\text{-sample}\,, \tag{1.46}$$

where φ and the detector are again cycled. In this way, all 16 dipolar couplings of oriented hexane have been determined and assigned to positions on the molecules. Note that hexane is a formidable spin system, with 14 strongly cou-

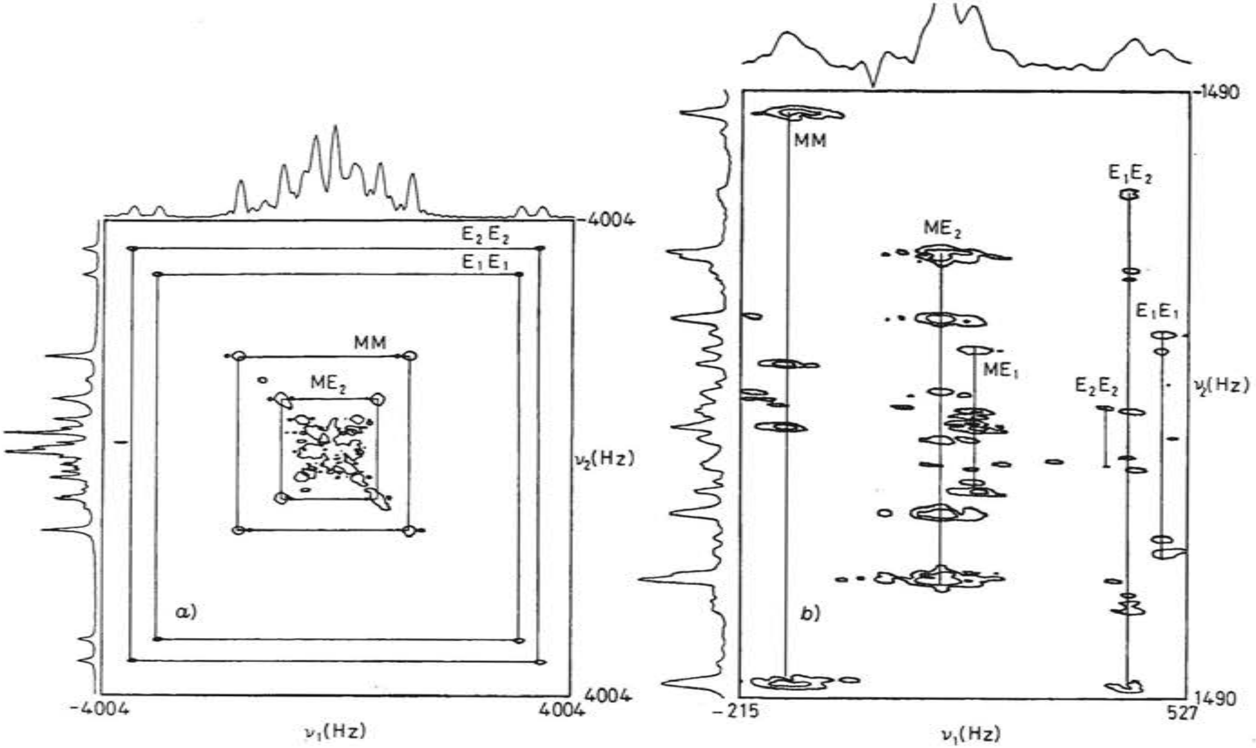

Fig. 1.19. – *a*) Double-quantum filtered two-dimensional correlation spectrum of 81% randomly deuterated *n*-hexane, 23 mole % in EK 11650, taken with the pulse sequence described in the text with deuterium decoupling. 128 × 1024 point data sets were collected at 360 MHz, with a spectral width of 16 667 Hz in both dimensions. The square patterns, which reveal dipole couplings in individual isotopomers, are shown for four of the sixteen proton pairs. *b*) Part of a double-quantum *vs.* single-quantum spectrum obtained using the pulse sequence described in the text. ν_1 is the double-quantum axis and ν_2 is the single-quantum axis. Vertical lines parallel to the ν_2 axis indicate the six possible double-quantum frequencies of molecules with two protons. M, E_1 and E_2 correspond to the methyl and the two inequivalent ethylene positions in hexane. All the dipole couplings in oriented hexane have been determined in this way. (Adapted from *J. Am. Chem. Soc.*, **108**, 6813 (1986), with permission.)

pled protons, and that its conventional spectrum is considerably more complex than that shown in fig. 1.4. This technique can help determine conformational dynamics of flexible molecules of this kind [47, 48], and may be extended to molecules of biological interest.

1·16. *Selective n-quantum excitation.* – High n-quantum transitions, though desirable, are generally of annoyingly low intensity. This problem can be partly overcome, however, by selective n-quantum excitation, in which a phase-shifted string of sequences with propagators $\boldsymbol{U}_\varphi$ is concatenated [16]. The total propagator $\boldsymbol{U}_\mathrm{T}$ is given by

$$\boldsymbol{U}_\mathrm{T} = \boldsymbol{U}_{(n-1)\varphi} \dots \boldsymbol{U}_\varphi \boldsymbol{U}_0 \,, \tag{1.47}$$

with each $\boldsymbol{U}_\varphi$ obtained from a basic $\boldsymbol{U}_0$ by the transformation of eq. (1.35). If $\varphi = 2\pi/n$, then only n-quantum operators survive in the overall propagator, thereby making the propagator n-quantum selective. However, in order for this selectivity to be achieved, $\boldsymbol{U}$ must contain n-quantum operators. One approach is to construct a «sandwich»

$$\boldsymbol{U}_0 = \boldsymbol{Q}^\dagger \boldsymbol{U} \boldsymbol{Q} \,, \tag{1.48}$$

where $\boldsymbol{U}$ describes a brief excitation and $\boldsymbol{Q}$ and $\boldsymbol{Q}^\dagger$ describe a pair of lengthy sequences, related by time reversal, which induce multiple-quantum operators in $\boldsymbol{U}$. An example of selective excitation of the 4-quantum spectrum of oriented benzene is shown in fig. 1.20.

Selective excitation can be viewed in the frequency domain as shown in fig. 1.21 and 1.22. Two-quantum excitation involves phase shifts of $2\pi/2 = \pi$, *i.e.* $0, \pi, 0, \pi, 0, \pi, \dots$. This operator is symmetric in time and yields a symmetric

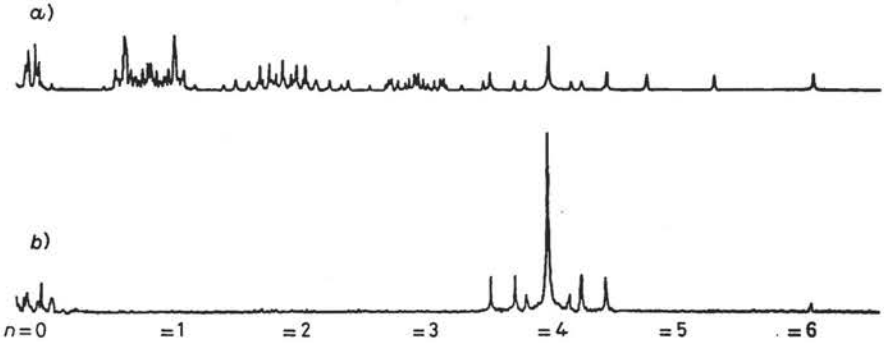

Fig. 1.20. – Multiple-quantum NMR spectra (ensemble averaged over a range of τ values) of oriented benzene *a*) with normal nonselective broad-band excitation and *b*) with four-quantum selective excitation. Selective n-quantum excitation enhances the n-quantum intensity, which, under nonselective excitation, may be low owing to the statistically low probability of absorbing many quanta. (Adapted from *J. Chem. Phys.*, **74**, 2808 (1981), with permission.)

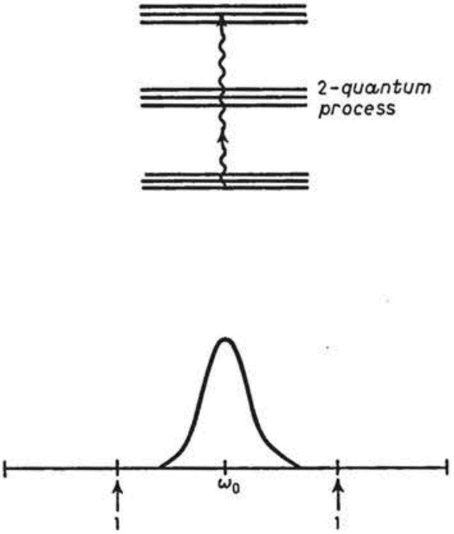

Fig. 1.21. – Symmetry of two-quantum selectivity by π phase shifting. The first resonant process involves one quantum each from the upper and the lower sidebands. (Adapted from *Adv. Magn. Reson.*, **11**, 111 (1983), with permission.)

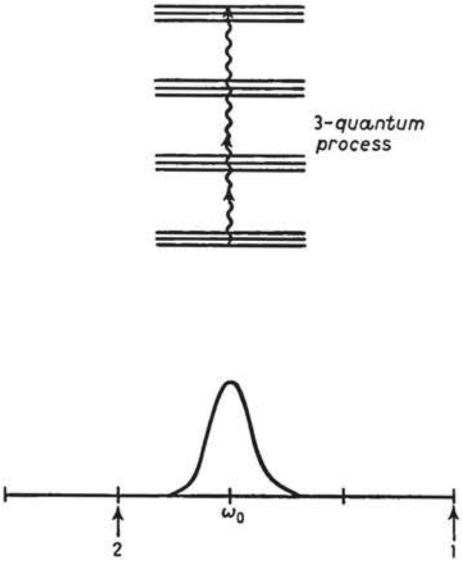

Fig. 1.22. – Symmetry of three-quantum selectivity by $2\pi/3$ phase shifts. The sidebands are now asymmetrically disposed about the resonance, and the first resonant process involves two quanta from the lower sideband and one from the upper sideband. (Adapted from *Adv. Magn. Reson.*, **11**, 111 (1983), with permission.)

nearest sideband structure about the resonance at ω_0 in fig. 1.21. The first resonant process is a 2-quantum transition involving one photon from each sideband. The phase shifts of $2\pi/3$ for 3-quantum excitation yield the sequence $0, 2\pi/3, 4\pi/3, 0, 2\pi/3, 4\pi/3, \ldots$ with the asymmetrical nearest sideband disposition shown in fig. 1.22. The first resonant process must now involve two photons from one sideband and one from the other. Bear in mind that this is a linear Fourier argument for the obviously nonlinear process of multiple-quantum excitation, so it is wrong in general. Nevertheless, it prescribes the correct symmetry and is useful if carefully applied.

1·17. *Multiple-quantum* NMR *in solids.* – Time-reversal detection as described in subsect. **1·10** is necessary in solids because the transition frequencies are distributed almost continuously. Consequently, there is an essentially complete cancellation of intensity if the phases of the line are random, as in fig. 1.9*a*). An alternative view of the same problem is depicted in fig. 1.23. Suppose we use the normal three-pulse sequence of eq. (1.28) to excite and observe multiple-quantum transitions in a solid. The integrated intensity of the multiple-quantum spectrum is given by the initial amplitude of the magnetization sampled in t_2 when $t_1 = 0$. But in a solid, after long τ the magnetization will have decayed to zero and hence little or no multiple-quantum intensity will be observed.

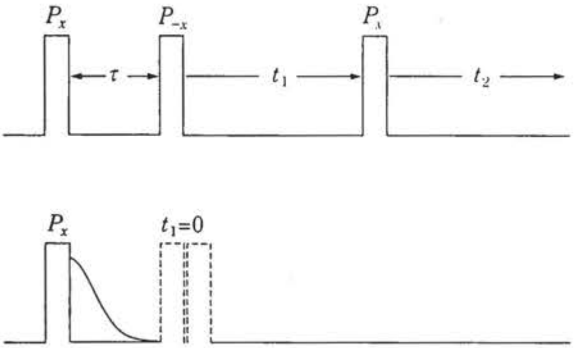

Fig. 1.23. – Pulse sequence for the three-pulse multiple-quantum scheme. If $t_1 = 0$ in a solid and τ is longer than the solid FID time, the signal is zero; hence the integrated multiple-quantum intensity will be zero as well. This illustration presents another view of the problem outlined in fig. 1.9.

Using the appropriate time-reversal detection, however, we can indeed obtain solid-state spectra with high n, in excess of 100 quanta[17]. An example of a suitable time-reversal excitation experiment is shown in fig. 1.24. The two pulses of this simple excitation sequence are replaced by a train of pulses whose average Hamiltonian (see sect. **2**) is given by

$$H_{\mathrm{DQ}} = (H_{xx} - H_{yy})/3\,, \tag{1.49}$$

where DQ denotes a pure double-quantum operator. The nonsecular Hamiltonian H_{xx} was mentioned in subsect. 1·9.

If the phases of the x and $\bar{x}$ r.f. pulses in the lower sequence of fig. 1.24 are all shifted by $\pi/2$ to y and $\bar{y}$ pulses, then we simply exchange the x and y indices in eq. (1.49) and obtain

$$R_z^\dagger\left(\frac{\pi}{2}\right)H_{\mathrm{DQ}}R_z\left(\frac{\pi}{2}\right) = -(H_{xx}-H_{yy})/3\,. \tag{1.50}$$

Hence, from eq. (1.12), the unitary propagator $\boldsymbol{U}$ is shifted to its adjoint

$$\boldsymbol{U} \rightarrow \boldsymbol{U}^\dagger\,, \tag{1.51}$$

as required for detection by eqs. (1.33) or (1.39) for use with TPPI.

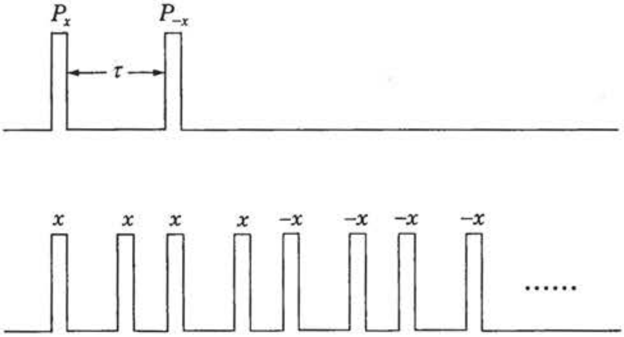

Fig. 1.24. – By replacing the pair of pulses with the lower pulse train and employing phase shifting, time-reversal detection can be used to recover the full multiple-quantum intensity in a solid.

Figure 1.25 shows multiple-quantum spectra obtained in solid hexamethylbenzene for different preparation and mixing times τ with the lower sequence of fig. 1.24 [18]. Solid hexamethylbenzene is an essentially infinite network of coupled spins, so we expect the multiple-quantum absorption to increase continuously with τ. If at any given τ we consider that a finite cluster of N spins has become involved, then, from eq. (1.5), the integrated intensity of the n-quantum transitions should go approximately as

$$Z_n = \binom{2N}{N+n} \sim \frac{4^N}{\sqrt{N\pi}}\exp[-n^2/N] \tag{1.52}$$

according to Stirling's approximation for large N and $n \ll N$. So we expect a roughly Gaussian distribution of intensities, a prediction borne out well in fig. 1.26, where even-ordered multiple-quantum spectra from a finite cluster of 21

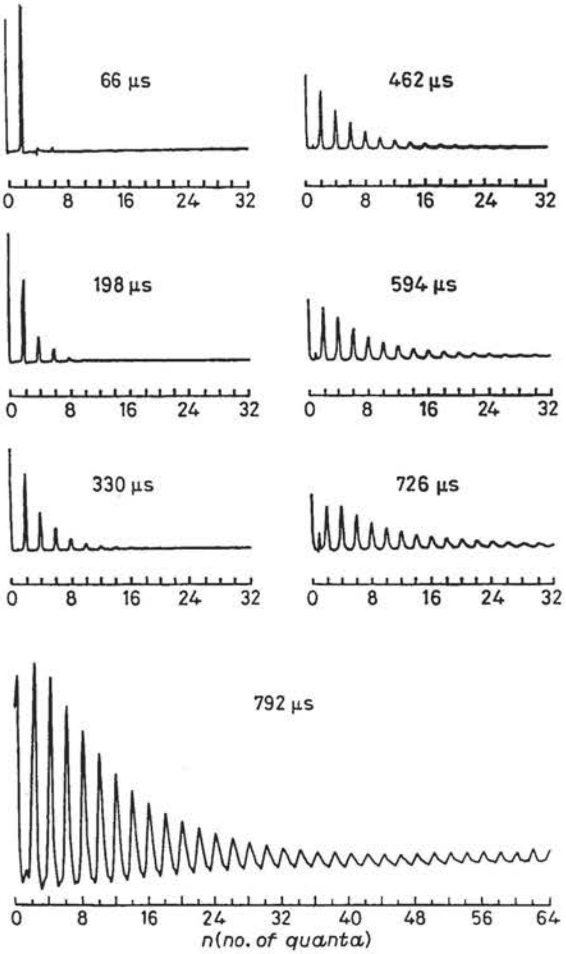

Fig. 1.25. - Multiple-quantum spectra of solid hexamethylbenzene obtained using the lower pulse sequence in fig. 1.24, with overall preparation and mixing times τ ranging from 66 to 792 μs. (The lowest trace, 792 μs, is expanded vertically.) As τ increases, more and more spins are correlated and more and more quanta are involved. In excess of one hundred quanta have been observed in this way. (Adapted from *J. Chem. Phys.*, **83**, 2015 (1985), with permission.)

spins are shown. The time dependence of the Gaussian width, also shown in fig. 1.26, can provide information on the distribution of atoms in materials, as depicted schematically in fig. 1.27. This method should be particularly useful for the study of clusters and, indeed, preliminary results have been realized in a number of cases, including inorganic solids, molecules in zeolite cavities [49], hydrogen in amorphous semiconductors [50] and atoms and molecules on sur-

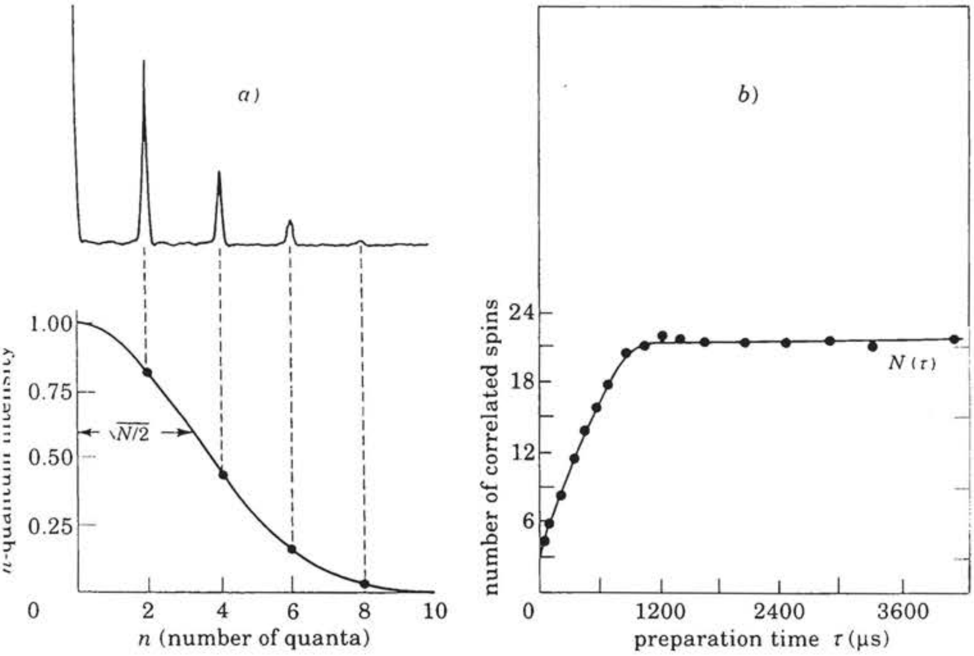

Fig. 1.26. – *a*) Multiple-quantum spectra of liquid crystal 5CB (containing 21 protons) showing a Gaussian distribution of intensities. *b*) Number of correlated spins $N(\tau)(\equiv$ maximum number of quanta) as a function of the preparation and mixing times τ in 5CB. $N(\tau)$ is extracted from an analysis of the Gaussian intensity distribution of *a*) as a function of τ. The plateau at 21 indicates that these molecules contain isolated clusters of 21 proton spins. (Adapted from *J. Am. Chem. Soc.*, **108**, 7447 (1986), with permission.)

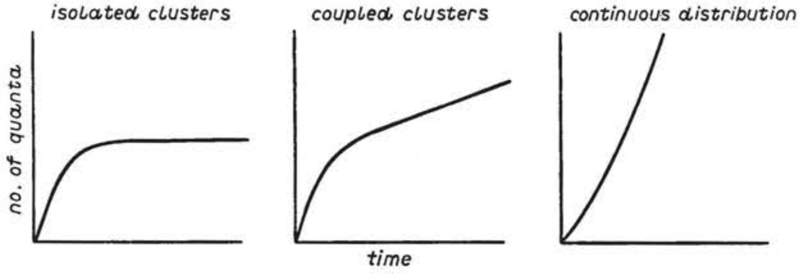

Fig. 1.27. – Schematic of $N(\tau)$, the number of correlated spins or maximum number of quanta, as a function of preparation time τ for various distributions of spins. This type of behavior has been observed in a variety of systems, including molecular crystals, molecules in zeolites, liquid crystals, absorbed species on surfaces and hydrogenated amorphous semiconductors.

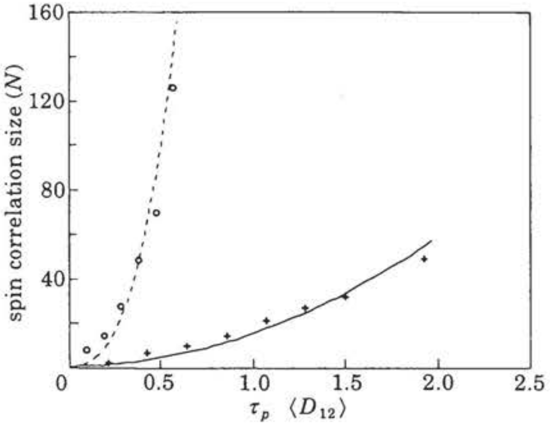

Fig. 1.28. – Fits of multiple-quantum dynamics models to data for CaH_2, representing a 3D system, and diamond powder, representing a surface or 2D system of hydrogen: ○ CaH_2, + diamond powder. The solid line refers to a 2D model while the dotted line represents a 3D model. (Adapted from *J. Phys. Chem.*, **96**, 8125 (1992), with permission.)

faces. For example, fig. 1.28 shows experimental results which allow a determination of the dimensionality of the system under consideration. In this case the growth of multiple-quantum coherence in the protons in a three-dimensional system (CaH_2) can easily be discriminated from the growth in the two-dimensional diamond powder system [51]. For extended coupled-spin systems, the more rigorous approach of Lacelle is to be preferred [51bis].

1'18. *Selection rules in multiple-quantum dynamics.* – If the pure double-quantum Hamiltonian eq. (1.49) is used for preparation and detection, then for $\rho(0) = I_z$ only even-quantum transitions are excited. If we characterize the dynamical evolution of the system by the number of spins N and the number of quanta, or coherence order, n, then the dynamical selection rules

$$\Delta N = \pm 1 \quad \text{and} \quad \Delta n = \pm 2 \tag{1.53}$$

are imposed. With the initial condition for $\rho(0) = I_z$

$$N = 1\,, \qquad n = 0\,, \tag{1.54}$$

the states ($N = 4$, $n = 4$), ($N = 8$, $n = 8$), ... are not accessible, *i.e.* we have the surprising consequence that it should not be possible to observe 4-quantum coherence in a 4-spin system, etc. [52]. Multiple-quantum dynamics studies have recently been extended by means of Monte Carlo techniques [53, 54].

1'19. *Total coherence transfer.* – Techniques related to multiple-quantum NMR are frequently useful for heteronuclear spectroscopy in isotropic liquids.

For example, to obtain narrow NMR spectra in the presence of inhomogeneous magnetic fields or susceptibility broadening. One technique, termed SHARP, uses echoes during the evolution of ^{13}C or ^{15}N coherence in the presence of coupled protons [55, 56]. This procedure should be useful in spatially selective NMR of heteronuclear systems with two r.f. coils, in particular where the relevant spatial region is in an inhomogeneous field or broadened by magnetic-susceptibility effects. An example, shown in fig. 1.29, demonstrates a simple version of spatial selectivity and high resolution with a surface coil on tubes con-

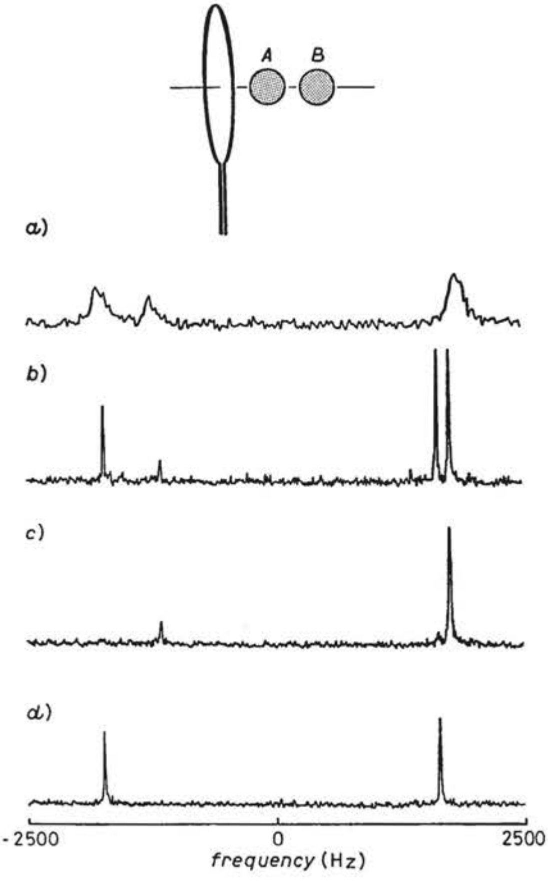

Fig. 1.29. – High-resolution surface coil experiment on two capillary tubes $A + B$ placed on axis at 2 and 4 mm from the coil. Tube A contained 3 μl of a ^{13}C-enriched alanine solution and B contained 2 μl ^{13}C-enriched ethanol. *a*) ^{13}C spectrum illustrating the inhomogeneous field. *b*) High-resolution SHARP spectrum, nonselective, implemented as described in the text. *c*) High-resolution SHARP spectrum, pulse times set for selectivity at A. *d*) SHARP spectrum, pulse times set for selectivity at B. (Adapted from *J. Am. Chem. Soc.*, **107**, 7193 (1985), with permission.)

taining ethanol and alanine. The pulse sequence used for this experiment was

$$(1.55)\qquad \left\{\begin{array}{llllllllll}
I(^1\mathrm{H})\left(\frac{\pi}{2}\right)_x & -\frac{\tau}{2}- & \pi & -\frac{\tau}{2}- & x\left(\frac{4t_1}{5}\right) & -\frac{\tau'}{2}- & \pi & -\frac{\tau'}{2}- & \frac{t_1}{5} & \text{-sample}(\pm), \\
S(^{13}\mathrm{C}) & & \pi & \frac{\pi}{2}(\pm) & & \frac{\pi}{2} & \pi & & \pi, &
\end{array}\right.$$

where $x(4t_1/5)$ implies continuous irradiation and the ± indicate that signals from experiments differing by 180° in phase are subtracted to further suppress nonsatellite peaks.

1'20. *Bilinear rotation pulses.*

– A further use of heteronuclear multiple-quantum coherence in heteronuclear spectroscopy in isotropic liquids is bilinear rotation decoupling (BIRD) [57], a method for the homonuclear decoupling of protons in weakly coupled liquid spin systems, which can be thought of as follows. Suppose a hard π pulse is applied to all protons and a π pulse is then applied to directly coupled ^{13}C-^{1}H pairs. This selective pulse restores to $+z$ all protons spins coupled directly to ^{13}C. The net effect is to invert all other spins, thus enabling them to be decoupled.

A pulse sequence that induces the bilinear rotation is

$$(1.56)\qquad \left\{\begin{array}{lllll}
I(^1\mathrm{H})\left(\frac{\pi}{2}\right) & -\frac{\tau}{2}- & \pi & -\frac{\tau}{2}- & \left(\frac{\pi}{2}\right). \\
S(^{13}\mathrm{C}) & & \pi & &
\end{array}\right.$$

If the Hamiltonian for the coupled I-S system is $H_{IS} = JI_z S_z$, then eq. (1.56) produces a propagator of the form $U(\tau) = \exp[-i2\pi\tau J I_y S_z]$. For $\tau = 1/J$ this propagator is a π pulse only for the directly bonded (satellite) protons. Bilinear rotation sequences have also been used in a variety of experiments in liquids to discriminate between one-bond and long-range couplings [58].

2. – Coherent-averaging theory.

2'1. *Introduction.*

– A recurring theme throughout these lectures is the requirement for the preparation or evolution of a system under a specified Hamiltonian or under a Hamiltonian with a particular symmetry or transformation properties. For example, in decoupling we attempt to make the effective coupling Hamiltonian zero. In multiple-quantum spectroscopy of solids we required a time-reversed detection with $H \sim H_{xx} - H_{yy}$. It is clearly necessary on many occasions to implement a specific desired Hamiltonian, perhaps different from the natural unperturbed Hamiltonian of the system. In other words, whereas the system might naturally evolve under its propagator $\boldsymbol{U}(t)$,

(2.1)

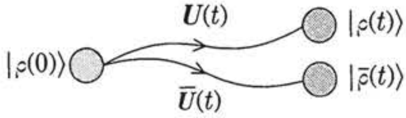

we apply a perturbation so that the system evolves under a different propagator $\overline{\boldsymbol{U}}(t)$, due to a Hamiltonian $\overline{H}$, arriving perhaps at a different state at time t. The perturbation needed may be a sequence of pulses or a mechanical rotation. For incoherent perturbations $\overline{\boldsymbol{U}}(t)$ may exist where $\overline{H}$ does not.

A theory that accounts well for the design of specific Hamiltonians (and, therefore, propagators) under coherent perturbation is coherent-averaging theory [59]. Suppose the Hamiltonian is time dependent (owing to, for example, an applied perturbation), as depicted in fig. 2.1. A question which arises is: can we find a time-independent Hamiltonian $\overline{H}$ which can induce evolution of the system through $\overline{\boldsymbol{U}}(t)$ to the same state as $H(t)$ would induce at time t? The answer is yes, that $\overline{H}$ is the Magnus Hamiltonian [60], given by

$$\overline{H} = \overline{H}^{(0)} + \overline{H}^{(1)} + \overline{H}^{(2)} + \dots, \tag{2.2}$$

where

$$\overline{H}^{(0)} = \frac{1}{t}\int_0^t H(t')\,\mathrm{d}t' \tag{2.3}$$

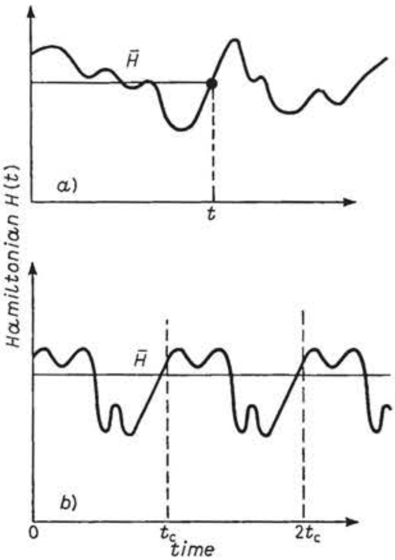

Fig. 2.1. – For a time-dependent Hamiltonian, the evolution can be often characterized by an effective time-independent average Hamiltonian $\overline{H}$. In general, if $H(t)$ is not periodic (a)), then $\overline{H}$ depends on t. If $H(t)$ is periodic (b)) then the same $\overline{H}$ is relevant for multiples of the period.

is the average Hamiltonian. The next two terms in this series are

$$\overline{H}^{(1)} = \frac{-i}{2t} \int_0^t \int_0^{t'} [H(t'), H(t'')]\, \mathrm{d}t''\, \mathrm{d}t' \,, \tag{2.4}$$

and

$$\overline{H}^{(2)} = -\frac{1}{6t} \int_0^t \int_0^{t'} \int_0^{t''} \{[H(t'),[H(t''), H(t''')]] + \\ +[H(t'''),[H(t''), H(t')]]\}\, \mathrm{d}t'''\, \mathrm{d}t''\, \mathrm{d}t' \,. \tag{2.5}$$

If eq. (2.2) converges rapidly, so that $\overline{H}^{(k)}$ are small for $k \neq 0$, then the average Hamiltonian $\overline{H}^{(0)}$ provides a good description of the system and the other $\overline{H}^{(k)}$ are correction terms. By applying a perturbation we have, therefore, taken a system which would have evolved under some Hamiltonian H and caused it to evolve effectively under $\overline{H}^{(0)}$ as in eq. (2.1). The trick is to implement the desired $\overline{H}^{(0)}$ by appropriate perturbations that can be realized experimentally, such as spin decoupling and time reversal. Note that, in general, $\overline{H}$ and $\overline{H}^{(0)}$ depend on t, but, if $H(t)$ is periodic, then the same $\overline{H}$ and $\overline{H}^{(0)}$ hold at all integer multiples of t_c. (If $H(t)$ is not periodic, the approach is still useful, since one can implement an $\overline{H}$ which provides a particular desired final state $|\bar{\rho}(t)\rangle$ at time t.)

Expressions (2.3) to (2.5) were used to calculate the time-reversal Hamiltonian of eq. (1.49) corresponding to the sequence of fig. 1.24, and they will be used repeatedly in the following sections. This approach has been useful in a variety of problems in different areas, for example truncation of couplings by high field [61-63], composite pulses [64-66], iterative schemes [67] and multiple-quantum operators [68, 69].

A particularly useful simplification occurs when the time-dependent Hamiltonian $H(t)$ commutes with itself at all times, i.e. $[H(t), H(t')] = 0$. In this case all $\overline{H}^{(k)} = 0$ for all $k \neq 0$, as we can see from eqs. (2.4) and (2.5) for $k = 1, 2$, and the average Hamiltonian $\overline{H}^{(0)}$ is exact. This happens for Carr-Purcell trains [70] and for magic-angle spinning [71] involving chemical-shift interactions [72] (and related cases such as dipolar couplings of N spins in a one-dimensional array, of which a pair of spins is the simplest example), dipolar couplings averaged by uniaxial molecular motion, heteronuclear dipolar couplings, or first-order quadrupolar coupling of isolated spins. We shall see that in this way it is possible to narrow the spectrum by magic-angle spinning even for broad quadrupolar spectra in solids.

2·2. *Multiple-pulse line narrowing.* – As an example of coherent averaging, we take the opportunity to review the WHH-4 multiple-pulse sequence [73] for removing the homonuclear dipolar interaction in solids. In this four-pulse se-

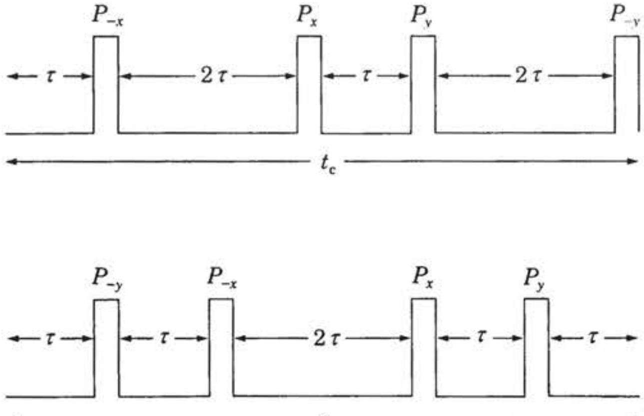

Fig. 2.2. – Pulse sequence for one cycle of the four-pulse WHH-4 multiple-pulse decoupling sequence. The signal is sampled in the center of the 2τ periods. Shifting the sequence by an amount τ to the left reveals the inherent symmetry, which ensures that all the odd-order correction terms in the Magnus Hamiltonian vanish.

quence, shown in fig. 2.2, the signal is observed stroboscopically during the sampling windows. The one-cycle propagator of the sequence can be written

$$U(t_c) = U_z(\tau)P_{\bar{x}}U_z(2\tau)P_xU_z(\tau)P_yU_z(2\tau)P_{\bar{y}}\,, \tag{2.6}$$

where

$$P_\alpha = \exp\left[-i\frac{\pi}{2}I_\alpha\right], \qquad P_{\bar{\alpha}} = \exp\left[-i\frac{\pi}{2}I_{\bar{\alpha}}\right]$$

and

$$U_\alpha(\tau) = \exp[-iH_{\alpha\alpha}\tau]\,, \qquad \alpha = \pm x,\ \pm y,\ \pm z\,.$$

We now move into the so-called «toggling rotating frame» by applying a transformation corresponding to the operation produced by the r.f. pulses to obtain

$$U(t_c) = U_z(\tau)U_y(2\tau)U_z(\tau)U_x(2\tau)\,. \tag{2.7}$$

Note that by shifting the cycle from the first sampling window to the second (as illustrated in fig. 2.2), we can rewrite eq. (2.7) as

$$U(t_c) = U_x(\tau)U_z(\tau)U_y(\tau)U_y(\tau)U_z(\tau)U_x(\tau)\,. \tag{2.8}$$

This is exactly equivalent to the expression of eq. (2.6), but it reveals that the sequence is in fact symmetric about its center. We are now in a position to evaluate the different terms in the Magnus expansion, to find

$$\overline{H}^{(0)} = \frac{1}{3}(H_{xx} + H_{yy} + H_{zz})\,, \tag{2.9}$$

which yields for the dipolar interaction

$$\overline{H}_{\mathrm{D}}^{(0)} = 0\,, \tag{2.10}$$

and for the chemical-shift interaction

$$\overline{H}_{\mathrm{CS}}^{(0)} = \sum_k \frac{1}{\sqrt{3}} (\omega_i^{(k)} + \Delta\omega) I_{111}^{(k)}\,, \tag{2.11}$$

where $I_{111}^{(k)} = I_x^{(k)} + I_y^{(k)} + I_z^{(k)}$. Thus, to zeroth order, the homonuclear dipolar interaction is removed by the WHH-4 sequence, and the chemical-shift interaction is scaled by a factor $1/\sqrt{3}$.

Because of the reflection symmetry, $\overline{H}^{(1)}$ and all of the odd-order correction terms vanish [74, 75], leaving the second-order terms as the leading corrections,

$$\begin{aligned}\overline{H}^{(2)} = \frac{\tau^2}{18}\big\{&[(H_{zz} + 2H_{xx} + 2H_{yy}), [(H_{xx} + H_{yy}), H_{zz}]] - \\ &-[(H_{yy} + 2H_{xx}), [H_{yy}, H_{xx}]]\big\}\,,\end{aligned} \tag{2.12}$$

which reduces to

$$\overline{H}_{\mathrm{D}}^{(2)} = \frac{\tau^2}{18}[(H_{\mathrm{D}xx} - H_{\mathrm{D}zz}), [H_{\mathrm{D}yy}, H_{\mathrm{D}xx}]] \tag{2.13}$$

for the dipolar interaction, and in the case of the chemical-shift interaction

$$\overline{H}_{\mathrm{CS}}^{(2)} = \frac{\tau^2}{18} \sum_k (\sigma_i^{(k)} + \Delta\omega)^3 (I_{yk} - 2I_{xk} + 4I_{zk})\,. \tag{2.14}$$

$\overline{H}_{\mathrm{D}}^{(2)}$ is responsible for the ultimate resolution available from the WHH-4 experiment on resonance (in the absence of pulse imperfections). Using coherent-averaging theory one can go on to calculate the effects of cross-terms between the chemical-shift and dipolar interactions, and the effect of pulse imperfections on the performance of the sequence in a relatively straightforward manner. In this way iterative schemes have been developed to compensate for such imperfections to higher and higher order, resulting in such advanced decoupling sequences as MREV-8 [76, 77], BLEW [78], BR-24 [79] and recent sequences from CORY [80].

2·3. *Magic-angle spinning.* – The WHH-4 sequence and other multiple-pulse techniques present methods for removing dipolar interactions by averaging in spin space. In this subsection we shall briefly show how averaging of the spatial coordinates by sample spinning leads to an average Hamiltonian in which the dipolar interaction is also removed [81, 82]. In sect. **5** we shall return to the issue of averaging under various schemes of sample reorientation, but from a group-theoretical perspective, and the example presented here serves as a useful comparison.

The truncated Hamiltonian in the rotating frame representing the chemical shift has the form [83]

$$H_0^{\mathrm{cs}} = \gamma\hbar A_{00}T_{00} + \gamma\hbar A_{20}T_{20}\,, \tag{2.15}$$

where A_{lm} and T_{lm} are irreducible spherical tensor components expressing the spatial and spin dependence of H, respectively. The heteronuclear dipolar and first-order quadrupolar interactions contain second-rank terms of the same form as those of eq. (2.15), and magic-angle spinning has an analogous effect on dipolar and first-order quadrupolar broadening as we derive here for the chemical shift. Note that the first term is isotropic, but that the second term depends on the orientation with respect to the external field.

Re-expressing $\boldsymbol{A}$ in a coordinate system fixed in the sample (rotor) which is rotating about an axis inclined by an angle Θ to the magnetic field, where the coordinates will be expressed by a_{lm}, we obtain

$$H_0^{\mathrm{cs}} = \gamma\hbar a_{00}\tau_{00} + \gamma\hbar\tau_{20}\sum_{m_1=-2}^{2} D_{m0}^{(2)}(\Omega_{\mathrm{sfc}}(t))\,a_{2m}\,. \tag{2.16}$$

Because of the invariance of the Hamiltonian to rotations about the main field, this coordinate transform only depends on Θ and $\phi = \omega_r t$. The matrix $\boldsymbol{a}$ can be diagonalized by a rotation $\Omega_{\mathrm{pas}} = (\alpha, \beta, \gamma)$ into its principal axis system, in which its components are written ρ_{lm},

$$a_{lm_1} = \sum_{m_2=-2}^{2} D_{m_2 m_1}^{(l)}(\Omega_{\mathrm{pas}})\,\rho_{lm_2}\,. \tag{2.17}$$

In this picture the only nonvanishing components are ρ_{00}, ρ_{20} and $\rho_{2\pm2}$, which are conventionally expressed as the isotropic chemical shift $\rho_{\iota} = \rho_{00}$, an anisotropy $\delta = \sqrt{2/3}\,\rho_{20}$ and an asymmetry parameter $\eta = \sqrt{6}\,\rho_{2,\pm2}/\rho_{20}$. Applying eq. (2.17) to eq. (2.16) we finally have an expression for the time-dependent Hamiltonian in the rotating frame

$$H_0^{\mathrm{cs}} = \gamma\hbar a_{00}\tau_{00} + \gamma\hbar\tau_{20}\sum_{m_1=-2}^{2} D_{m_1 0}^{(2)}(\Omega_{\mathrm{sfc}}(t)) \sum_{m_2=-2}^{2} D_{m_2 m_1}^{(2)}(\Omega_{\mathrm{pas}})\,\rho_{2m_2} \tag{2.18}$$

and expansion gives

$$\begin{aligned} H_0^{\mathrm{cs}} = {}& \gamma\hbar\rho_i\tau_{00} + \gamma\hbar\sqrt{\frac{3}{2}}\,\delta\tau_{20}\left\{\frac{1}{2}(3\cos^2\Theta - 1)\right\}\cdot \\ & \cdot\left\{\frac{1}{2}(3\cos^2\beta - 1) + \frac{\eta}{2}\sin^2\beta\cos 2\gamma\right\} + \gamma\hbar\sqrt{\frac{3}{2}}\,\delta\tau_{20}\,\xi_{\mathrm{MAS}}(t), \end{aligned} \tag{2.19}$$

where $\xi_{\mathrm{MAS}}(t)$ is an orientation-dependent function of the rotor phase [83].

Equation (2.19) demonstrates the spinning-induced periodicity of the spin Hamiltonian. A single rotor period $\phi(0 \to 2\pi)$ is periodic in the sense discussed above, and we can determine the average of the time-dependent terms using the Magnus expansion. Performing the integration of eq. (2.3) yields $\bar{\xi} = 0$ and eq. (2.19) becomes

$$\overline{H}^{(0)} = \gamma\hbar\rho_i\tau_{00} + \gamma\hbar\sqrt{\frac{3}{2}}\,\delta\tau_{20}\left\{\frac{1}{2}(3\cos^2\Theta - 1)\right\}\cdot \cdot\left\{\frac{1}{2}(3\cos^2\beta - 1) + \frac{\eta}{2}\sin^2\beta\cos 2\gamma\right\}. \tag{2.20}$$

If the angle of the spinning axis is chosen such that $3\cos^2\Theta - 1 = 0$, then we obtain a purely isotropic zeroth-order average Hamiltonian

$$\overline{H}^{(0)} = \gamma\hbar\rho_i\tau_{00}\,. \tag{2.21}$$

The conditions for the validity of this expression are that the series of eqs. (2.2)-(2.5) converges rapidly. In this case it converges as

$$\overline{H}^{(n+1)} \approx \frac{\Delta}{\omega_r}\overline{H}^{(n)}\,, \tag{2.22}$$

where Δ is the «size» of the interaction being averaged. Therefore, eq. (2.20) will provide an accurate description when $\omega_r \gg \Delta$. Although the spinning speed currently reaches as high as 30 kHz [84], there are many examples where this is not sufficient and the criterion $\omega_r \gg \Delta$ is not met. However, a special situation arises if the form of the Hamiltonian is such that the commutator in eq. (2.4) vanishes identically. In this case eq. (2.4) and all higher terms (which depend on the same commutator) disappear. This will be true when the interaction is inhomogeneous, *e.g.* when the spin terms in the Hamiltonian remain the same and they are only scaled under rotation. In the inhomogeneous case eq. (2.19) reduces under spinning at the magic angle to

$$H_0 = \gamma\hbar\rho_i\tau_{00} + \gamma\hbar\sqrt{\frac{3}{2}}\,\tau_{20}\,\delta\xi_{\mathrm{MAS}}(t)\,, \tag{2.23}$$

and the spectrum breaks up into a narrow centerband at the isotropic chemical shift and a series of narrow sidebands evenly spaced at a separation equal to the rotor frequency. Thus, even at relatively low speeds, magic-angle spinning allows us to obtain high-resolution spectra. As examples of the effect of magic-angle spinning fig. 2.3 shows an early result of the deuterium spectrum of a mixture of solid hexamethylbenzene and ferrocene [85], and fig. 2.4 shows a recent ^{27}Al magic-angle spinning spectrum of the full quadrupolar manifold (central and satellite transitions) for α-$\mathrm{Al_2O_3}$ which was used to determine the quadrupolar-coupling constants and asymmetry parameters for the two sites in this sample [86].

In order to average both homonuclear dipolar interactions and chemical-shift anisotropy it has proved necessary to combine the effects of multiple-pulse sequences and magic-angle spinning. The combined technique (CRAMPS) has provided resolved spectra for protons and fluorine [87, 88].

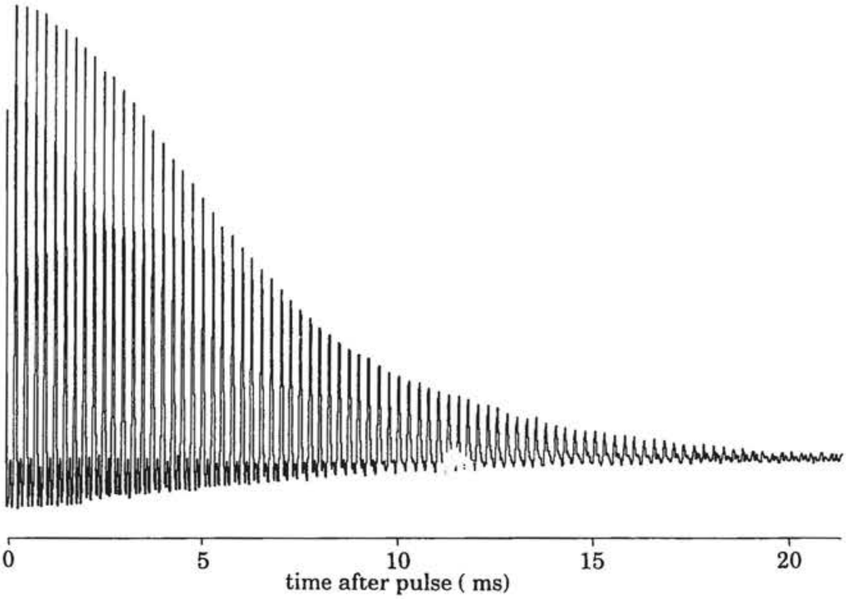

Fig. 2.3*a*. – Deuterium rotational echo train obtained from magic-angle spinning.

2'4. *Double rotation.* – If interactions of different nonzero ranks are present, it is sometimes not possible to average all the anisotropic interactions to zero by spinning about a single axis [81, 89-91]. This occurs, for example, in the case of second-order quadrupolar broadening. In sect. 5 we shall demonstrate how to solve the problem of simultaneously averaging two interactions on the basis of symmetry. Here we consider averaging over more sophisticated trajectories than simply spinning around a single axis, for which the average of all interactions is zero [92, 93].

In the case of the central transition of a half-integer quadrupolar nucleus the Hamiltonian for a static sample is

$$H_0^{\mathrm{Q}} = \sum_{l=0,2,4} C_l A_{l0} T_{l0} \, , \tag{2.24}$$

where the C_l are constants related to the quadrupolar coupling. The orientation dependence is expressed in terms of a sum of second- and fourth-rank tensors. We have seen above that after applying a rotation around a single axis the Hamiltonian is truncated along the rotation axis (if the spinning is fast enough), and the residual is then proportional to the Legendre polynomials $P_l(\cos\Theta)$. In this case $l = 2$ and 4, and spinning around a single axis will only partially narrow the line, since the roots of $P_2(\cos\Theta)$ and $P_4(\cos\Theta)$ do not coincide. However, applying another rotation relative to the first will further narrow the line. Solutions can be found which completely eliminate the second-order broadening with two rotations. In the double-rotation method (DOR) we spin around a first

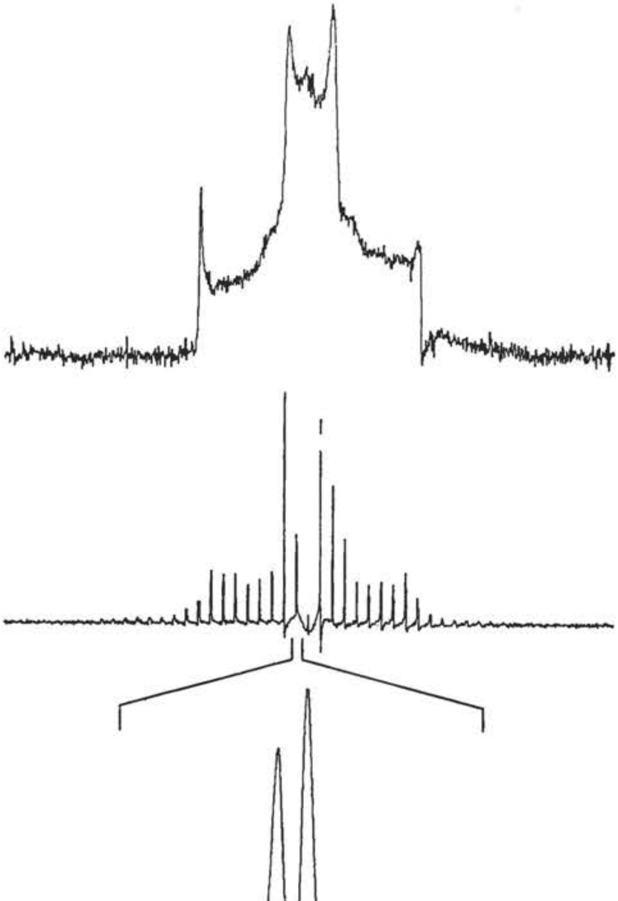

Fig. 2.3*b*. – Magic-angle spinning of deuterium in a solid mixture of deuterated hexamethylbenzene and deuterated ferrocene, demonstrating narrowing of the powder line even though the spinning frequency is considerably lower than the ~ 100 kHz quadrupolar broadened power linewidth. The two resonances at the bottom (expansion of the centerband in the middle trace) correspond to the isotropic chemical shifts of the two deuterated species. (Adapted from *Chem. Phys.*, **42**, 423 (1979), with permission.)

angle $\Theta_m^{(2)}$, the magic angle for P_2, and a second angle $\Theta_m^{(4)}$ which corresponds to one of the magic angles (30.56° or 70.12°) of the fourth-order Legendre polynomial. Rotation around two axes modifies eq. (2.24) to become

$$\omega = \sum_{l=0,2,4} C_l \tau_{l0} \sum_{m_1, m_2=-l}^{l} D_{m_1,0}^{(l)}(\Omega_{r_1}(t)) D_{m_2,m_1}^{(l)}(\Omega_{r_2}(t)) a_{lm_2}, \tag{2.25}$$

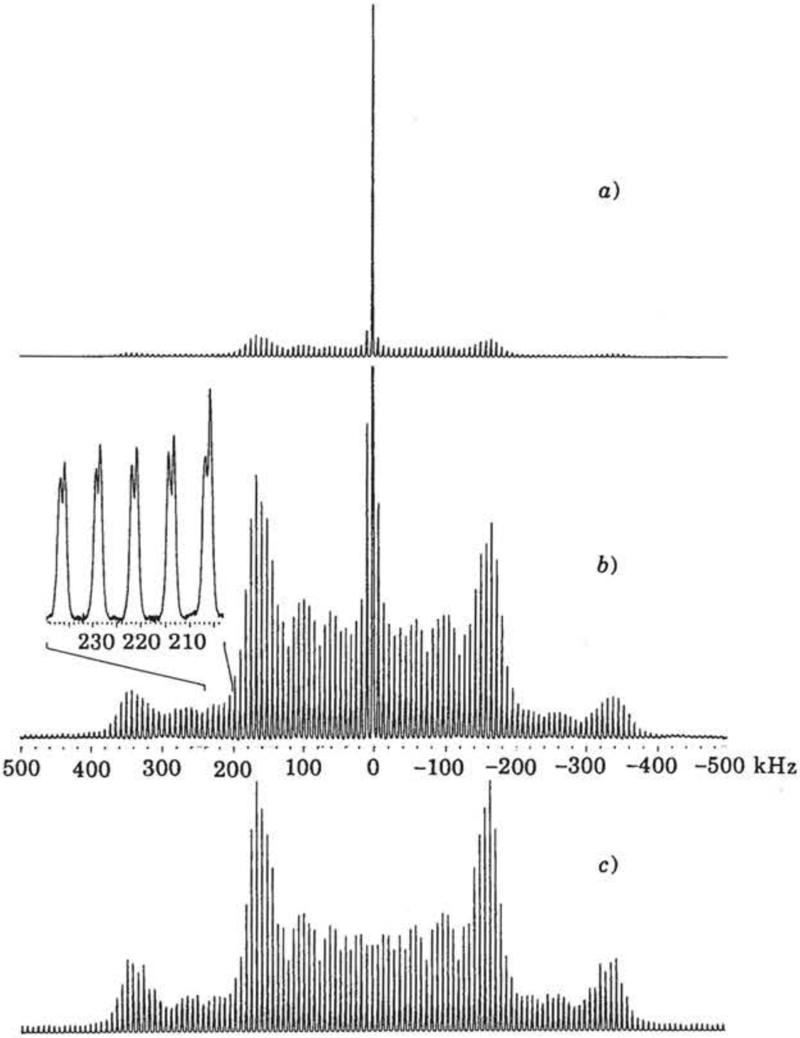

Fig. 2.4. – ^{27}Al MAS NMR spectra of the central and satellite transitions for α-Al_2O_3 spinning at 7.525 kHz. *a*) Experimental spectrum showing the relative intensities of the central and satellite transitions. *b*) Spectrum in *a*) with the vertical scale expanded by a factor of ten. The inset shows expansion of a region where the second-order quadrupole shift between the $(\pm 5/2, \pm 3/2)$ and the $(\pm 3/2, \pm 1/2)$ satellite transitions is clearly observed. *c*) Simulated spectrum for the satellite transitions obtained using a quadrupolar coupling $C_Q = 2.38$ MHz and $\eta = 0.00$. (Adapted from *J. Magn. Reson.*, 85, 173 (1989), with permission.)

where $\Omega_{r_1}(t)$ and $\Omega_{r_2}(t)$ are sets of Euler angles which define the transforms to the laboratory frame from the first, outer rotor frame, and to the outer rotor frame from the second, inner rotor frame, and where

$$a_{lm} = \sum_{m'=-l}^{l} D^{(l)}_{m',m}(\Omega_{\text{pas}})\, q_{lm'} .$$

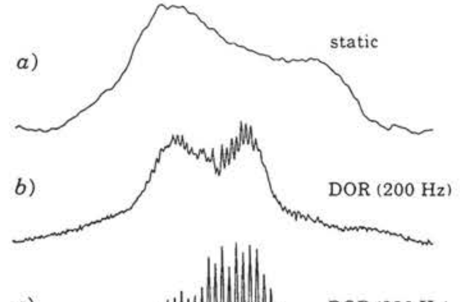

Fig. 2.5. – ^{23}Na DOR spectra of sodium oxalate spinning at various speeds, demonstrating the averaging of the second-order quadrupolar broadening and the effect of the time-dependent terms due to the slow outer rotor in eq. (2.25). There is only one type of ^{23}Na site in the crystal structure of this compound. (Adapted from *Solid State Nucl. Magn. Reson.*, **1**, 267 (1992), with permission.)

The $q_{lm'}$ are the elements of the quadrupolar-coupling tensor in its principal axis system.

After expansion of eq. (2.25) three terms result, similarly to the case of MAS:

$$\phi_{\mathrm{DOR}}(t) = C_0 a_{00} \tau_{20} + \sum_{l=2,4} C_l \tau_{l0} \sum_{m=-l}^{l} d^{(l)}_{-m,0}(\Theta_{r_1})\, d^{(l)}_{m,-m}(\Theta_{r_2})\, a_{l,-m} + \xi_{\mathrm{DOR}}(t), \tag{2.26}$$

where $\xi_{\mathrm{DOR}}(t)$ is a time-dependent term which depends on the rotation axes and the rotation rates; it is dependent on both orientation and time. The first term in eq. (2.26) corresponds to the isotropic shift and is a scalar, independent of both orientation and time. The second term is dependent on orientation but not time. As in the MAS example, we can average over $\xi_{\mathrm{DOR}}(t)$ *if at least one of the*

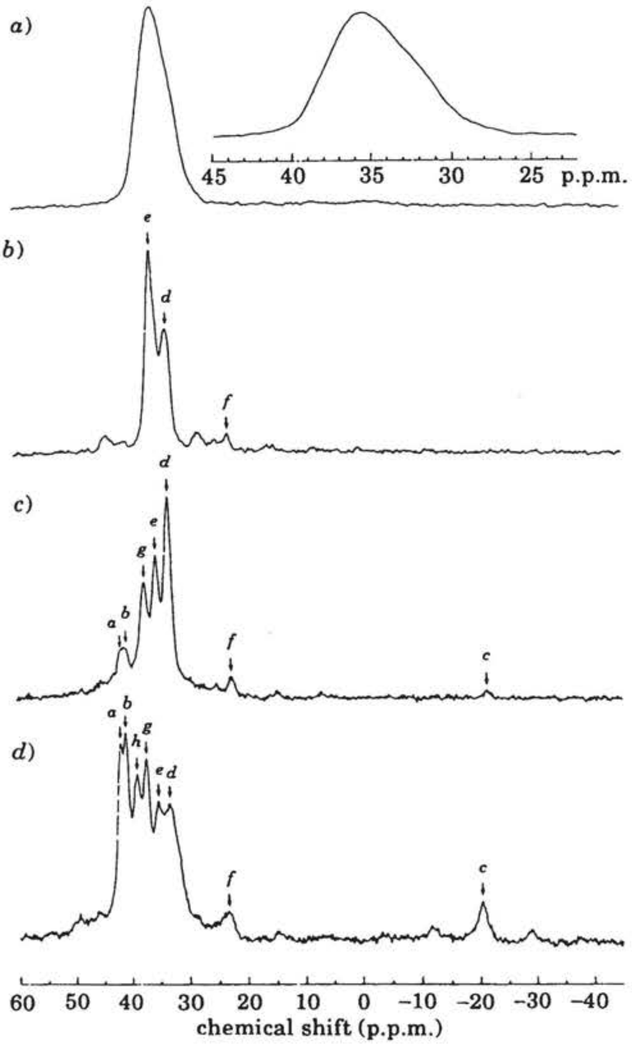

Fig. 2.6. – ^{27}Al NMR spectra of dehydrated and partially rehydrated VPI-5: *a*) MAS spectrum of dehydrated VPI-5, *b*) DOR spectrum of dehydrated VPI-5, *c*) DOR spectrum after two days of rehydration, *d*) DOR spectrum after 23 days of rehydration. (Adapted from *Nature* (*London*), **346**, 550 (1990), with permission.)

double-rotation rates is large compared to the interaction strength, in which case the third term averages to zero. Since

$$d_{00}^{(l)}(\Theta) = P_l(\cos\Theta), \tag{2.27}$$

we can eliminate the second term in eq. (2.26) if

$$P_2(\cos\Theta_{r_1})\,P_2(\cos\Theta_{r_2}) = 0 \tag{2.28}$$

and

$$P_4(\cos\Theta_{r_1})\,P_4(\cos\Theta_{r_2}) = 0\,. \tag{2.29}$$

The solutions are $\Theta_{r_1} = \Theta_m^{(2)}$ and $\Theta_{r_2} = \Theta_m^{(4)}$ or *vice versa*.

In the case where the spinning is not sufficiently fast to allow us to neglect $\xi_{\mathrm{DOR}}(t)$, it leads to the presence of sidebands in an exactly analogous manner to the time-dependent term in the MAS example and this is demonstrated in the example of the ^{23}Na DOR spectra shown in fig. 2.5 [94]. As an example of the type of resolution that can be obtained for the important case of ^{27}Al by this method, fig. 2.6 shows a DOR spectrum of ^{27}Al in VPI-5 [95].

3. – Spin decoupling.

3·1. *Spin $I = 1/2$ pair.* – Maintaining a theme of multiple-quantum effects and coherent averaging, we shall show in this section how one may achieve double-quantum decoupling. However, to prepare ourselves we must first consider the decoupling of a spin $I = 1/2$ from an observed spin $S = 1/2$. The I spin is irradiated near resonance with an r.f. field of amplitude ω_1. In the rotating frame the Hamiltonian is

$$H = H_0 + H_{IS}\,, \tag{3.1}$$

where

$$H_0 = -\Delta\omega I_z - \omega_1 I_x \tag{3.2}$$

describes the I fields in the rotating frame in frequency units and

$$H_{IS} = dI_z S_z \tag{3.3}$$

is the I-S coupling. We now transform to a tilted frame with z along the effective I field. The tilt operator is given by

$$T = \exp[-i\theta I_y]\,, \tag{3.4}$$

where

$$\cos\theta = \frac{\Delta\omega}{(\omega_1^2 + \Delta\omega^2)^{1/2}} = \frac{\Delta\omega}{\omega_{\mathrm{e}}}\,. \tag{3.5}$$

In this frame

$$H = -\omega_{\mathrm{e}} I_z + dS_z(I_z\cos\theta - I_x\cos\theta)$$

and

$$\omega_{\mathrm{e}} = \sqrt{\omega_1^2 + \Delta\omega^2}\,. \tag{3.6}$$

We now go into a frame defined by $-\omega_{\mathrm{e}} I_z$ and take the average Hamiltonian of the I-S coupling term (as described in sect. 2), obtaining

$$\overline{H}_{IS}^{(0)} = d\cos\theta S_z I_z\,, \tag{3.7}$$

$$\overline{H}_{IS}^{(1)} = d^2\sin\theta\frac{1}{\omega_e}S_z^2\left(\cos\theta I_x - \frac{1}{2}\sin\theta I_z\right), \tag{3.8}$$

and, at resonance ($\Delta\omega = 0$, $\theta = \pi/2$),

$$\overline{H}_{IS}^{(2)} = \frac{d^3}{2\omega_1^2}S_z^3 I_x\,. \tag{3.9}$$

For a spin $S = 1/2$ the term $\overline{H}_{IS}^{(1)}$ in eq. (3.8) commutes with the spin vector $\boldsymbol{S}$, so only $\overline{H}_{IS}^{(0)}$ and $\overline{H}_{IS}^{(2)}$ are relevant.

3·2. *One-quantum offset and* r.f. *amplitude dependence.* – Away from resonance where $\Delta\omega \neq 0$, the effective coupling between I and S is dominated by $\overline{H}_{IS}^{(0)}$, and the decoupling efficiency δ_S (roughly the relative S linewidth) goes as

$$\delta_S \sim \cos\theta = \frac{\Delta\omega}{(\omega_1^2+\Delta\omega^2)^{1/2}}\,. \tag{3.10}$$

Thus for small $\Delta\omega$, more precisely $d \ll \Delta\omega \ll \omega_1$, the S linewidth should depend linearly on $\Delta\omega$.

At resonance ($\Delta\omega = 0$) the dominant term is $\overline{H}_{IS}^{(2)}$, and we expect

$$\delta_S \sim \left(\frac{d}{\omega_1}\right)^2, \tag{3.11}$$

i.e. the decoupling efficiency should increase (the S linewidth should decrease) inverse quadratically with ω_1 ($\delta_S \sim 1/\omega_1^2$) for large ω_1.

We note here that the $\cos\theta$ factor is a scaling of an I_z term analogous to scaling of chemical shifts or resonance offsets due to strong irradiation off resonance. We have recognized that this scaling originates from the same source as the «mysterious» geometrical phase factor in certain closed-circuit adiabatic processes, which we shall discuss in sect. **9**. As mentioned in subsect. 2·1, more efficient and robust spin decoupling can be achieved by means of iterative schemes.

Iterative schemes rely on the realization that only $H^{(0)}$ of eq. (2.2) is important for heteronuclear decoupling [65, 96] and that $H^{(0)}$ can be made more and more insensitive to imperfections (such as offset) by constructing supercycles of composite 90° or 180° pulses. For example, the original MLEV-4 sequence consists of the cycle [97]

$$RR\overline{R}\overline{R}\,, \tag{3.12}$$

where the basic element R of the supercycle is a composite 180° pulse such as

$$R = (90°)_x\text{-}(180°)_y\text{-}(90°)_x \tag{3.13}$$

and $\overline{R}$ is the same as R with all the phases reversed. This sequence was subsequently iteratively expanded to yield the MLEV-16 decoupling sequence [98]

$$RR\overline{R}\,\overline{R}\;\;\overline{R}RR\overline{R}\;\;\overline{R}\,\overline{R}RR\;\;R\overline{R}\,\overline{R}R\,. \tag{3.14}$$

Similar methods can be used to expand 90° composite pulses into supercycles, one of the most successful being WALTZ-16, which corresponds to the sequence [99, 100]

$$\bar{3}4\bar{2}3\bar{1}2\bar{4}2\bar{3}\;\;3\bar{4}2\bar{3}1\bar{2}4\bar{2}3\;\;3\bar{4}2\bar{3}1\bar{2}4\bar{2}3\;\;\bar{3}4\bar{2}3\bar{1}2\bar{4}2\bar{3}\,, \tag{3.15}$$

where the elements 1, 2, 3 and 4 correspond to 90°, 180°, 270° and 360° pulses, respectively. In fig. 3.1 we show the performance of WALTZ-16 with respect to offset from the transmitter frequency.

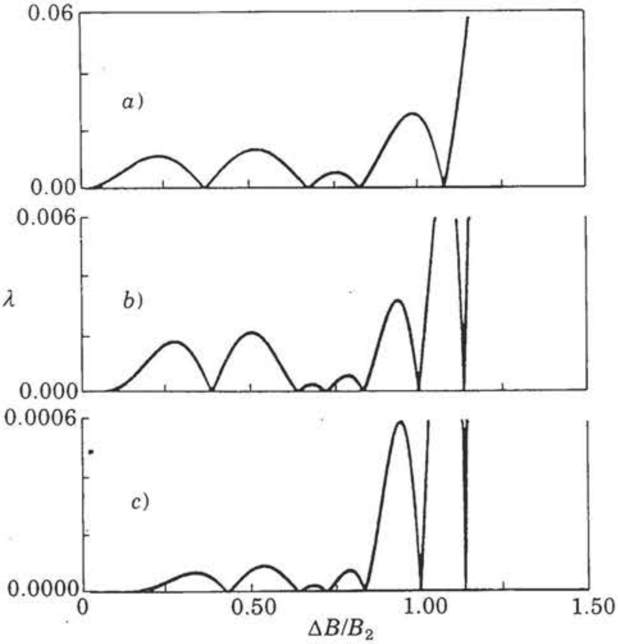

Fig. 3.1. – The predicted scaling factors delivered by the *a*) WALTZ-4, *b*) WALTZ-8 and *c*) WALTZ-16 sequences. Note the order-of-magnitude expansion of the vertical scale at each stage. The improvement is fastest near resonance and falls off towards the edge at each stage. (Adapted from *Prog. Nucl. Magn. Reson. Spectrosc.*, **19**, 47 (1987), with permission.)

3.3. *Double-quantum decoupling.* – Imagine that we are required to decouple a spin $I = 1$, say a deuterium spin, from a spin $S = 1/2$, say a proton. Such would be the case, for example, in experiments on large biological molecules where isotopic substitution has been performed in order to simplify the spin system. If the deuterium quadrupole splitting is large (recall fig. 1.10), it may be impossible to cover the full I spectrum with a sufficiently large ω_1 field [101, 102]. However, if we irradiate at the unperturbed Zeeman resonance $\omega = \omega_0$, then the double-quantum transitions $M = 1 \leftrightarrow M = -1$ should make decoupling possible, since the $M = 0$ state exerts no z field at the S spin. A rough estimate of the condition can be made as follows. If the quadrupole coupling ω_Q is much larger than the I-S coupling (*e.g.*, $\omega_Q \sim 100\,\text{kHz}$ for deuterium), then for normal one-quantum decoupling we would require

$$\omega_1 \gg \omega_Q\,, \tag{3.16}$$

a challenging technical demand with current NMR technology. This requirement is to be contrasted with the much less demanding condition

$$\omega_1 \gg d \tag{3.17}$$

for the $S = 1/2$, $I = 1/2$ pair with dipolar couplings d, according to eq. (3.3).

If we excite the double-quantum transition, however, then according to second-order perturbation theory [103] (matrix element squared divided by energy difference) the transitions between $M = 1$ and $M = -1$ occur with an amplitude

$$\omega_1^{\text{DQ}} \sim \frac{\omega_1^2}{\omega_Q}\,. \tag{3.18}$$

The effective double-quantum amplitude is to be compared with the coupling d; hence we now require

$$\frac{\omega_1^2}{\omega_Q} \gg d\,, \tag{3.19}$$

i.e.

$$\omega_1 \gg \sqrt{d\omega_Q}\,, \tag{3.20}$$

which is much more easily implemented than eq. (3.16) for the usual case where $d \ll \omega_Q$ [101, 102, 104-106].

3.4. *Double-quantum offset and* r.f. *amplitude dependence.* – To appreciate the sensitivity of double-quantum decoupling to resonance offset $\Delta\omega$ and r.f. amplitude ω_1, we adopt eqs. (3.10) and (3.11), substituting ω_1^2/ω_Q for ω_1 and

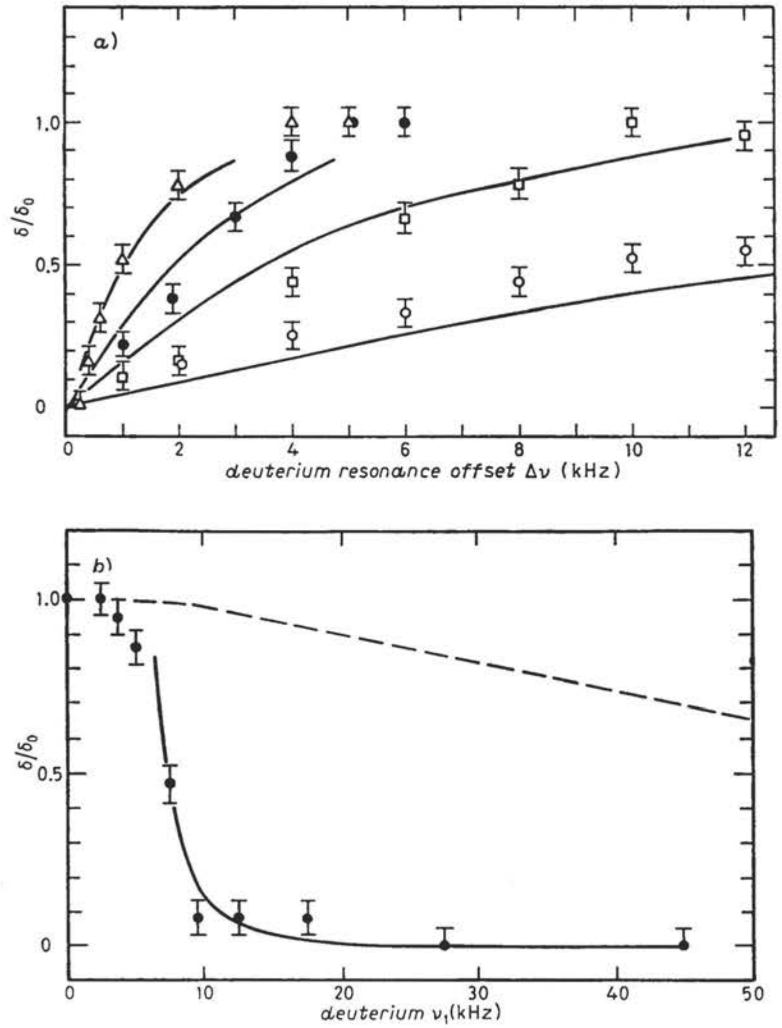

Fig. 3.2. – *a*) Proton linewidth in solid DMSO-d_6 (99%) at − 75 °C under deuterium double-quantum decoupling as the deuterium spins are irradiated at various frequencies $\Delta\nu$ from resonance: △ $\nu_1 = 12.5\,\text{kHz}$, ● $\nu_1 = 17.0\,\text{kHz}$, □ $\nu_1 = 23.0\,\text{kHz}$, ○ $\nu_1 = 45.0\,\text{kHz}$. δ/δ_0 corresponds to δ_S in the text. Note the sensitivity of the decoupling to the I resonance condition, a characteristic of the double-quantum decoupling process. The solid lines are from theoretical calculations. *b*) Proton linewidth in solid DMSO-d_6 (99%) at − 75 °C as the deuterium spins are irradiated at resonance with various values of ω_1 to induce double-quantum decoupling. The solid line shows the asymptotic $1/\omega_1^4$ behavior expected from theory. The dashed line shows the expected behavior if the double-quantum transition did not occur. (Adapted from *Phys. Rev. B*, **18**, 112 (1978), with permission.)

$2\Delta\omega$ for $\Delta\omega$. For double-quantum decoupling, the S linewidth is given by

$$\delta_S \sim \cos\theta = \frac{2(\Delta\omega)\,\omega_Q}{(\omega_1^4 + 4\Delta\omega^2\omega_Q^2)^{1/2}} \tag{3.21}$$

thus making the resonance condition for decoupling much more sensitive than in one-quantum decoupling, since $\Delta\omega$ *is multiplied by* ω_Q.

At resonance

$$\delta_S \sim \frac{d^2\,\omega_Q^2}{\omega_1^4}\,, \tag{3.22}$$

so decoupling begins only when $\omega_1 \sim (d\omega_Q)^{1/2}$. The subsequent dependence on ω_1 is much more rapid, going as the inverse fourth power. All this behavior has been quantitatively verified, and examples are shown in fig. 3.2. Double-quan-

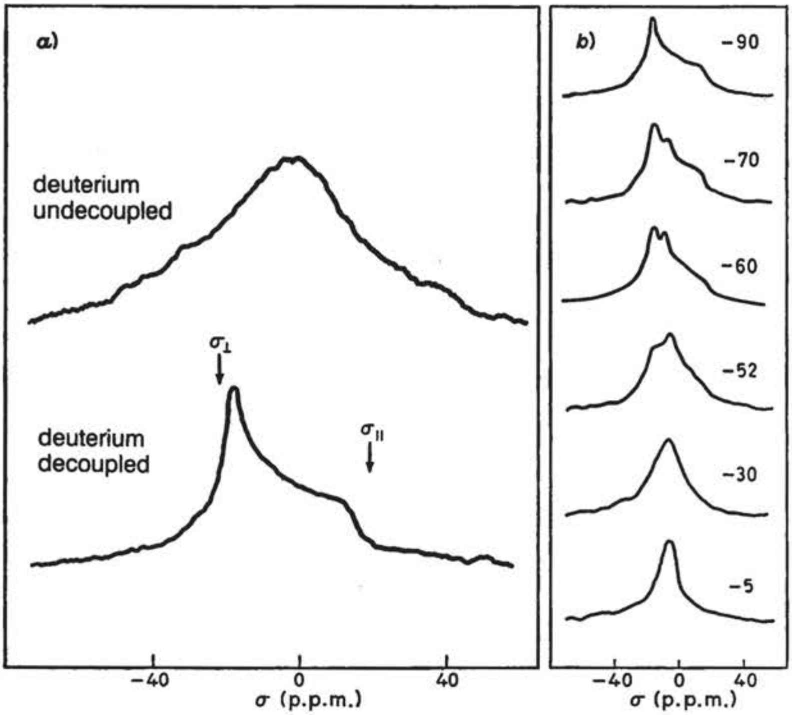

Fig. 3.3. – *a*) NMR spectra of residual protons in heavy ice (99% deuterium) at − 90 °C with and without deuterium decoupling. The chemical-shift anisotropy of the protons in the hydrogen bonds is ~ 34 p.p.m. *b*) As the temperature is raised, the spectra exhibit motional narrowing, with lineshapes characteristic of tetrahedral jumps. This behavior is consistent with the protons hopping between the four hydrogen bonds around the oxygens. (Courtesy of D. E. WEMMER.)

tum decoupling has been used in our laboratory to obtain high-resolution spectra of diluted protons displaying, for example, proton chemical-shift anisotropy for the hydrogen bonds in solid heavy ice, and to observe the effects of the tetrahedral motion of the protons on the NMR lineshapes as ice is heated towards its melting point (see sect. 5). Typical proton spectra of 99% deuterated ice with deuterium double-quantum decoupling are shown in fig. 3.3. As the ice is heated, the effects of motional narrowing are observed [107]. A few degrees below the melting temperature the line is that of an isotropic sample. The intermediate spectra indicate that *the protons are jumping between the tetrahedrally disposed hydrogen bonds around the oxygens.*

3·5. *Comment on the relationship between spin decoupling and multiple-quantum excitation.* – Consider a system of N I spins (*e.g.*, protons) coupled to a S spin (*e.g.*, ^{13}C). Several schemes involving composite pulses and iterative sequences have been devised to effect spin decoupling in such systems. These sequences, employing phase shifts and permutations, are reminiscent of some of the selective n-quantum schemes described in subsect. **1**·16. There must be some relationship between the two areas. Indeed, suppose we could engineer a pure $(N+1)$-quantum selective scheme to excite the I spins. *Since N spins cannot absorb or emit more than N quanta, such an excitation would be tantamount to implementing the unit propagator, i.e.* decoupling. In this sense decoupling schemes employing π pulses and π phase shifts are two-quantum selective (good for decoupling one spin) and multiple-pulse schemes involving $\pi/2$ pulses and $\pi/2$ phase shifts are four-quantum selective and decouple groups of spins.

4. – Interaction of radiation and matter.

4·1. *Two-level system in a quantized field.* – A common question is where are the quanta, the *photons*, in a multiple-quantum experiment? When we say $\Delta M = 2$, are there two quanta really involved or just one off-resonance quantum at double the frequency? What is the relationship to optical multiphoton excitation [108]? To investigate these questions clearly, we would like to study the very simplest case where photons actually appear. In order to do so, it is necessary to bring the radiation field as a legitimate full-fledged partner into the treatment, and not just treat it semi-classically as a time-dependent perturbation on the spins. That way, we can «see» the photons in the field and count them. At the same time this treatment will remind us of Feynman's analogy [109] of any two-level system to a spin $I = 1/2$. Later we shall encounter generalizations of this analogy, *e.g.*, a three-level system to a spin $I = 1$, and so on. The treatment also reminds us of the analogies, often unhappily neglected, between NMR and optical spectroscopy.

Before we treat two-quantum phenomena, let us review the simplest one-quantum problem, a two-level system interacting with a single mode of a cavity (the Jaynes-Cummings model [110]), described by a time-independent Hamiltonian

$$H = H_{\text{mat}} + H_{\text{rad}} + H_{\text{int}}. \tag{4.1}$$

H_{mat} is the matter Hamiltonian, the matter being the system (atom or spin) irradiated and behavior observed. We assume it consists of two states, 1 and 2, with energies $\hbar\omega_1$ and $\hbar\omega_2$, such that

$$\omega_2 - \omega_1 = \omega_0 . \tag{4.2}$$

Assume further that the particles occupying these states are fermions [111] with coupling λ. Since at most one can occupy each state, the possible states are

$$|0, 0\rangle, \qquad |0, 1\rangle, \qquad |1, 0\rangle, \qquad |1, 1\rangle, \tag{4.3}$$

where $|0, 1\rangle$ is the vacuum for particle 1 and single occupancy for particle 2, etc. We now introduce fermion operators $c_1, c_1^\dagger, c_2, c_2^\dagger$ such that

$$\begin{cases} c_1^\dagger\,|0, k\rangle = |1, k\rangle, \\ c_1^\dagger\,|1, k\rangle = |0, k\rangle, \end{cases} \tag{4.4}$$

and similarly for $c_2, c_2^\dagger$ and $|j, 0\rangle$, $|j, 1\rangle$. All other operations yield zero. The fermion operators satisfy the anticommutation rule

$$\{c_1, c_1^\dagger\} = \{c_2, c_2^\dagger\} = 1 . \tag{4.5}$$

The matter Hamiltonian is given in terms of these operators by

$$H_{\text{mat}} = \hbar\omega_1 c_1^\dagger c_1 + \hbar\omega_2 c_2^\dagger c_2 . \tag{4.6}$$

H_{rad} in eq. (4.1) is the radiation Hamiltonian, which we write in terms of the photon creation and destruction operators for a single mode, a and $a^\dagger$, with frequency ω and eigenkets $|n\rangle$ (n = number of photons) [112]. We remember that for a harmonic oscillator we have

$$\begin{cases} a^\dagger\,|n\rangle = \sqrt{n+1}\,|n+1\rangle, \\ a\,|n+1\rangle = \sqrt{n+1}\,|n\rangle. \end{cases} \tag{4.7}$$

The commutation rules are

$$\begin{cases} [a, a] = [a^\dagger, a^\dagger] = 0 , \\ [a, a^\dagger] = 1 , \end{cases} \tag{4.8}$$

and the Hamiltonian, ignoring the zero-point energy, is

$$H_{\text{rad}} = \hbar\omega a^\dagger a . \tag{4.9}$$

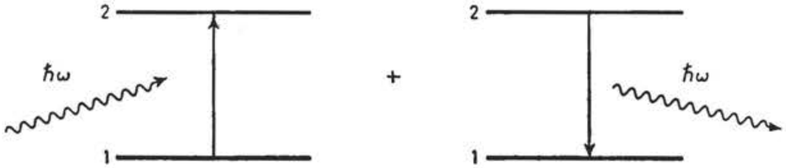

Fig. 4.1. – Two coupling events between a spin $I = 1/2$ or fictitious spin $I = 1/2$ and photons in the cavity. A photon is absorbed and the spin is excited, or a photon is emitted and the spin returns to the ground state. This corresponds to the semi-classical rotating-wave approximation.

For H_{int} of eq. (4.1), the interaction between the radiation and the matter, we assume the coupling depicted in fig. 4.1. A photon $\hbar\omega$ is absorbed, transforming particle 1 into 2, or one is emitted, transforming particle 2 into 1; *i.e.*

$$H_{\text{int}} = \frac{\hbar\lambda}{2}(c_1 c_2^\dagger a + c_1^\dagger c_2 a^\dagger)\,. \tag{4.10}$$

This coupling conserves energy for $\omega = \omega_0$ and incorporates the semi-classical rotating-wave approximation (note that we have neglected events in which a photon is absorbed and transforms particle 2 into 1, for example). Equations (4.6), (4.9) and (4.10) now can be collected into the total Hamiltonian in eq. (4.1) to give

$$H = \hbar\omega_1 c_1^\dagger c_1 + \hbar\omega_2 c_2^\dagger c_2 + \frac{\hbar\lambda}{2}(c_1 c_2^\dagger a + c_1^\dagger c_2 a^\dagger)\,. \tag{4.11}$$

4·2. *Fictitious spin $I = 1/2$ operators.* – At this point we introduce the fictitious spin $I = 1/2$ operators [27-29]

$$\begin{cases} I_x = \dfrac{1}{2}(c_1^\dagger c_2 + c_1 c_2^\dagger)\,, \\ I_y = \dfrac{-i}{2}(c_1^\dagger c_2 - c_1 c_2^\dagger)\,, \\ I_z = \dfrac{1}{2}(c_1^\dagger c_1 - c_2^\dagger c_2)\,. \end{cases} \tag{4.12}$$

Given the relationships of eqs. (4.4) and (4.5), it can be verified that

$$[I_x, I_y] = iI_z\,, \tag{4.13}$$

with the eigenstates $|\pm\rangle$ of I_z defined as

$$I_z|\pm\rangle = \pm\frac{1}{2}|\pm\rangle \tag{4.14}$$

and

$$I_{\pm} = I_x \pm iI_y\,, \tag{4.15}$$

the Hamiltonian eq. (4.11) can be written, aside from a commuting operator (remember that the number of particles is conserved), as

$$H = -\hbar\omega_0 I_z + \hbar\omega a^{\dagger} a + \frac{\hbar\lambda}{2}(a^{\dagger} I_- + aI_+)\,. \tag{4.16}$$

This Hamiltonian is identical to that of a spin $I = 1/2$ interacting with the cavity mode. Now assume the cavity mode is at resonance ($\omega = \omega_0$), and transform to an interaction picture defined by

$$R(t) = \exp[-it(-\omega_0 I_z + \omega a^{\dagger} a)]\,. \tag{4.17}$$

This is the analog of the rotating frame for the full quantum problem. As usual, this transformation simplifies considerably the Hamiltonian, which is now given by

$$H = \frac{\hbar\lambda}{2}(a^{\dagger} I_- + aI_+)\,. \tag{4.18}$$

4·3. *Evolution of the two-level system.* – Imagine the initial state $|\psi(0)\rangle$ being the excited state $|-\rangle$ for the fictitious spin with n photons in the cavity, as depicted in fig. 4.2:

$$|\psi(0)\rangle = |-, n\rangle\,. \tag{4.19}$$

The evolution of $|\psi\rangle$ is given by

$$|\psi(t)\rangle = \exp\left[-\frac{i}{\hbar}Ht\right]\psi(0)\,, \tag{4.20}$$

which is easily evaluated using the Hamiltonian of eq. (4.18) together with eqs. (4.7) and (4.15) to yield

$$|\psi(t)\rangle = |-, n\rangle \cos\sqrt{n+1}\,\frac{\lambda t}{2} - |+, n+1\rangle\, i \sin\sqrt{n+1}\,\frac{\lambda t}{2}\,. \tag{4.21}$$

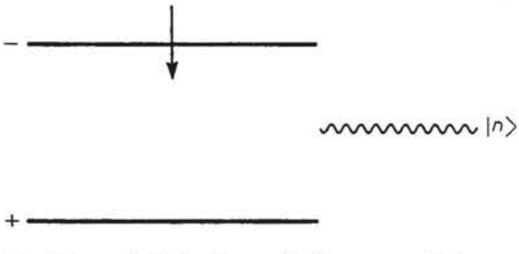

Fig. 4.2. – Initial state. The spin is in the excited state and there are n photons in the field.

This expression describes a quantum Rabi oscillation [113] or nutation that periodically exchanges a photon between the cavity and the spin. The analogy to the usual semi-classical problem of spin $I = 1/2$ interacting with a resonance field of amplitude ω_1 is made by realizing that

$$\lambda\sqrt{n+1} \leftrightarrow \omega_1 \, . \tag{4.22}$$

Note, however, that, even when there are initially no photons in the cavity ($n = 0$), there is still the evolution, corresponding to spontaneous emission from the excited-spin or two-level system. Note also that, for a 2π pulse

$$\omega_1 t = \sqrt{n+1}\,\lambda t = 2\pi \, , \tag{4.23}$$

the ket $|\psi(0)\rangle$ does not come back to itself but instead to $\cos\pi$ times itself, *i.e.*

$$|\psi(2\pi)\rangle = -\,|\psi(0)\rangle \, . \tag{4.24}$$

This effect corresponds to the well-known spinor behavior [114, 115] of a system with an even number of states or of a nonintegral fictitious spin, which we shall discuss further in sect. **9**.

4·4. *Evolution off resonance.* – The expression of eq. (4.21) derived for resonance ($\omega = \omega_0$) can be generalized for arbitrary frequency of the mode ω in eq. (4.16). This extension is best made by transforming to a tilted interaction picture in analogy to eq. (3.4). The result, for the initial condition of eq. (4.19), is

$$|\psi(t)\rangle = |-, n\rangle[\cos\lambda_e t/2 - i\cos\theta\sin\lambda_e t/2] - |+, n+1\rangle\, i\sin\theta\sin\lambda_e t/2 \, , \tag{4.25}$$

where

$$\lambda_e = (\lambda^2(n+1) + (\omega_0 - \omega)^2)^{1/2} \, , \tag{4.26}$$

$$\sin\theta = \sqrt{n+1}\,\lambda/\lambda_e \, . \tag{4.27}$$

4·5. *Adiabatic rapid passage.* – The treatment above provides an elegant picture of adiabatic rapid passage for a two-level system or fictitious spin $I = 1/2$. Consider fig. 4.3, which depicts the energy levels of the uncoupled matter and radiation Hamiltonians

$$H_0 = H_{\text{mat}} + H_{\text{rad}} \tag{4.28}$$

as the frequency (or field) is varied through resonance. The resonance between matter and radiation occurs at the level crossings, $\omega = \omega_0$. Adding the interaction Hamiltonian H_{int} causes a mixing of the states near resonance, which gives rise to an avoided crossing as in fig. 4.4. The repulsion between levels at resonance depends on the number of photons in the cavity as $(n+1)^{1/2}\lambda$, the semiclassical field intensity ω_1 [116] from eq. (4.22).

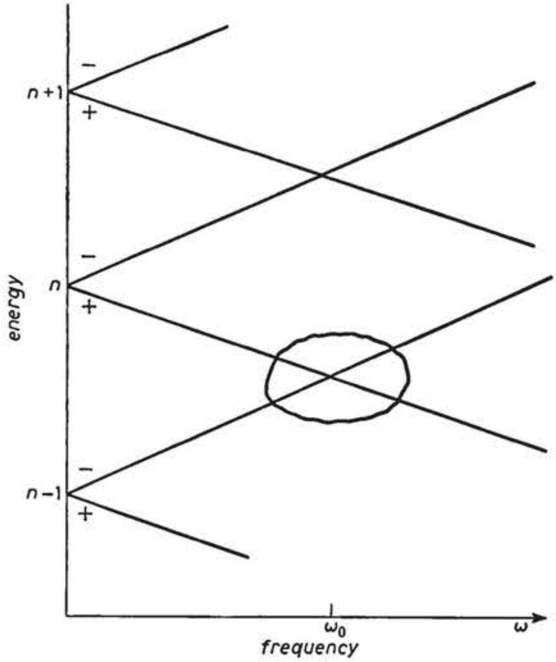

Fig. 4.3. – Energy level diagram for a spin $I = 1/2$ or fictitious spin $I = 1/2$ (two-level system) and a quantized radiation field with photon states $|n\rangle$.

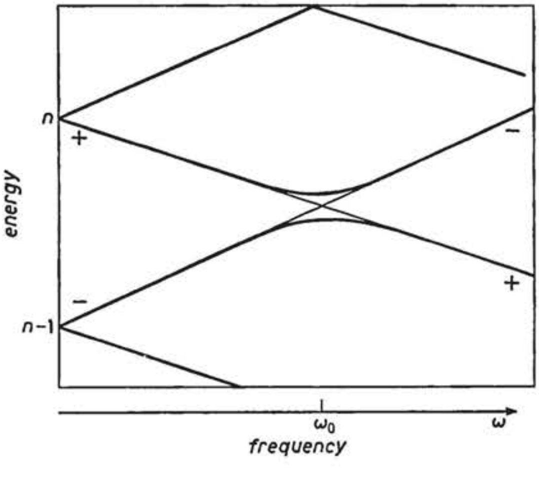

Fig. 4.4. – Coupling between the spin $I = 1/2$ and the radiation causes a level anticrossing at the resonance. From this picture it is easy to visualize how adiabatic rapid passage interchanges the ± states.

If we begin with the spin (or fictitious spin) in one state away from resonance, *e.g.* $|-, n\rangle$ on the left of fig. 4.4, and now shift the frequency *adiabatically* [117] through resonance, then we recall from quantum mechanics that the system remains in an eigenstate. Thus it will go to $|+, n-1\rangle$ on the right-hand side. Therefore, sweeping through a resonance line rapidly compared to T_1 but slowly enough so there are no frequency components at ω_0 should invert a resonance line whether we sweep from left to right or right to left. This effect is called population inversion by adiabatic rapid passage, an extremely useful way of making robust π pulses. *The most efficient adiabatic sweeps are not linear (i.e. linear dependence of frequency on time), however, but rather are hyperbolic functions* [118].

4·6. *Three-level system in a quantized field.* – We adopt the notation of subsect. 4·3 for three particles interacting with the single mode of a cavity; we assume that only 1 and 2 or 2 and 3 can be directly interconnected by energy-conserving (rotating-wave) absorption or emission of a single photon. Thus the interaction is depicted in fig. 4.5*a*), with

$$\begin{cases} \omega_{12} + \omega_{23} = 2\omega_0 \,, \\ \omega_{12} - \omega_{23} = 2\omega_Q \,. \end{cases} \tag{4.29}$$

The full Hamiltonian for this system,

$$H = \hbar\omega_1 c_1^\dagger c_1 + \hbar\omega_2 c_2^\dagger c_2 + \hbar\omega_3 c_3^\dagger c_3 + \hbar\omega a^\dagger a + \\ + \frac{\hbar\lambda}{\sqrt{2}}(c_1 c_2^\dagger a + c_1^\dagger c_2 a^\dagger) + \frac{\hbar\lambda'}{\sqrt{2}}(c_2 c_3^\dagger a + c_2^\dagger c_3 a^\dagger) \,, \tag{4.30}$$

is entirely analogous to eq. (4.11). We will not discuss the general case here, but will instead select simple conditions under which double-quantum behavior emerges [119].

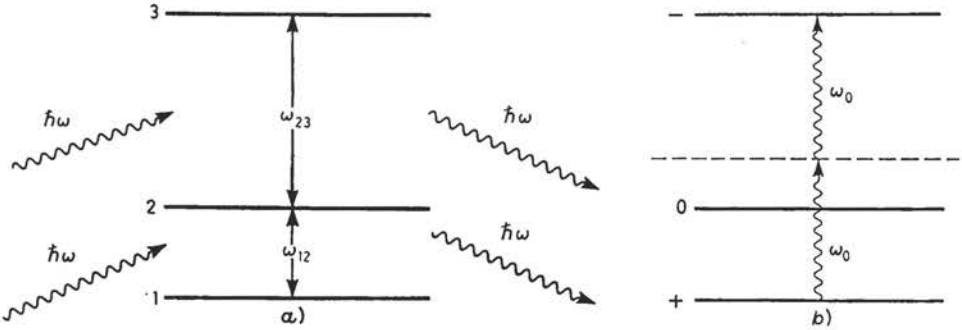

Fig. 4.5. – *a*) Coupling events between a spin $I = 1$ and photons in a cavity. *b*) Resonant two-photon process in a three-level spin $I = 1$ system.

4·7. *Fictitious spin $I = 1$ operators.* – First let us introduce the fictitious spin $I = 1$ operators

$$\text{(4.31)}\qquad \begin{cases} I_z = c_1^\dagger c_1 - c_3^\dagger c_3\,, & Q_z = 2c_2^\dagger c_2 - c_3^\dagger c_3 - c_1^\dagger c_1\,,\\ I_+ = c_1 c_2^\dagger + c_2 c_3^\dagger\,, & Q_+ = c_2 c_3^\dagger - c_1 c_2^\dagger\,,\\ I_- = c_1^\dagger c_2 + c_2^\dagger c_3\,, & Q_- = c_2^\dagger c_3 - c_1^\dagger c_2\,,\\ Q_{+2} = c_1 c_3^\dagger\,, & Q_{-2} = c_1^\dagger c_3\,. \end{cases}$$

Here the raising and lowering operators are used directly without going through any intermediate stages involving I_x, Q_x, Q_{xy}, etc. Inserting these spin $I = 1$ operators in eq. (4.30) and ignoring commuting unit operators (again, number of particles is conserved), we can rewrite H as

$$\text{(4.32)}\qquad H = \hbar\omega_0 I_z + \frac{\hbar\omega_{\mathrm{Q}}}{3} Q_z + \hbar\omega a^\dagger a + \frac{\hbar}{2\sqrt{2}}[(\lambda - \lambda')Q_+ + (\lambda + \lambda')I_+]a + \\ + \frac{\hbar}{2\sqrt{2}}[(\lambda - \lambda')Q_- + (\lambda + \lambda')I_-]a^\dagger\,.$$

We now specialize to the case in which the two allowed one-quantum absorptions and emissions have the same matrix elements,

$$\text{(4.33)}\qquad \lambda = \lambda'\,,$$

so that

$$\text{(4.34)}\qquad H = -\hbar\omega_0 I_z + \frac{\hbar\omega_{\mathrm{Q}}}{3} Q_z + \hbar\omega a^\dagger a + \frac{\hbar\lambda}{\sqrt{2}}(I_+ a + I_- a^\dagger)\,.$$

This Hamiltonian is just the interaction of a quadrupolar spin $I = 1$ with Zeeman frequency ω_0 and quadrupolar frequency ω_{Q}. Now assume the radiation is at resonance ($\omega = \omega_0$) and that it is weak compared to the quadrupolar splitting,

$$\text{(4.35)}\qquad \lambda\sqrt{n+1} \ll \omega_{\mathrm{Q}}\,,$$

corresponding to the situation in fig. 4.5*b*). Note that this condition embodies the weaker case in which

$$\text{(4.36)}\qquad \lambda \ll \omega_{\mathrm{Q}}\,.$$

4·8. *Double-quantum (two-photon) Hamiltonian.* – In the interaction picture defined by eq. (4.17), the Hamiltonian of eq. (4.34) can be written

$$\text{(4.37)}\qquad H = H_{\mathrm{Q}} + H_1 = \frac{\hbar\omega_{\mathrm{Q}}}{3} + \frac{\hbar\lambda}{\sqrt{2}}(I_+ a + I_- a^\dagger)\,.$$

With the condition of eq. (4.36) we now have a situation ideal for a perturbation treatment since the second operator term H_1 in eq. (4.37) is much smaller than the first term H_Q. It is appropriate to retain only the «secular» part of the interaction term, *i.e.* that part diagonal with respect to the first term. We carry this out using Van Vleck perturbation theory [61] as follows. First, define an infinitesimal transformation

$$H = \exp[-iS]H\exp[iS] \simeq H - i[S, H] + \dots, \tag{4.38}$$

where S is an infinitesimal Hermitian operator. Substituting eq. (4.38) into eq. (4.37), we get

$$H = H_Q + H_1 - i[S, H_Q] - i[S, H_1]\dots. \tag{4.39}$$

Now we demand that the first-order infinitesimal term vanish, so that

$$H_1 - i[S, H_Q] = 0, \tag{4.40}$$

which reduces eq. (4.35) to

$$H' \simeq H_Q + H_1' \tag{4.41}$$

with the modified interaction Hamiltonian

$$H_1' = \frac{-i}{2}[S, H_1]. \tag{4.42}$$

After some algebra the S which satisfies eq. (4.40) is found to be

$$S = -i\frac{\lambda}{\omega_Q\sqrt{2}}(Q_+ a - Q_- a^\dagger). \tag{4.43}$$

Evaluating the commutator in eq. (4.42) with eq. (4.43), we obtain the effective interaction Hamiltonian (neglecting terms commuting with H_Q)

$$H_1' = \frac{\hbar\lambda^2}{2\omega_Q}(Q_{+2}a^2 + Q_{-2}a^{\dagger 2}). \tag{4.44}$$

According to the definitons of $Q_{\pm 2}$ and a, $a^\dagger$ given in eqs. (4.7) and (4.31), this form is a pure double-quantum Hamiltonian with the appealing property that it exhibits the two *photons* directly in the terms a^2 and $a^{\dagger 2}$. These terms represent the destruction and creation of only pairs of photons.

4·9. *Evolution of the system.* – If the system begins in the upper state as shown in fig. 4.6 with n photons in the cavity, *i.e.*

$$|\psi(0)\rangle = |-, n\rangle, \tag{4.45}$$

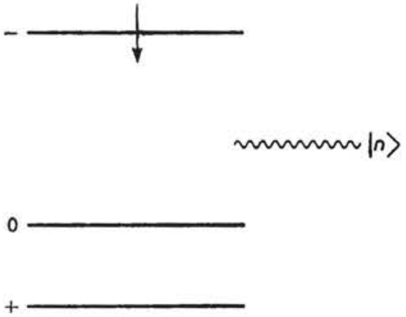

Fig. 4.6. – Initial state. The spin is in the excited state and there are n photons in the cavity.

then under the influence of the Hamiltonian of eq. (4.44) the system evolves as

$$|\psi(t)\rangle = |-, n\rangle \cos \sqrt{(n+1)(n+2)}\,\frac{\lambda^{(2)}t}{2} - \\ - |+, n+2\rangle\, i \sin \sqrt{(n+1)(n+2)}\,\frac{\lambda^{(2)}t}{2}\,, \tag{4.46}$$

where $\lambda^{(2)}$ is the effective two-photon amplitude

$$\lambda^{(2)} = \frac{\lambda^2}{\omega_Q}\,. \tag{4.47}$$

This result is to be compared with eq. (4.21). *Here two photons are being exchanged with the cavity; a two-photon Rabi oscillation.*

The correspondence to the semi-classical case is given by

$$\frac{\lambda^2}{\omega_Q}\sqrt{(n+1)(n+2)} \sim \frac{\lambda^2 n}{\omega_Q} \leftrightarrow \frac{\omega_1^2}{\omega_Q}\,. \tag{4.48}$$

When we begin with no photons in the cavity, eq. (4.46) corresponds to two-photon spontaneous emission. This process, incidentally, is how metastable He $(1s, 2s)$ decays by optical emission to the ground state.

4·10. *Double-quantum adiabatic rapid passage.* – The energy levels of the three-level system and cavity photons with no coupling between them appear in fig. 4.7. There are now three relevant crossings indicated in the circle, two corresponding to normal one-quantum resonances and the one we have just described due to a double-quantum resonance at ω_0. With the interaction between matter and radiation, all three crossings are avoided, as shown for the case $\lambda^2((n+1)(n+2))^{1/2} \ll \omega_Q^2$ in fig. 4.8, roughly $\lambda(n+1)^{1/2} \ll \omega_Q$ as stated in eq. (4.35). The levels at the two one-quantum resonances repel by $\sim \lambda(n+1)^{1/2}$,

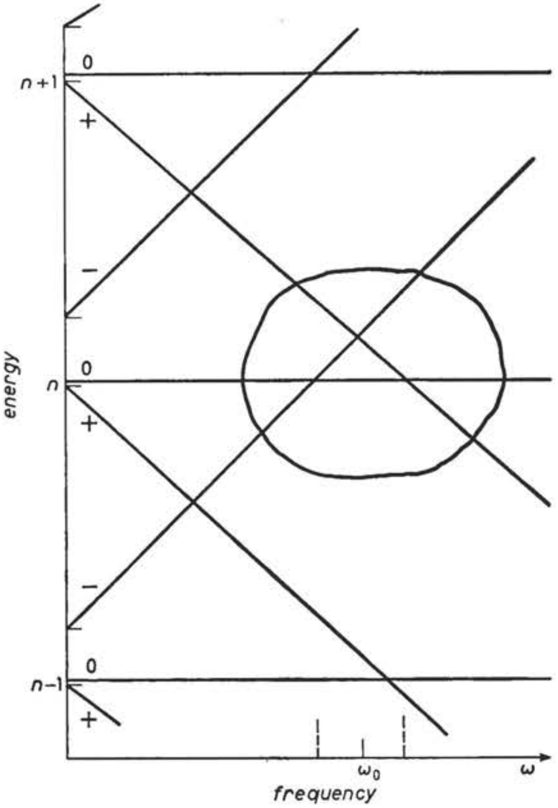

Fig. 4.7. – Energy level diagram for a spin $I = 1$ or fictitious spin $I = 1$ (three-level system) and a quantized radiation field with photon states $|n\rangle$.

whereas those at the double-quantum resonance experience the weaker repulsion $\sim \lambda^2((n+1)(n+2))^{1/2}/\omega_Q$. Thus the adiabatic condition for the double-quantum resonance is considerably more stringent than that for the one-quantum resonances.

Several interesting features are exposed in the diagram of fig. 4.8. The resonances of a three-level system can be inverted by adiabatically sweeping either through all the transitions or only through the double-quantum transition. Individual one-quantum transitions may be inverted by selectively sweeping through them adiabatically. *If we sweep adiabatically to the right through the left resonance and then through the double-quantum resonance, the left line is inverted; if we sweep to the left first through the double-quantum resonance, and then through the left one-quantum resonance, the left line does not invert* [119]. The intensities of each are also affected. This phenomenon was first observed in experiments on spin $I = 1$ nuclei in crystals, where lines would sometimes invert with adiabatic rapid passage in one direction but not in the

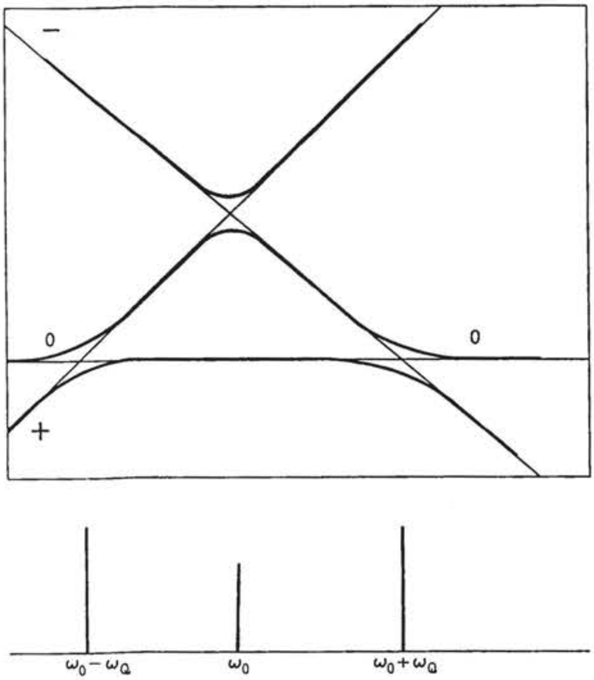

Fig. 4.8. – Coupling between the spin $I = 1$ and the radiation causes level anticrossing. There are two one-photon anticrossings and one two-photon anticrossing. It is possible by adiabatic rapid passage to interchange 0 and −, 0 and + or the ± states. The latter is a two-photon (double-quantum NMR) adiabatic rapid passage.

other. It is, of course, possible to sweep so that passage through the one-quantum transitions is adiabatic, whereas passage through the double-quantum transition is not. If passage through the double-quantum transition is sudden enough compared with the level repulsion, then the system behaves as if the levels cross at ω_0 and there is no double-quantum inversion. Generalizations of these considerations to higher spin and to coupled spins is straightforward.

We note in closing that all arguments concerning adiabatic rapid passage can, of course, be made using traditional semi-classical NMR considerations.

5. – Group theory and dynamics.

In this section we discuss the treatment of dynamic effects in NMR in the presence of symmetry. The two most common motional mechanisms that give rise to such dynamic effects in the solid state are molecular motion (or chemical exchange) [120, 121] and macroscopic reorientational motion of the sample, the latter usually implemented for the purposes of narrowing or simplifying the spectrum.

5·1. *Molecular motion.* – The effects of symmetry can be appreciated by considering fig. 5.1. A molecule undergoes motion subject to the symmetry G and the motion is investigated by means of an NMR observable characterized by subgroup $g \subset G$. The purpose of the NMR experiment is to provide information about the parameters (for example, the molecular jump rates) of the molecular motion. Now, if the probe has a high enough symmetry, $g = G$, the NMR spectrum is *invariant* to the motion and we can learn nothing further from the spectrum about the parameters of the motion. For the case where the probe has no symmetry subgroup of G except the trivial group C_1, it should be possible to derive, from the NMR spectra, all the parameters of the motion.

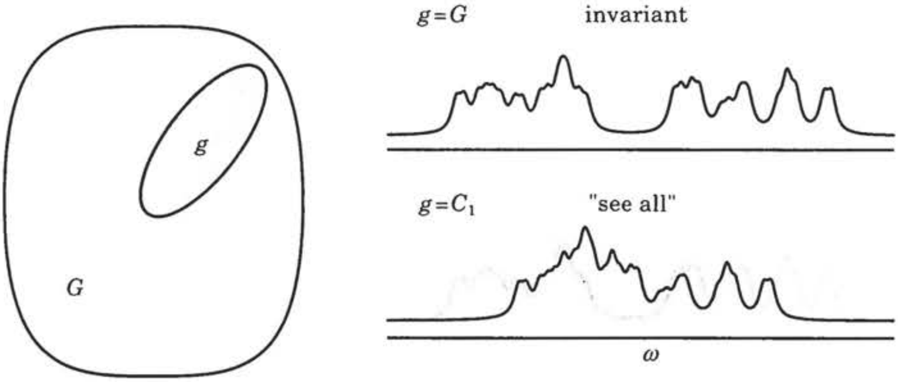

Fig. 5.1. – If a molecule undergoes motion subject to symmetry group G, and the motion is investigated by a probe of symmetry subgroup $g \subset G$, the spectrum is invariant to the motion if $g = G$, but, if the probe contains no symmetry subgroup of G except C_1, it should be possible to derive all the parameters of the motion from the spectrum.

A simple, but realistic example is depicted in fig. 5.2. In this case, the motion consists of 180° flips (with flip rate W_{12}) of a water molecule in a crystal about its C_{2v} axis. If the NMR probe is the dipolar coupling between the two protons, the spectrum is invariant to the motion since the axis of the dipolar interaction is left unchanged by the jump (fig. 5.2*a*)). In contrast, if the NMR probe has its principal axis roughly along the OH bond as, for example, the chemical shift or deuterium quadrupole coupling, the spectrum displays the classical effects of chemical exchange, collapsing to a motionally averaged spectrum (one line for the chemical shift, and a doublet for the quadrupole coupling) at high temperature, and W_{12} may be extracted from the spectra.

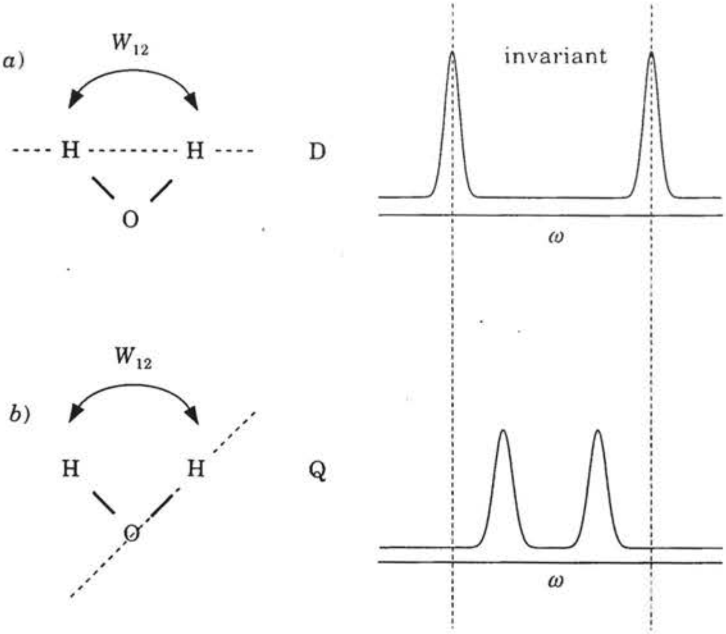

Fig. 5.2. – If the proton dipolar interaction is used to probe the 180° flip about the C_{2v} axis of water of hydration in a crystal, no change in the spectrum is observed since the dipolar interaction is invariant to this motion. On the contrary, if the chemical shift or deuterium quadrupolar interaction were used in place of the dipolar interaction, the motion would have the effect of narrowing the spectrum as illustrated schematically (for the quadrupolar coupling) in the lower part of the figure.

An interesting question is how much can we learn about the motion, how many parameters can be extracted, in the *intermediate* case, where g has a non-trivial symmetry, but less than G[122-124]. Consider, for example, the carbon spectrum of solid benzene. The relevant motion involves 60° jumps (or multiples thereof) about the C_6 axis of the molecule, with jump parameters W_{12}, W_{13}, W_{14},

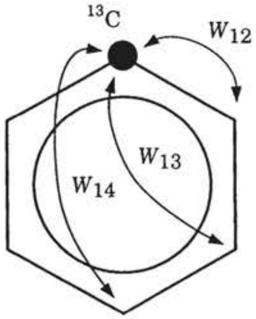

Fig. 5.3. – Jump motions and rates in benzene.

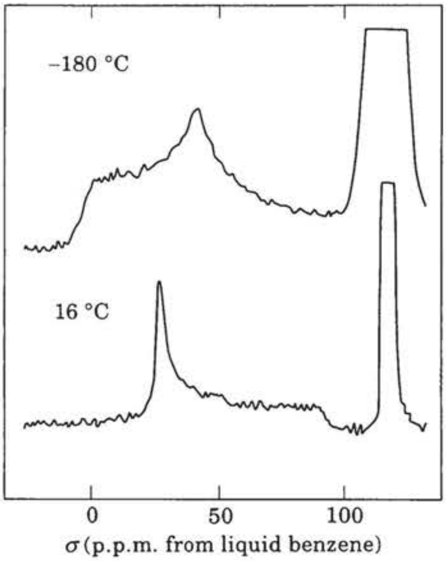

Fig. 5.4. – ^{13}C powder spectra of hexamethyl benzene in the high- and low-temperature limits. The wide peaks are from the ring carbons and the sharp peaks, which have been truncated, are from the methyl carbons. (Courtesy of D. E. WEMMER.)

as illustrated schematically in fig. 5.3 [125]. Here, the chemical-shift tensor has a (nontrivial) symmetry less than that of the molecular jumps, and we expect that the NMR spectra should not provide sufficient information to determine all three parameters. An experimental example of the motional averaging is shown in fig. 5.4.

5˙2. *Group theory and exchange.* – In this subsection we follow the treatment of Alexander, Baram and Luz [123]. In the simplest case, the Bloch equations [126] for the magnetization, y_j, of a spin in site j are

$$\alpha_j y_j = P_j \,, \tag{5.1}$$

where

$$\alpha_j = i(\omega - \omega_j) - T_{2j}^{-1} \tag{5.2}$$

and ω and T_{2j} are the Larmor frequency and transverse relaxation time in the j-th site. In the presence of molecular jumps, the magnetization is exchanged between sites [127-129]

$$\alpha_j y_j + \sum_k W_{jk}(y_k - y_j) = P_j \,, \tag{5.3}$$

where W_{jk} is the transition rate from j to k. Now consider the effect of symmetry on eqs. (5.1)-(5.3) [130]. Let the symmetry of the molecular dynamics be G. The y_k form the basis for a reducible representation of G, and each W_{jk} may be associated with a group element R in G,

$$R_\alpha y_j = y_k \,, \tag{5.4}$$

so that we may write

$$W_{jk} = W(R_\alpha)\,. \tag{5.5}$$

Moreover, since the $W(R_\alpha)$ are determined by the symmetry of G, *all equivalent elements (those belonging to the same class C) have the same rate* W_c, so we can rewrite eq. (5.3) as

$$\alpha_j y_j + \sum_c W_c \sum_{\alpha \in C} (R_\alpha - E)\, y_j = P_j\,. \tag{5.6}$$

We expand the y_j in terms of basis functions $g_{\lambda\mu}$ of the group G

$$y_j = \sum_{\lambda\mu} a^j_{\lambda\mu}\, g_{\lambda\mu} = \sum_\lambda g_{\lambda j}\,, \tag{5.7}$$

where λ labels the irreducible representation and μ is an index of the row in a multidimensional representation. The coefficients $a^j_{\lambda\mu}$ are uniquely determined from G in terms of projection operators formed from the group elements. From group theory, for any $g_{\lambda\mu}$ acted on by the sum of elements in a class [130]

$$\sum_{\alpha \in C} R_\alpha g_{\lambda\mu} = n_c \frac{\chi^\lambda_c}{\nu_\lambda} g_{\lambda\mu}\,, \tag{5.8}$$

where n_c is the order of the class C, χ^λ_c is the character, and n_λ the dimensionality of the λ representation. Thus eq. (5.6) becomes

$$\alpha_j y_j - \sum_c W_c n_c \sum_\lambda \left(1 - \frac{\chi^\lambda_c}{\nu_\lambda}\right) g_{j\lambda} = P_j\,,$$

which can be simplified to yield

$$\alpha_j y_j - \sum_\lambda W_\lambda g_{j\lambda} = P_j \tag{5.9}$$

by defining W_λ, the rate for the representation, as

$$W_\lambda = \sum_c W_c n_c \left(1 - \frac{\chi^\lambda_c}{\nu_\lambda}\right). \tag{5.10}$$

Thus we have replaced the summation over individual rates for exchange between sites with rates for the irreducible representations of the symmetry group for the exchange [131].

5˙3. *Relevant representations.* – The symmetry may be used to simplify the analysis even further, by recognizing that not all irreducible representations l

are needed. Because we observe only the total magnetization

$$y = \sum_j y_j \,, \tag{5.11}$$

which transforms according to the totally symmetric representation A_1 of G, only those representations of G which mix with (couple to) A_1 by the observable are relevant; these *relevant representations* of G are those which, when reduced (decomposed) under g, contain only the totally symmetric representation of g. That is, if

$$N_\lambda = \sum_c n_c \chi_c^\lambda \chi_c^{A_1} \tag{5.12}$$

is not zero, the λ representation is relevant and must be included in the summation. Noting from eq. (5.10) that $W_{A_1} = 0$ in every case, it is clear that *there exists one independent motional parameter for each relevant representation (beyond* A_1). Indeed, in the case where there is just one relevant representation, Γ beyond A_1, there is a simple analytical solution for the spectral lineshape [125]:

$$y(\omega) = \frac{\dfrac{P}{W_\Gamma} \displaystyle\sum_j \frac{1}{\alpha_j - W_\Gamma}}{\dfrac{N}{W_\Gamma} + \displaystyle\sum_j \frac{1}{\alpha_j - W_\Gamma}} \,. \tag{5.13}$$

5·4. *Summary of symmetry considerations.* – To sum up what we have derived above, the effect of motion on the spectrum is determined by the relative

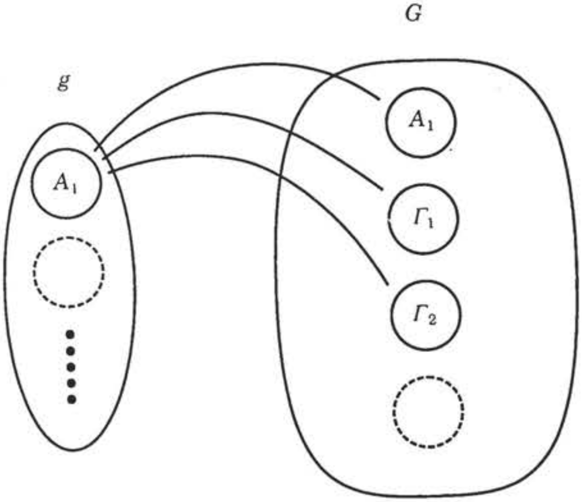

Fig. 5.5. – Relevant representations of G are determined by using character tables to find which elements of G contain the totally symmetric representation of g.

symmetry of the interaction we use to probe the motion (the observable magnetization with symmetry group g) and the symmetry of the dynamics (symmetry group G). If $g = G$ or if g has a higher symmetry than G, then only the A_1 representation of G is relevant, and the spectrum will be invariant to the motion. If g has a lower symmetry than G, then the spectrum will be at least partially affected by the motion, and, if g has no symmetry subgroup of G ($g = C_1$), then the number of relevant representations is equal to the number of classes, and all the W_c can be determined. In general, the approach is to find the relevant representations of G (fig. 5.5) using the character tables for the groups, and then determine the W_λ in terms of the y_j using expression (5.10).

5·5. *Example: dynamics of solid benzene.* – The case of benzene provides an illustrative example of the symmetry considerations [125]. For the molecular symmetry of benzene, with the observable being the anisotropic chemical shift, we can assign $g = D_2$, which has the character table given in table I and contains four irreducible representations A_1, B_1, B_2 and B_3. The symmetry of the molecule in this case can be taken as D_6, with the character table also shown in table I, containing 6 irreducible representations, *only two of which* (A_1 *and* E_2) *contain* A_1 *of* D_2. Thus there are two relevant representations, which corre-

TABLE I. – *Character tables for the* D_2 *and* D_6 *groups.* The characters shown in boldface in the D_6 table correspond to the elements of the relevant representations with respect to the D_2 subgroup, namely those elements that do not sum to zero under D_2.

D_2	E	C_2^z	C_2^y	C_2^x
A_1	1	1	1	1
B_1	1	1	− 1	− 1
B_2	1	− 1	1	− 1
B_3	1	− 1	− 1	1

D_6	E	$2C_6$	$2C_3$	C_2	$3C_2'$	$3C_2''$
$\mathbf{A_1}$	**1**	**1**	**1**	**1**	**1**	**1**
A_2	1	1	1	1	− 1	− 1
B_1	1	− 1	1	− 1	1	− 1
B_2	1	− 1	1	− 1	− 1	1
E_1	2	1	− 1	− 2	0	0
$\mathbf{E_2}$	**2**	**− 1**	**− 1**	**2**	**0**	**0**

spond (from eq. (5.10)) to rates $W_{A_1} = 0$ and $W_{E_2} = W_{12} + W_{13}$. From group theory, we, therefore, expect that there is only one observable rate for the dynamic processes in solid benzene, the sum of the rate parameters for 60° and 120° jumps. This makes sense, because a 180° rotation does not affect the chemical shift (making W_{14} ineffective) and a process which consists of a 60° jump (W_{12}) cannot be distinguished, for example, from one which consists of a 180° jump followed by a $-120°$ jump (W_{13}), hence the sum $W_{12} + W_{13}$. Thus, while the experimental NMR spectra (fig. 5.6) clearly reflect the effects of the sixfold symmetry in the motion, they cannot teach us about 60° *vs.* 120° jumps. In contrast, in the case of fivefold symmetry, W_{12} (72°) and W_{13} (144°) can be determined separately [132].

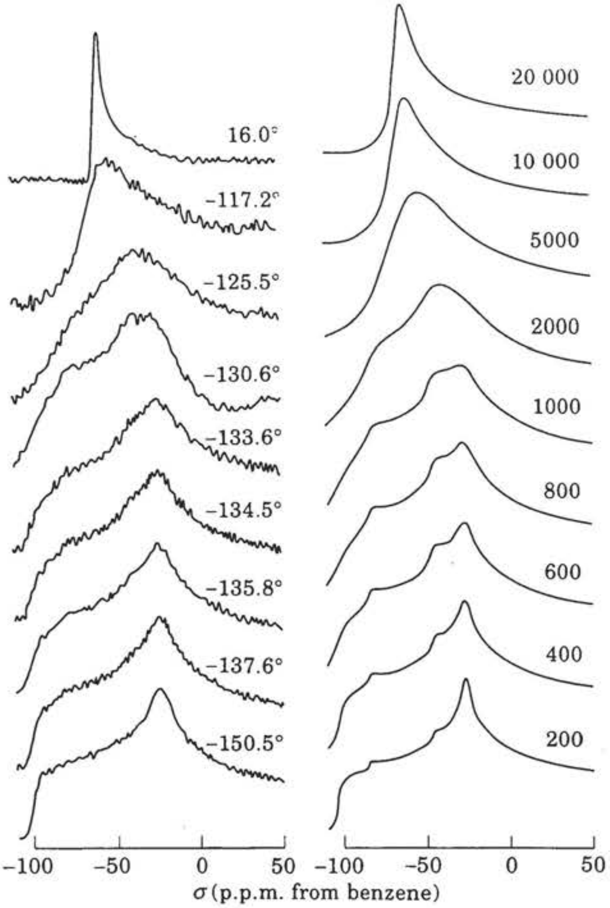

Fig. 5.6. – ^{13}C powder spectra of hexamethyl benzene showing the low-field part of the experimental and theoretical spectra for a number of temperatures. The right-hand side shows the theoretical spectra for a sixfold jump model, demonstrating the features due to motional narrowing present in the experimental spectrum (left). (Courtesy of D. E. WEMMER.)

Based on the principles of this exercise, it is possible to investigate the effects of symmetry in the case of more elaborate motional dynamics. For example, the motion of ethylene absorbed on a surface [133], and a particularly beautiful possibility being the reorientational motion of carbon-60 molecules under icosahedral symmetry [134, 135].

5˙6. *Macroscopic motional averaging.* – In this subsection we deal with symmetry considerations in motional averaging of anisotropic interactions. We recall that powder spectra of solids are broad because of the dependence of the frequency on orientation

$$\omega = \omega(\Theta, \phi).$$

In principle, by reorienting the sample rapidly and isotropically, simulating, for example, the reorientational motion of molecules in liquids, the anisotropy of the interactions could be made to vanish. Fortunately, it is not normally necessary to implement the full isotropic symmetry of the rotation group SO(3), since the anisotropic interaction has some symmetry, and the dependence of frequency on orientation can be represented as a *finite* sum of components, each irreducible under SO(3)

$$\omega = \sum_l \omega_l . \tag{5.14}$$

The contribution of each component ω_l depends on the $2l + 1$ values of the corresponding tensor A_{lm}, which forms the basis of the representation $D^{(l)}$ of SO(3), and on the orientation of the magnetic field in a sample-fixed coordinate system,

$$\omega_l = \sum_m A_{lm} D^{(l)}_{m0}(\Omega_{\text{sfc}}(t)) , \tag{5.15}$$

where $D^{(l)}_{m0}(\Omega_{\text{sfc}}(t))$ is an element of the associated Wigner rotation matrix. The question is what is the most economical (perhaps symmetric) set of orientations under which the $l \neq 0$ components of ω vanish.

5˙7. *Sample spinning.* – For a single l, for example $l = 2$, one simple answer involves rapid hopping or spinning about an axis. If the sample is undergoing some type of motion on a time scale comparable to the size of the interactions involved (typically a few kHz), then the orientation of the sample-fixed coordinate system will be time dependent and the observed phase of the signal for a given transition at some instant T is proportional to

$$\phi_l(T) = \int_0^T \mathrm{d}t\, \omega_l(t) = \sum_m A_{lm} \int_0^T \mathrm{d}t\, D^{(l)}_{m0}(\Omega_{\text{sfc}}(t)) . \tag{5.16}$$

As we saw in subsect. 2˙1 and 2˙3, stroboscopic sampling, followed by Fourier transform, gives the average frequency of the transition over the interval. The anisotropy described by tensor components $A_{lm\neq 0}$ for a particular l can be averaged away by reorienting the sample so that the field is directed at $N = l + 1$ or more directions to form a cone so that

$$\Omega^k_{\text{sfc}} \equiv \left(\alpha_k = \alpha_0 + \frac{2\pi}{N}k, \beta, \gamma\right) \tag{5.17}$$

because from eq. (5.16)

$$\sum_{k=1}^{N} D^{(l)}_{m0}(\Omega_{\text{sfc}}) = N d^{(l)}_{m0}(\beta)\,\delta_{m0}\,. \tag{5.18}$$

The remaining term, proportional to A_{l0}, can then be eliminated by a suitable choice of apex angle $2\beta^{(l)}$ such that

$$d^{(l)}_{00}(\beta^l) \equiv P_l(\cos\beta^{(l)}) = 0\,. \tag{5.19}$$

5'8. *Group theory of motional averaging.* – Now we pose the question of whether motional averaging under a subgroup G of SO(3) can average anisotropic terms in eq. (5.15). Such motion would represent an efficient means of effecting the averaging. We are concerned with the average value of each frequency component over all N symmetry operations R of the group G,

$$\overline{\omega}^G_l = \sum_m A_{lm}\overline{D^{(l)}_{m0}}, \tag{5.20}$$

where

$$\overline{D^{(l)}_{m0}} = \frac{1}{N}\sum_{R\in G} D^{(l)}_{m0}(\Omega_R)\,. \tag{5.21}$$

The representations of the group SO(3) reduce under the subgroup G as

$$D^{(l)}_{mn}(\Omega_R) = \sum_\lambda a^{(l,\lambda)} D^{(\lambda)}_{mn}(\Omega_R)\,, \tag{5.22}$$

where λ labels the irreducible representation of G. The average of the transformation matrices of eq. (5.21) and, therefore, *the average frequency* ω_l *can be different from zero only if* $D^{(l)}$ *contains the totally symmetric representation of* G [136]. The multiplicity $a^{(l,\lambda)}$ of A_1 when $D^{(l)}$ is reduced under G can be evaluated from

$$a^{(l,\lambda)} = \frac{1}{N}\sum_R \chi^{(l)}(R)\chi^{(\lambda)}(R)\,, \tag{5.23}$$

and the characters calculated from

$$\chi^{(l)}(R) = \sum_m D^{(l)}_{mm}(R) = \frac{\sin\left(l+\frac{1}{2}\right)\zeta_R}{\sin\frac{1}{2}\zeta_R}\,, \tag{5.24}$$

where ζ_R is an angle of rotation of the corresponding symmetry operation, related to Euler angles by

$$\zeta_R = 2\cos^{-1}\left\{\cos\frac{\beta_R}{2}\cos\frac{\alpha_R+\gamma_R}{2}\right\}. \tag{5.25}$$

TABLE II. – *Characters of the* $D^{(l)}$ *in the octahedral and icosahedral point subgroups of* SO(3).

Octahedral (O).

l	E	$8C_3$	$3C_4^2$	$6C_2$	$6C_4$	a^{A_1}
0	1	1	1	1	1	1
1	3	0	-1	-1	1	0
2	5	-1	1	1	-1	0
3	7	1	-1	-1	-1	0
4	9	0	1	1	1	1
5	11	-1	-1	-1	1	0
6	13	1	1	1	-1	1
7	15	0	-1	-1	-1	0
8	17	-1	1	1	1	1

Icosahedral (I), $\rho = (1+\sqrt{5})/2$, $\bar{\rho} = (1-\sqrt{5})/2$.

l	E	$12C_5$	$12C_5^2$	$20C_3$	$15C_2$	a^{A_1}
0	1	1	1	1	1	1
1	3	ρ	$\bar{\rho}$	0	-1	0
2	5	0	0	-1	1	0
3	7	$-\rho$	$-\bar{\rho}$	1	-1	0
4	9	-1	-1	0	1	0
5	11	1	1	-1	-1	0
6	13	ρ	$\bar{\rho}$	1	1	1
7	15	0	0	0	-1	0
8	17	$-\rho$	$-\bar{\rho}$	-1	1	0
9	19	-1	-1	1	-1	0
10	21	1	1	0	1	1

5·9. *Averaging under cubic and icosahedral symmetry.* – Table II shows the character tables for the octahedral (cubic) and icosahedral groups, with the last column indicating the multiplicity of the totally symmetric representation A_1 for the reduction of $D^{(l)}$ under G. A multiplicity of zero indicates that an anisotropic interaction of rank l will be averaged to zero under the symmetry of group G. For example, under the cubic group, second-rank interactions like chemical-shift anisotropy or first-order quadrupole coupling are averaged to zero. This symmetry may be implemented by reorienting the sample so that the magnetic field lies consecutively along the three orthogonal axes of the sample, a technique known as magic-angle hopping [137, 138]. Magic-angle spinning involves continually reorienting the sample in such a way that, in the sample frame, the magnetic field traces out a cone incorporating the three orthogonal

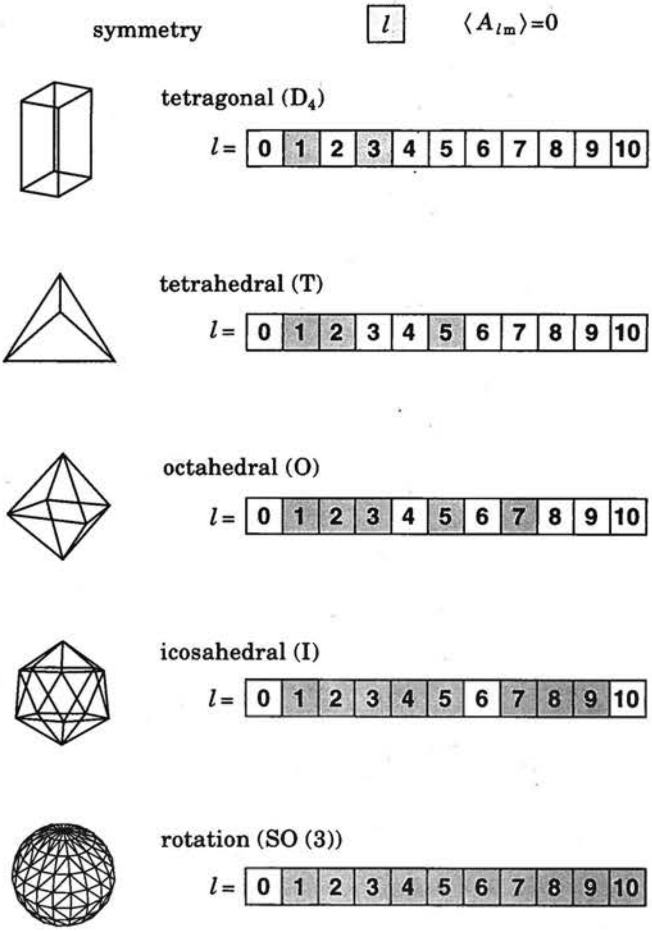

Fig. 5.7. – Averaging of spherical harmonics under subgroups of SO(3).

axes. Thus *magic-angle spinning can be regarded as a continuous implementation of cubic symmetry.*

The central transition for noninteger quadrupole spins is dominated by second-order quadrupole couplings which contain both $l = 2$ and $l = 4$ terms. These terms cannot vanish simultaneously by hopping or spinning about a single axis. However, the character table for the icosahedral group indicates that both these terms should vanish under icosahedral symmetry, which involves, in its most economical form, a motion of the sample amongst six orientations so that the magnetic field lies along the vertices of an icosahedron, a technique dubbed dynamic-angle hopping. A continuous version of this symmetry, dynamic-angle spinning, involves rotation of the sample about two axes so that the magnetic field traces out two cones incorporating the vertices of an icosahedron. *Icosahe-*

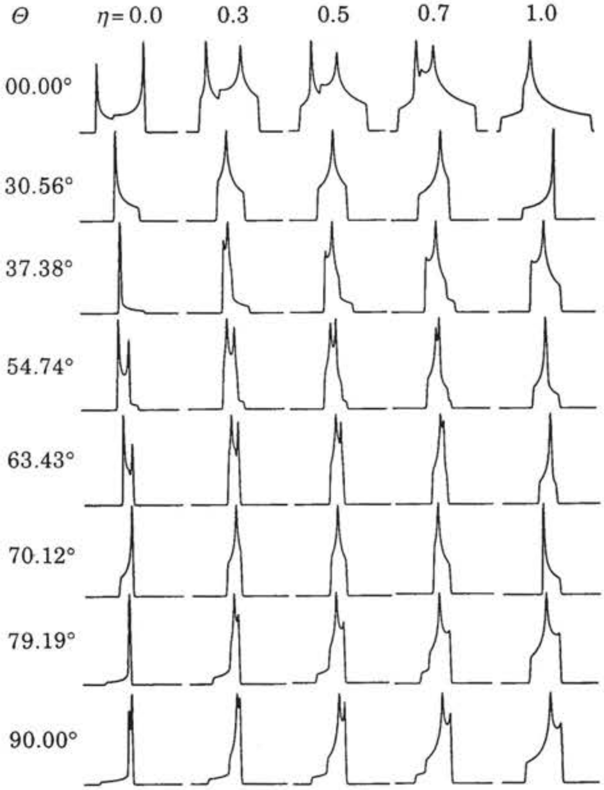

Fig. 5.8. – Simulated second-order powder patterns for the central transition of a spin $I = 3/2$ after motional averaging around a single rotation axis at various angles with respect to the magnetic field. 0° (icosahedral angle), 30.56° (root of $P_4(\cos\Theta)$), 37.38° (icosahedral angle), 54.74° (root of $P_2(\cos\Theta)$), 63.43° (icosahedral angle), 70.12° (root of $P_4(\cos\Theta)$), 79.19° (icosahedral angle). (Adapted from *Solid State Nucl. Magn. Reson.*, **1**, 267 (1992), with permission.)

dral symmetry can be viewed as the next approximation to the sphere for averaging of the higher-rank interactions. In fig. 5.7 we sum up which ranks are averaged to zero by a variety of symmetry groups including tetrahedral, octahedral and icosahedral. Note that the first ranks which are not averaged to zero by icosahedral motion are $l = 6$ and 10.

5·10. *Dynamic-angle spinning.* – An alternative view of dynamic-angle spinning is suggested by the powder patterns of fig. 5.8 for samples spinning around various axes [139]. Note that some of the lineshapes are in fact mirror images of others, with different scaling factors. For example, the spectra at 0° are scaled mirror images of those at 63.43°, and those spinning at 37.38° are exact images of those for 79.19°. Since reflection occurs about the isotropic-shift value for each crystal orientation, it is possible to rephase the signal of spins from all orientations simultaneously at some time by appropriate choice of spinning angles and evolution times. If evolution for a period τ_1 proceeds at the angle β_1, and subsequently for a period τ_2 at β_2, the accumulated anisotropic

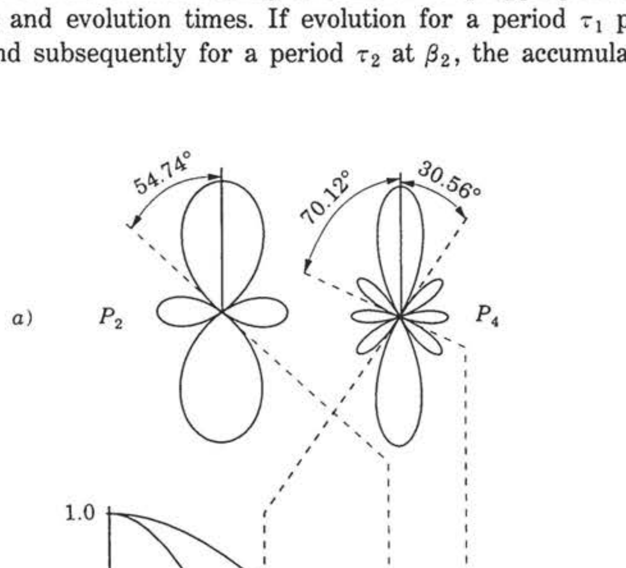

Fig. 5.9. – Plot of the second- and fourth-order Legendre polynomials, $P_2(\cos\Theta)$ and $P_4(\cos\Theta)$, *vs.* the angle of rotation in variable-angle spinning. *a)* Plot in polar coordinates, *b)* in Cartesian coordinates. The nodes of both functions are indicated by dashed lines. (Adapted from *Solid State Nucl. Magn. Reson.*, **1**, 267 (1992), with permission.)

phase will be

$$\phi(T) = \int_0^T \omega(\beta(t))\,\mathrm{d}t = \omega(\beta_1)\,\tau_1 + \omega(\beta_2)\,\tau_2\,. \tag{5.26}$$

The modulation in eq. (5.26) disappears for each interaction of rank n if

$$P_n(\cos\beta_1) + P_n(\cos\beta_2)\,k = 0\,, \tag{5.27}$$

where $k = \tau_2/\tau_1$ which results in $\phi(\tau_1 + \tau_2) = 0$. In this way the signal recorded

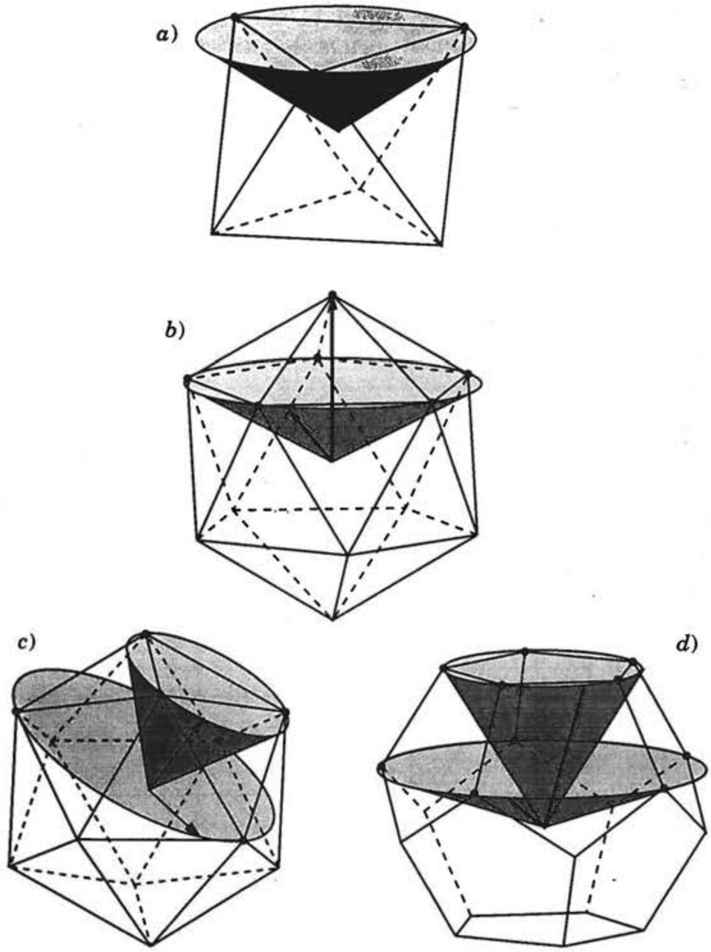

Fig. 5.10. – The external magnetic field viewed in a sample-fixed coordinate frame moves along one or two cones in MAS and DAS, respectively. The DAS trajectory on an icosahedron crosses six vertices for the $k = 5$ case (*b*)) and the $k = 1$ case (*c*)). The $k = 1$ case can also be seen as a trajectory crossing ten vertices of a dodecahedron (*d*)).

as a function of $\tau_1 + \tau_2$ with k constant will be independent of all anisotropic terms, and carry information only about the isotropic shifts.

Many variations of this approach are possible because motion of the spinning axis is not limited to discrete positions and equal probability. Dynamic-angle spinning trajectories have been implemented which follow the symmetry of regular polyhedra. The solutions of eq. (5.27) generally describe surfaces in the three-dimensional space of β_1, β_2 and $\tau_1 + \tau_2$. A simultaneous solution for two equations of the form of eq. (5.27) is obtained at any point on a crossing line of two surfaces, and these points are shown in fig. 5.9. Two solutions, ($\beta_1 = 37.38°$, $\beta_2 = 79.19°$, $k = 1$) and ($\beta_1 = 0.00°$, $\beta_2 = 63.43°$, $k = 5$), describe cones which traverse the vertices of an icosahedron (fig. 5.10), and thus correspond exactly to the icosahedral symmetry of subsect. 5˙9. Figure 5.11*a*) shows the pulse sequence for a typical DAS experiment and fig. 5.12 shows the resulting spectrum, in this case of the central transitions of the ^{17}O resonances in a series

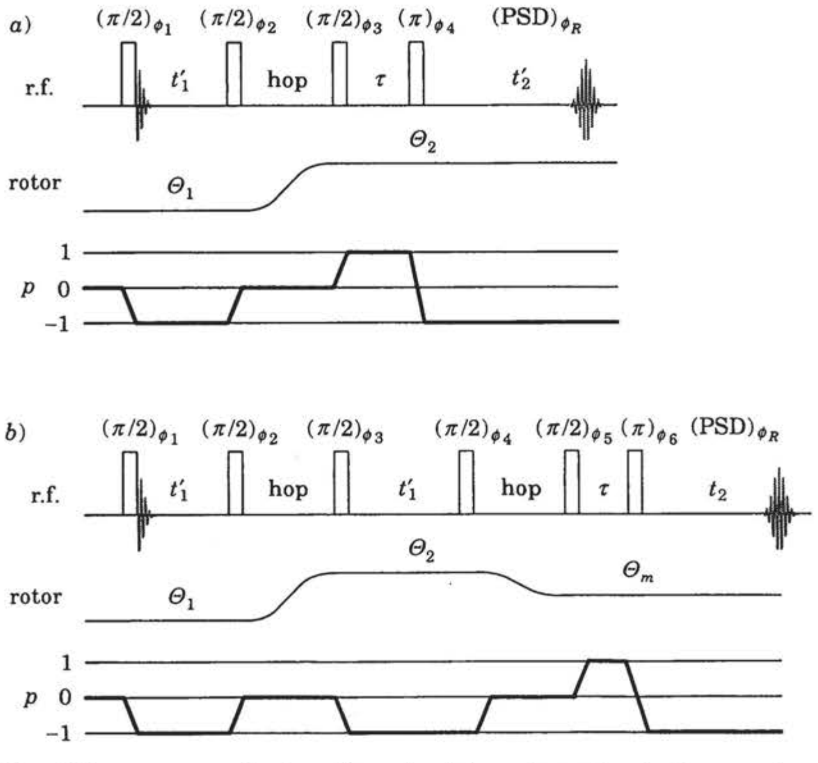

Fig. 5.11. – Pulse sequences for two-dimensional dynamic-angle spinning experiments. *a*) Conventional sequence to obtain an isotropic-anisotropic correlation, with powder patterns in the anisotropic dimension characteristic of the second spinning angle. *b*) Sequence including a second hop to allow detection at the magic angle. The phases are cycled so as to select the pathway illustrated below the sequence in order to ensure a pure phase spectrum by selecting the whole echo in t_2. (Courtesy of P. J. GRANDINETTI.)

of crystalline silicates. A simple extension of the sequence, shown in fig. 5.11*b*), includes an extra hop after t_1 which allows detection of the signal in t_2 at the magic angle. This facilitates analysis of the spectrum since the powder patterns in the anisotropic dimension of the spectrum are free of second-rank contributions and are only due to the second-order quadrupole (fourth-rank) contributions, illustrated for the central transitions of ^{87}Rb in rubidium nitrate in fig. 5.13 [140].

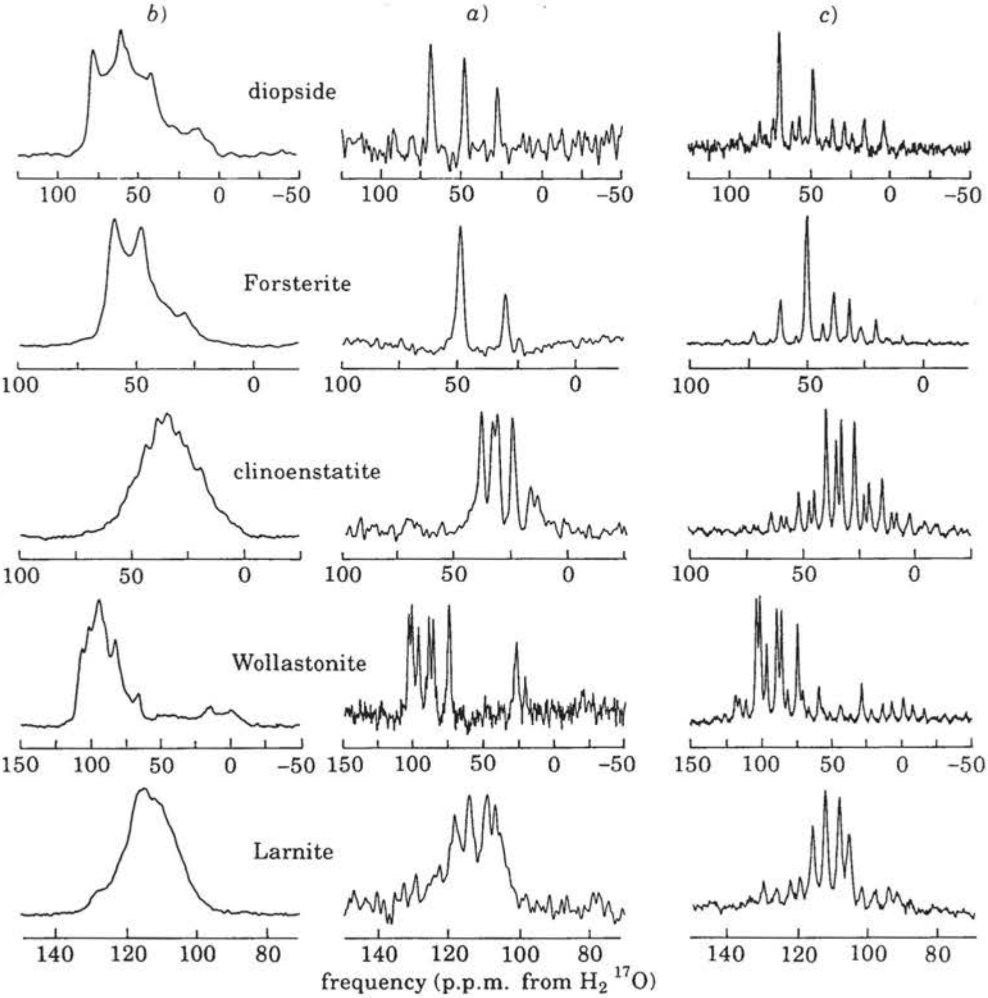

Fig. 5.12. – *a*) Isotropic ^{17}O dynamic-angle spinning spectra of a series of crystalline silicates at 9.4 T. For comparison we also show *b*) the magic-angle spinning spectra and *c*) the double-rotation spectra of the same compounds. (Courtesy of K. T. MUELLER.)

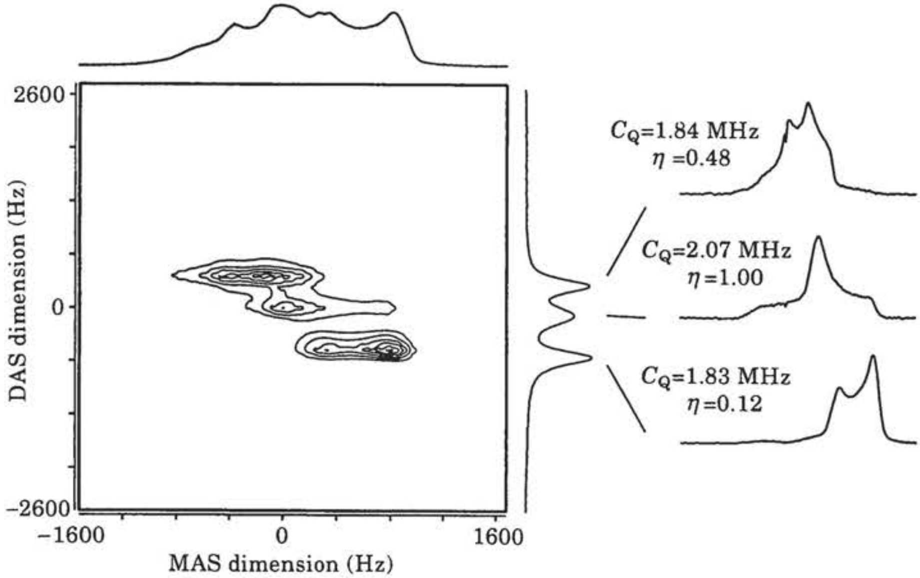

Fig. 5.13. – The two-dimensional dynamic-angle spinning spectrum of the central transition of ^{87}Rb in $RbNO_3$ obtained using the sequence of fig. 5.11*b*). The isotropic-anisotropic correlation yields powder patterns that are determined purely by fourth-rank interactions, which facilitates the analysis in terms of the quadrupolar coupling constants and asymmetry parameters (Adapted from *J. Am. Chem. Soc.*, **114**, 7489 (1992), with permission).

5·11. *Isotropic-anisotropic correlation spectra.* – Note that because the isotropic spectrum is detected indirectly in a DAS experiment, according to the pulse sequences shown in fig. 5.11, two-dimensional Fourier transform of the data (followed by a shearing transform) yields a two-dimensional isotropic-anisotropic correlation spectrum. Thus the isotropic resolution is achieved without sacrificing the information contained in the anisotropies, and for each isotropic line we can obtain the corresponding anisotropy [72, 141, 142] which may allow us to assign the isotropic shifts, or in favorable cases gives access to a wealth of chemical information about the material under study. Such a case is shown in fig. 5.14 in which we show the DAS spectrum of a potassium tetrasilicate glass ($K_2Si_4O_9$) [143]. At first sight the broad line in the isotropic dimension may appear to indicate that the experiment has failed to remove completely the anisotropy. However, closer inspection reveals that this broadening is due to a distribution of isotropic sites in the glass and, moreover, when we examine the anisotropies, we see that they are dependent on the isotropic shift (fig. 5.10). FARNAN *et al.* [143] have shown that this distribution of quadrupolar couplings and asymmetry parameters can be converted into a bond angle distribution for the glass shown in fig. 5.15, thus clearly demonstrating the enormous potential such experiments have for structural studies of complex materials [144].

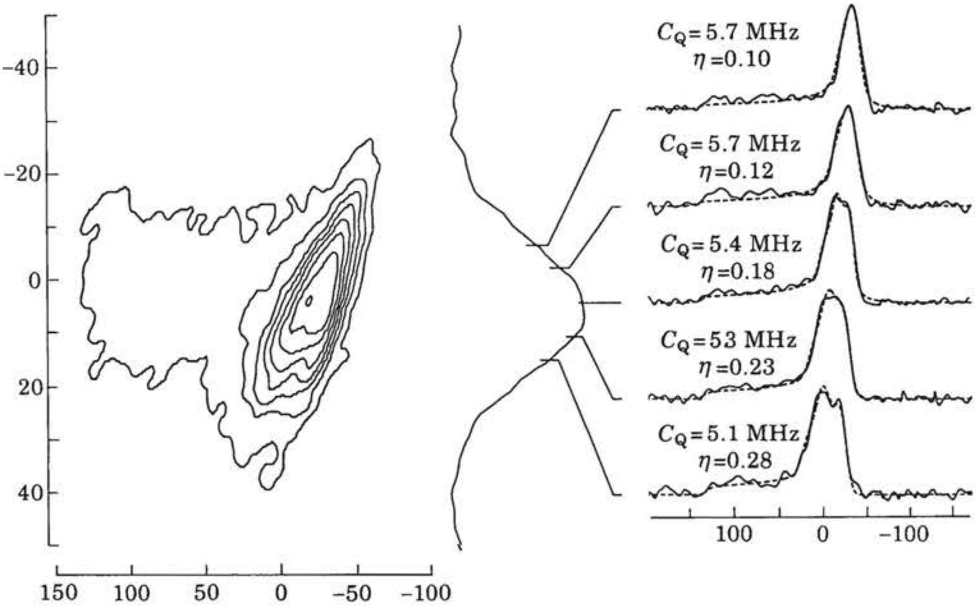

Fig. 5.14. – Two-dimensional ^{17}O DAS NMR spectrum of $K_2Si_4O_9$ glass, showing the resonance of the bridging oxygens. The anisotropic lineshapes are characteristic of spinning at 79.19° with respect to the field, and are due almost entirely to the interaction between the quadrupole moment of ^{17}O and the electric-field gradient at the oxygen sites. Slices through the anisotropic dimension are subjected to multiparameter fits to determine the magnitude and asymmetry of the field gradient across the isotropic line. (Adapted from *Nature (London)*, 358, 31 (1992), with permission.)

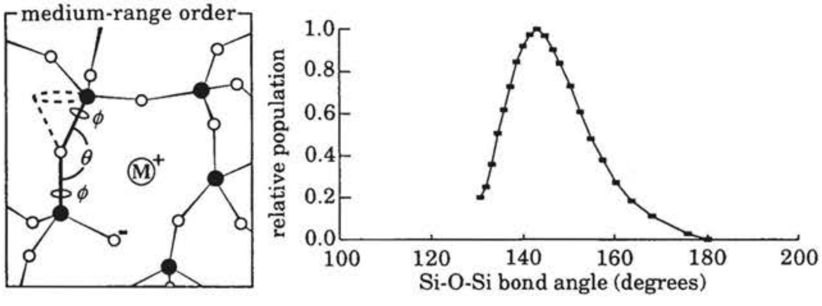

Fig. 5.15. – The quadrupolar-coupling constants and asymmetry parameters extracted from fig. 5.14 can be used to determine the distribution of Si-O-Si bond angles in the $K_2Si_4O_9$ glass which characterizes the degree of medium-range order present in the structure. (Adapted from *Nature (London)*, 358, 31 (1992), with permission.)

5·12. *Variable-angle correlation spectroscopy.* – An alternative approach to isotropic-anisotropic correlations in MAS spectroscopy is given by variable-angle correlation spectroscopy (VACSY) [145]. This experiment is representative of a broad spectrum of potential new techniques, dubbed mixed dimension acquisition schemes (MIDAS), for obtaining many kinds of correlation spectra, and it is instructive to look at it in more detail.

From the description of subsect. 5·11 it might seem that either a change in the rotor axis or the application of synchronous pulses is necessary in order to correlate an isotropic (*i.e.* magic-angle spinning) spectrum with a static (*i.e.* spinning at 0°) spectrum. However, we have already seen that continuous versions of the hopping experiments (the transition from magic-angle hopping to magic-angle spinning) yield similar results. Indeed, the VACSY experiment yields two-dimensional isotropic-anisotropic correlation spectra for spin $I = 1/2$ systems experiencing anisotropic chemical shift or heteronuclear dipolar interactions without changing the spinning axis during the sequence. In subsect. 2·2 we derived the chemical-shift Hamiltonian for a spin $I = 1/2$ system undergoing rapid spinning at an angle Θ with respect to the field. Equation (2.20) can be used to derive the precession frequency for a given crystallite orientation in the form

$$\omega(\alpha, \beta, \gamma) = \omega_i + P_2(\cos\Theta)\,\omega_a(\alpha, \beta, \gamma), \tag{5.28}$$

where the anisotropy is scaled by the second-order Legendre polynomial. Con-

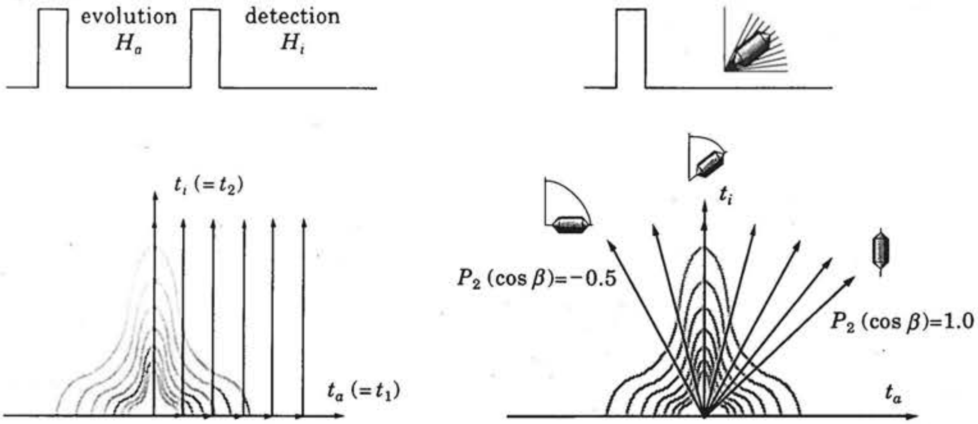

Fig. 5.16. – In «traditional» correlation spectroscopy (left) the time domain is sampled in Cartesian-coordinate fashion by arranging for pure anisotropic and pure isotropic evolution respectively during t_1 and t_2 (perhaps by changing the spinning axis from 0° during t_1 to Θ_m during t_2). In variable-angle correlation spectroscopy (VACSY) (right), the same correlation spectrum is obtained through a non-Cartesian sampling from a series of variable-angle spinning experiments, which progressively scale the anisotropic contribution to the evolution. (Adapted from *J. Chem. Phys.*, **97**, 4800 (1992), with permission.)

sider now the time domain acquisition in a conventional two-dimensional correlation experiment in which the data are sampled in Cartesian coordinates under the pure interactions that are desired in the corresponding dimensions, as illustrated in fig. 5.16. In such an experiment the signal is given by

$$f(t_1, t_2) = \int\int I(\omega_1, \omega_2) \exp[i(\omega_1 t_1 + \omega_2 t_2)]\, \mathrm{d}\omega_1\, \mathrm{d}\omega_2 \,. \tag{5.29}$$

Let us compare eq. (5.29) to the signal acquired in a one-dimensional spinning experiment corresponding to eq. (5.28), for which

$$f(t) = \int I(\omega(\alpha, \beta, \gamma)) \exp[i\omega t]\, \mathrm{d}\omega \,, \tag{5.30}$$

and, if we substitute eq. (5.28) in (5.30), we obtain an expression of the form

$$f(t_i, t_a) = \int\int I(\omega_i, \omega_a) \exp[i(\omega_i t_i + \omega_a t_a)]\, \mathrm{d}\omega_i\, \mathrm{d}\omega_a \tag{5.31}$$

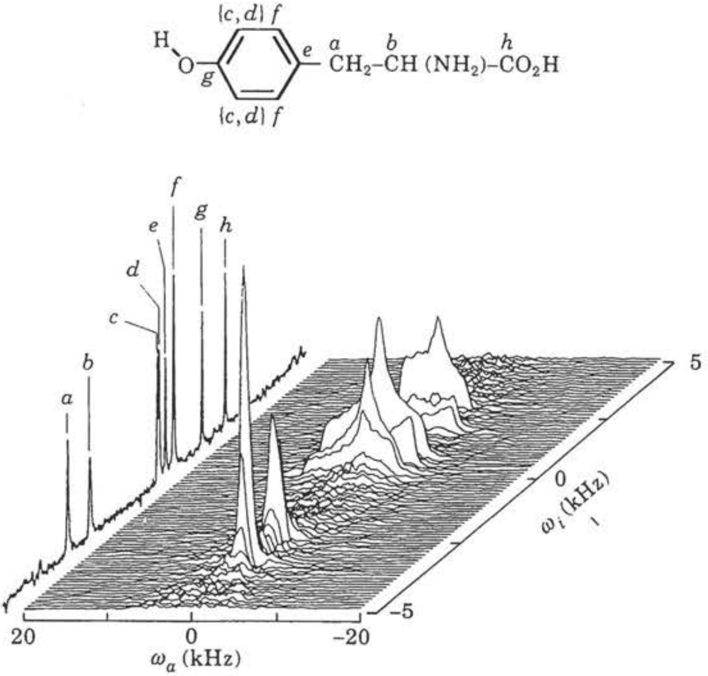

Fig. 5.17. – Two-dimensional isotropic-anisotropic NMR chemical-shift correlation spectrum of L-tyrosine, showing the isotropic projection and the assignment of the peaks to each site in the molecule. A set of 65 signals were digitized at rates of 12 kHz over a range of angles. Experimental data were then interpolated over a regular grid composed of 128 × 256 points and Fourier transformed. (Adapted from *Isr. J. Chem.*, 32, 161 (1992), with permission.)

with $t_i = t$ and $t_a = P_2(\cos\Theta)\,t$. This expression has the same form as eq. (5.29) for a normal two-dimensional spectrum and suggests that *by acquiring a series of spectra spinning at different angles we should be able to obtain an isotropic-anisotropic correlation spectrum.* Indeed, by recording such a series of spectra and rearranging the data as shown in fig. 5.16, the spectrum of solid tyrosine, shown in fig. 5.17, was obtained. The great advantage of this technique is that it allows one to obtain spectra by scaling interactions, thus avoiding experiments in which one must switch interactions either by sudden mechanical motion of the sample or the introduction of multiple-pulse irradiation. This analysis turns out to be very general (analogous to imaging by projections instead of Fourier imaging) and it is possible to obtain not only two-dimensional correlations in this way, but also higher-dimensional spectra, the only prerequisite being that the original anisotropic nD spectrum has a form in which the anisotropic contributions scale with $P_2(\cos\Theta)$. The technique has already been extended to the separation of anisotropic two-dimensional exchange spectra [121] according to their isotropic shifts [146].

6. – Cross-polarization.

6·1. *Spin temperature.* – This section is concerned with cross-polarization, and especially the equilibrium magnetizations observed in cross-polarization (CP) experiments. Using simple models of cross-polarization [147, 148] we may predict the equilibrium magnetizations by observing that in a system containing N_S S spins and N_I I spins, experiencing fields B_I and B_S, the initial I spin magnetization is given by Curie's law

$$M_I^0 = \beta_I^0 C_I B_I \,, \tag{6.1}$$

where

$$\beta_I^0 = 1/kT \tag{6.2}$$

is the inverse spin temperature, and

$$C_I = \gamma_I^2 hI(I+1) N_I/3 \tag{6.3}$$

is the I spin heat capacity. Two of the most important quantities of the system are the energy

$$E_I^0 = -\beta_I^0 C_I B_I^2 \,, \tag{6.4}$$

and the entropy

$$S_I = \text{const} - k(\beta_I^0)^2 C_I B_I^2 \,. \tag{6.5}$$

If the spins are allowed to come into thermal contact so that they exchange magnetization at a rate characterized by T_{IS}, then after a time $t \gg T_{IS}$ the I and

S spins will come to equilibrium and will have equal spin temperatures

$$\beta^{\text{eq}} = \beta_I^{\text{eq}} = \beta_S^{\text{eq}}, \tag{6.6}$$

in which case the energy is now

$$E^{\text{eq}} = E_I^{\text{eq}} + E_S^{\text{eq}} = -\beta^{\text{eq}}(C_I B_I^2 + C_S B_S^2). \tag{6.7}$$

Since the Hamiltonian is assumed to be time independent, energy is conserved. By defining $\varepsilon^2 = C_S/C_I$ and $\chi = B_S/B_I$ we obtain

$$\beta^{\text{eq}} = \beta^0 \frac{1}{1+\chi^2\varepsilon^2} \tag{6.8}$$

and we can predict the S spin equilibrium magnetization

$$M_S^{\text{eq}} = \frac{\alpha}{1+\chi^2\varepsilon^2}\beta_I^0 C_S B_I = \frac{\chi}{1+\chi^2\varepsilon^2} M_S^0, \tag{6.9}$$

where M_S^0 is the normal value of M_S at thermal equilibrium.

6·2. *Methods for obtaining thermal contact.* – In the normal laboratory frame T_{IS} is comparable to the rate of equilibration with the lattice. In order to achieve rapid cross-polarization we must isolate the I and S spins from the lattice and put them in thermal contact. We discuss two popular methods.

i) *Hartmann-Hahn matching.* The Hartmann-Hahn experiment [149] is a rotating-frame experiment, shown in fig. 6.1, in which the B fields correspond to applied magnetic fields in the transverse plane. T_{IS} is found to be strongly dependent on B_I and B_S and, therefore, on χ. The most rapid cross-polarization occurs under the Hartmann-Hahn (HH) condition

$$\gamma_I B_I = \gamma_S B_S. \tag{6.10}$$

In this case polarization can be transferred by energy-conserving mutual spin flip-flops as shown in fig. 6.1 [150]. Normally $N_S \ll N_I$ so that $\varepsilon \ll 1$, in which case eq. (6.9) becomes

$$M_S^{\text{eq}} = \frac{\gamma_I}{\gamma_S} M_S^0 \tag{6.11}$$

and the HH enhancement is given by the ratio γ_I/γ_S which is 4 for ^{1}H and ^{13}C. We will consider in detail problems associated with HH mismatch ($\chi \neq 1$) below.

ii) *Adiabatic demagnetization in the rotating frame* (ADRF) [147, 151]. A second method for obtaining efficient cross-polarization is shown in fig. 6.2. In this experiment (also performed in the rotating frame) transverse I spin magnetization is first spin locked and then the field B_I is adiabatically allowed to decrease to zero. If we take the most simple example of a two-spin system IS,

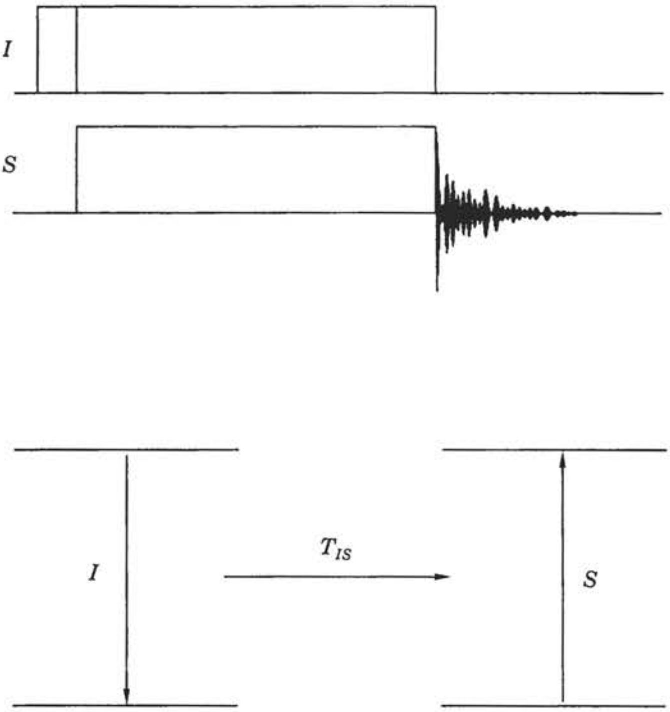

Fig. 6.1. – Pulse sequence for Hartmann-Hahn cross-polarization, in this case with detection of the S-spin free-induction decay. If the magnetic fields B_I and B_S in the rotating frames fulfill the condition of eq. (6.10), then an energy-conserving I-S flip-flop can occur resulting in a transfer of polarization as illustrated schematically in the lower part of the figure. (Adapted from *J. Chem. Phys.*, **59**, 569 (1973), with permission.)

then the initial density matrix in the tilted frame is

$$\rho(0) = I_z \tag{6.12}$$

and the Hamiltonian

$$H(t) = \omega_{1I}(t)\, I_z + b2I_x S_x\,, \tag{6.13}$$

where b is the heteronuclear dipolar interaction. If we assume that $\omega_{1I} \gg b$ at the beginning of the experiment, then we obtain

$$H_0 \approx \omega_{1I}(0)\, I_z \tag{6.14}$$

and we observe that $[H_0, \rho(0)] = 0$. If we turn the field off adiabatically, this corresponds to the condition

$$[H(t), \rho(t)] = 0 \tag{6.15}$$

for all values of t. Thus, when the field reaches zero, we obtain a Hamiltonian

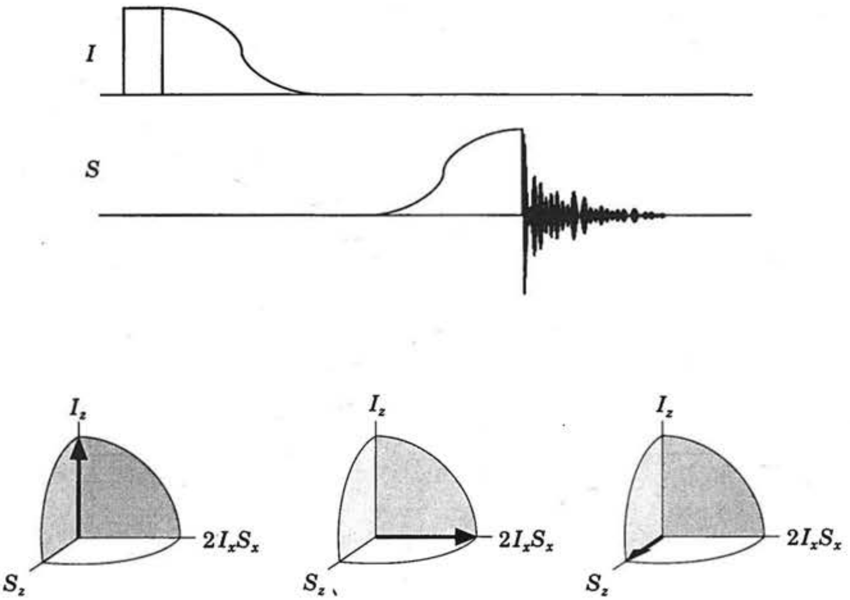

Fig. 6.2. – Pulse sequence for adiabatic demagnetization in the rotating frame. The evolution of the density matrix in a two-spin system is illustrated below. At the start of the experiment (lower left) all the spin order is contained in I_z. After adiabatic demagnetization the order is transferred into the dipolar reservoir, which is in turn transferred to S-spin order after remagnetization at the S-spin frequency (lower right).

and a density operator

$$H(t) = b2I_xS_x\,, \qquad \rho(t) = 2I_xS_x\,. \tag{6.16}$$

Since the change in the density matrix was adiabatic, all the spin order in this two-spin system is transferred from the reservoir I_z into the dipolar reservoir. It can be seen that, if we now adiabatically turn on a strong S spin field, all the order in the dipolar reservoir is transferred to the S spin longitudinal reservoir, so that we can achieve (in the two-spin system) complete transfer of polarization from I to S. The principles of this experiment are illustrated graphically in fig. 6.2. (Note that, if there are two I spins, complete transfer is no longer possible, a point we shall return to in sect. 7.)

6˙3. *Statistical picture of cross-polarization.* – An alternative way of looking at CP is to consider the details of the microscopic behavior of the spins [23]. If we consider a system of N_I I spins with N_{I^+} «up» and N_{I^-} «down» coupled to N_S S spins with N_{S^+} «up» and N_{S^-} «down», the I and S polarizations are defined by

$$\begin{cases} P_I = N_{I^+} - N_{I^-}\,, \\ P_S = N_{S^+} - N_{S^-}\,. \end{cases} \tag{6.17}$$

Initially $P_S = 0$ and $P_I = P_I^0$. We will consider briefly a question to which we shall return in the next section: what is the maximum S polarization achievable by the most efficient possible CP process from I to S? Our first consideration is that for maximum efficiency we must conserve entropy (so that the polarization transfer corresponds to a reversible process). The entropy depends on the number of configurations that the system can occupy,

$$S = k \ln W, \tag{6.18}$$

in which W represents the number of ways to place N^+ indistinguishable objects in N positions,

$$W = \binom{N}{N^+} = \frac{N!}{N^+!N^-!}. \tag{6.19}$$

If N is large, we obtain

$$W \approx 2^N \exp\left[\frac{-P^2}{2N}\right], \tag{6.20}$$

so that the entropy is

$$S = \text{const} - \frac{P^2}{2N}. \tag{6.21}$$

If we consider a situation in which entropy is conserved and all the I polarization is transferred to S, then we can equate S^0 with S^{eq} and obtain

$$\frac{(P_I^0)^2}{2N_I} = \frac{(P_S^{\text{eq}})^2}{2N_S}. \tag{6.22}$$

By simple rearrangement we see that the maximum final S polarization is

$$P_S^{\max} = P_S^{\text{eq}} = \sqrt{\frac{N_S}{N_I}}\, P_I^0. \tag{6.23}$$

Now we recall that the equilibrium polarization is proportional to γ and N, so that

$$P_I^0 = \frac{\gamma_I}{\gamma_S}\frac{N_I}{N_S} P_S^0. \tag{6.24}$$

Inserting eq. (6.24) in eq. (6.23)

$$P_S^{\max} = \frac{\gamma_I}{\gamma_S}\sqrt{\frac{N_I}{N_S}}\, P_S^0, \tag{6.25}$$

or for the magnetization

$$M_S^{\max} = \frac{\gamma_I}{\gamma_S}\sqrt{\frac{N_I}{N_S}}\, M_S^0. \tag{6.26}$$

Note that the S magnetization predicted here is a factor $\sqrt{N_I/N_S}$ larger than with HH matching given in eq. (6.11).

6·4. *Hartmann-Hahn mismatch.* – Returning to Hartmann-Hahn experiments (which will form the basis of the rest of the section), we would like to consider in detail the behavior of the system for $\chi \neq 1$. (Similar considerations apply to certain incarnations of the ADRF experiment.) Using eq. (6.10) we can predict the dependence of M_S^{eq} on the parameter $\chi = B_S/B_I$ as is shown in fig. 6.3. Although the treatment of subsect. **6·1** predicts maximum S magnetization for $\omega_S > \omega_I$, experimentally the maximum value of M_S^{eq} is observed at HH match. In order to explain the off-match behavior, we must develop an extension to the standard view of spin temperature and thermodynamics which will allow us to predict more accurately the equilibrium positions. Following LEVITT *et al.* [152, 153] we describe the system by an initial density operator $\rho(0)$ which is subjected to a time-independent Hamiltonian H which acts like a unitary transformation on the density operator

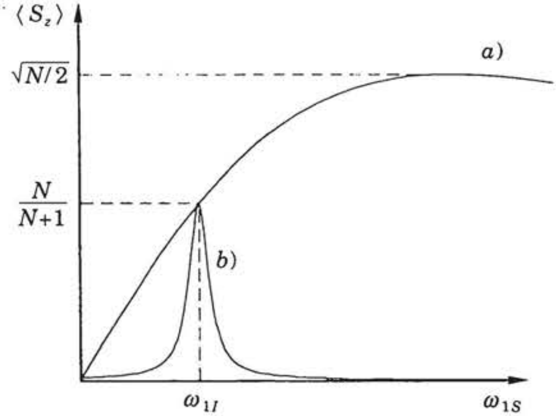

Fig. 6.3. – S-spin magnetization as a function of S-spin r.f. field. The model of subsect. **6·1** predicts curve a), whilst experimental dependences are obtained which follow curve b) and have a peak at HH match. (Adapted from ref. [152], with permission.)

$$\rho(t) = U\rho(0)\,U^{-1}\,, \tag{6.27}$$

where $U = \exp[-iHt]$. From spin thermodynamics we expect that on some time scale $t \gg T_{IS}$ the important observables of the system, such as the magnetizations of the different spins, eventually become time-independent, which is found to be valid in all sufficiently large and complex systems.

In the case of strong r.f. fields (applied along the x-axis) it is most convenient to transform to a picture defined by a rotation about the y-axis

$$A' = R^{-1}AR\,,$$

with

$$R = \exp\left[-i\frac{\pi}{2}\left(\sum_k I_{ky} + S_y\right)\right]. \tag{6.28}$$

At HH match we partition the Hamiltonian into two (noncommuting) reservoirs of spin order,

$$\Omega_1 = \frac{1}{\sqrt{N}}\sum_1^N I_{iz}\,, \tag{6.29}$$

$$\Omega_2 = S_z\,, \tag{6.30}$$

and

$$h_1 = \sqrt{N}\,\omega_{1I}\,, \qquad h_2 = \omega_{1S}\,, \tag{6.31}$$

and a perturbation term corresponding to the dipolar interactions,

$$V = \sum_1^N b_i 2I_{ix}S_x + H_{II}\,, \tag{6.32}$$

in which b_i are the heteronuclear dipolar interactions and H_{II} is the I-I interaction Hamiltonian. The equilibrium position is determined by projection of the initial density operator onto the reservoir terms

$$\rho^0_{\mathrm{eq}} = \frac{\langle H^0|\rho(0)\rangle}{\langle H^0|H^0\rangle}H^0\,, \tag{6.33}$$

where

$$H^0 = h_1\Omega_1 + h_2\Omega_2\,. \tag{6.34}$$

This has a simple geometric interpretation, demonstrated in fig. 6.4. The total energy of the system,

$$\langle H\rangle = \langle H|\rho\rangle = \langle H^0|\rho^0\rangle + \langle V|\rho^0\rangle + \langle H|\rho'(t)\rangle\,, \tag{6.35}$$

is conserved since the Hamiltonian is time-independent. Since the excess term ρ' is taken to be orthogonal to H^0, and the energetic influence of the perturbation V is ignored, the energy is contained only in the reservoirs

$$\langle H\rangle = \langle H^0|\rho^0\rangle.$$

The reservoir energy is the component of the state vector parallel to the reservoir Hamiltonian, as illustrated in fig. 6.4.

On the contrary, the entropy is split between the reservoirs and the excess term, and in the high-temperature approximation the entropy $S = \rho \ln \rho$ is proportional to the spin order. The spin order is simply

$$\langle\rho|\rho\rangle = \langle\rho^0|\rho^0\rangle + \langle\rho'|\rho'\rangle. \tag{6.36}$$

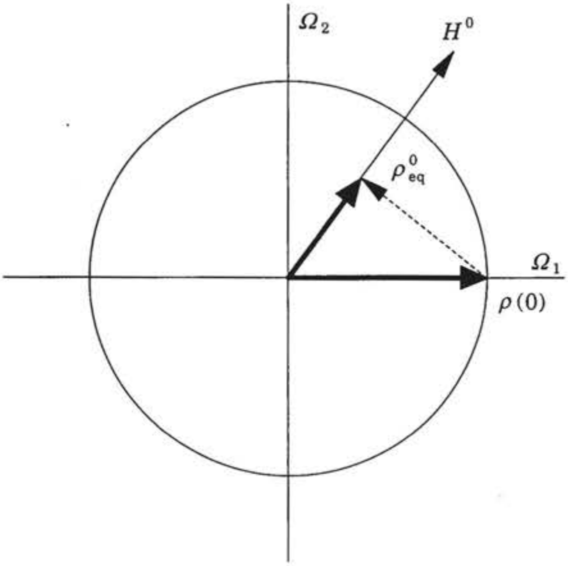

Fig. 6.4. – Geometric picture of equilibrium. In the plane of the reservoir operators the reservoir Hamiltonian is described by a vector. Equilibrium is represented as the projection of the initial density operator $\rho(0)$ onto the Hamiltonian. The circle represents the limit imposed by conservation of spin order.

Since the transformation from ρ^0 to ρ^0_{eq} is unitary, the *total* entropy must be conserved. The excess term ρ' serves as a repository of entropy but not energy.

The partition of eqs. (6.29)-(6.32) results in the predictions of CP efficiency *vs.* mismatch shown in fig. 6.3. Whilst it may be tempting to attribute this discrepancy between experiment and theory to a dynamic effect, experiments show that even far from match constant values of the S magnetization are obtained fairly quickly, after initial oscillations have decayed (see fig. 6.5) [153].

6'5. *Thermodynamics of heteronuclear cross-polarization.* – To achieve a description which works off match we must include the effect of broadening of the distribution of I-spin energy levels by dipolar interactions so as to produce a finite width of the HH match. However, we cannot simply replace Ω_1 by $\Omega_1 + H_{II}$ since, although the choice of «reservoirs» and «perturbations» is made arbitrarily, nevertheless each term should either have a harmonic spectrum, or a dense spectrum with a large number of closely spaced eigenvalues. The energy level structure resulting from replacement of Ω_1 by $\Omega_1 + H_{II}$ does not fulfill either of these guidelines. Indeed a combined Zeeman-dipolar reservoir does not attain internal thermal equilibrium rapidly if the applied fields are strong. Thus we are faced with the problem of how to include the energetic effects of H_{II}.

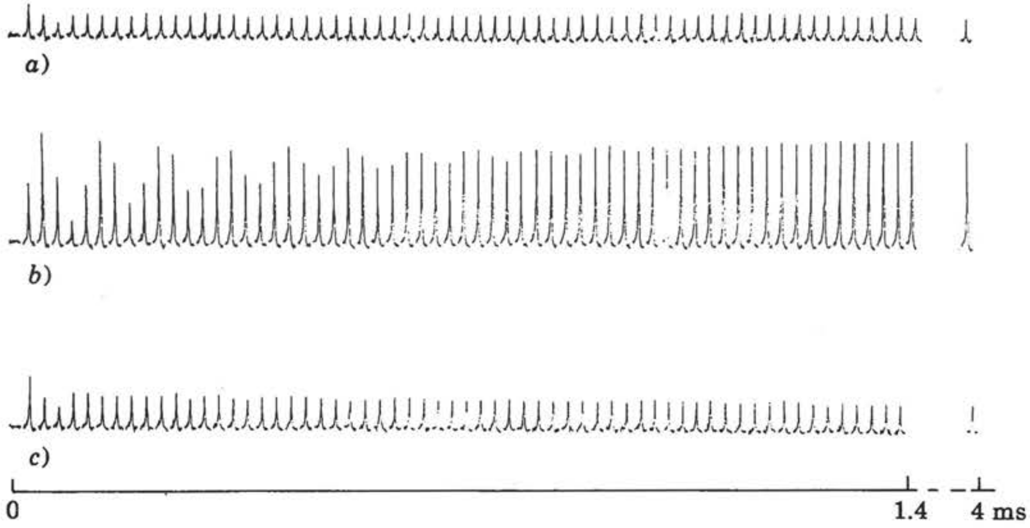

Fig. 6.5. – Experimental evolution of ^{13}C magnetization as a function of cross-polarization time for a single crystal of ferrocene. The experiments were performed at three different r.f. fields where *a*) has an *S*-spin field below the Hartmann-Hahn matching condition, *b*) corresponds to match, and *c*) is above match. Even away from the Hartmann-Hahn condition an equilibrium state is achieved fairly quickly, and we see that the theoretical behavior predicted by the standard model is not borne out in practice. (Adapted from *J. Chem. Phys.*, 84, 4243 (1986), with permission.)

The solution is based on the identification of quasi-invariants of the system, operators whose expectation values may be assumed to be conserved during the process of thermal equilibration. In the case of heteronuclear cross-polarization we make the following division into *three* relevant reservoirs: the first two are simply Ω_1 and Ω_2 of eqs. (6.29)-(6.31), and we invoke Ω_3 where

$$h_3\Omega_3 = -\frac{1}{2}\sum_{jk} d_{jk}\left(2I_{jz}I_{kz} - \frac{1}{2}(I_j^+ I_k^- + I_j^- I_k^+)\right) \tag{6.37}$$

(neglecting nonsecular terms), and the perturbation is the heteronuclear coupling term

$$V = \sum_1^N b_i 2I_{1x}S_x . \tag{6.38}$$

If this partition is valid (see subsect. 6˙9), we may proceed to observe that, since the operator $\sum_k I_{kz} + S_z$ commutes with all the major terms in the Hamiltonian (*i.e.* I^+S^-, I^-S^+), it is plausible to associate a *quasi-invariant operator* Q_1 with it. The expectation value $\left\langle \sum_k I_{kz} + S_z \right\rangle$ then represents the total number of spins with magnetic quantum number $+1/2$ minus the number with $-1/2$, the total angular momentum of the sample, which is clearly conserved by spin pair flips. Thus

$$Q_1 = q_1\left(\sum_1^N I_{kz} + S_z\right) \tag{6.39}$$

with the normalization

$$q_1 = \frac{\left\langle H^0 \,\middle|\, \sum_1^N I_{kz} + S_z \right\rangle}{\left\langle \sum_1^N I_{kz} + S_z \,\middle|\, \sum_1^N I_{kz} + S_z \right\rangle} = \frac{N\omega_{1I} + \omega_{1S}}{N+1} . \tag{6.40}$$

Assuming that there are only two quasi-invariants of the system, then the second quasi-invariant Q_2 can be obtained:

$$Q_2 = H^0 - Q_1 , \tag{6.41}$$

where Q_2 may be calculated to be

$$Q_2 = \frac{\Delta\omega}{N+1}\left\{NS_z - \sum_1^N I_{kz}\right\} + h_3\Omega_3 \tag{6.42}$$

and where $\Delta\omega = \omega_{1S} - \omega_{1I}$.

Note that Q_1 has distinct harmonic eigenvalues, while, for mismatch $\Delta\omega \approx \approx d_{jk}$, Q_2 has a quasi-continuous spectrum. Assuming $N \gg 1$, the quasi-equilibrium density operator is

$$\rho(t_{\mathrm{qe}}) \approx \frac{\langle\rho(0)|Q_1\rangle}{\langle Q_1|Q_1\rangle} Q_1 + \frac{\langle\rho(0)|Q_2\rangle}{\langle Q_2|Q_2\rangle} Q_2 , \tag{6.43}$$

$$\rho(t_{\mathrm{qe}}) = \alpha_{0I}\left\{S_z \frac{\lambda^2}{\lambda^2 + \Delta\omega^2} + \sum_1^N I_{kz} + h_3\Omega_3 \frac{-\Delta\omega}{\lambda^2 + \Delta\omega^2}\right\}, \tag{6.44}$$

with the CP width λ given by

$$\lambda^2 = \frac{\langle h_3\Omega_3 | h_3\Omega_3\rangle}{\langle I_{kz}|I_{kz}\rangle} = \frac{1}{4} N M_2^I , \tag{6.45}$$

where M_2^I is the second moment of the I-spin resonance line. This process represents a maximization of entropy under the constraints that all $\langle Q_q\rangle$ remain constant. It can be visualized as partial thermal equilibration between the reservoirs H_j^0 which cannot proceed to completion because of the constraint that the invariants $\langle Q_q\rangle$ are conserved, and may be viewed graphically as shown in fig. 6.6.

Equation (6.44) predicts the achievable S-spin polarization is maximum on match, and falls off on either side of match as a Lorentzian function of half-

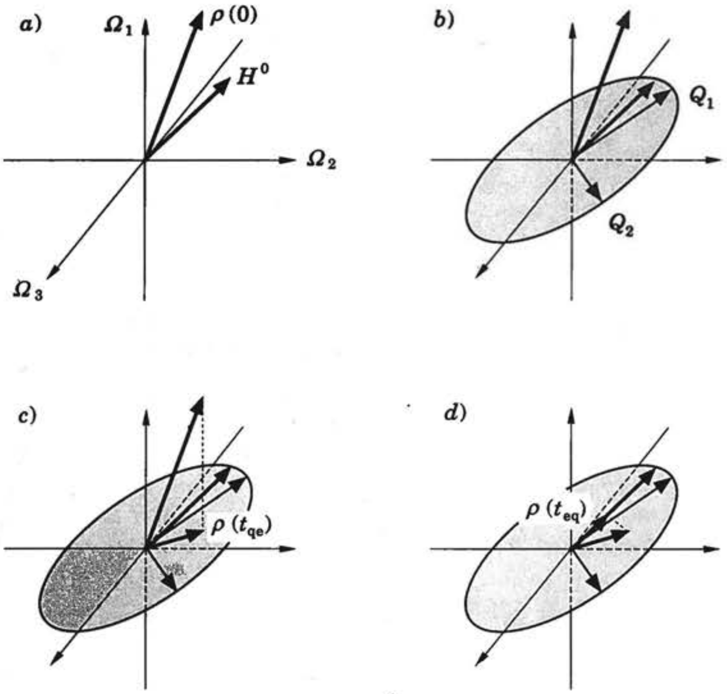

Fig. 6.6. – Given three thermodynamic reservoirs, Ω_1, Ω_2, Ω_3, and an initial density operator $\rho(0)$ (*a*)), then we can define a plane in this space by Q_1 and Q_2, the quasi-invariants of the system, which includes H^0. *b*) Quasi-equilibrium corresponds to a projection of $\rho(0)$ onto the plane (*c*)). Only after comparatively long times (longer than the experimental time scale), is the true equilibrium state reached (*d*)).

width at half-height $\lambda = (1/2)\sqrt{NM_2^I}$. Values of N of around 10 normally produce qualitative agreement with experiment, suggesting that mismatched CP affects strongly the dipolar energies of nearby I spins, but that these effects diffuse only slowly to I spins further away.

Note that this choice of quasi-invariants is only valid around the HH match condition. For other conditions other quasi-invariants must be determined, and indeed one finds that cross-polarization once again becomes efficient at conditions where the S-spin nutation frequency is a multiple of the I-spin frequency, *i.e.* $N\omega_{1I} = \omega_{1S}$[154].

6˙6. *Resolved heteronuclear coupling.* – As a final step towards an improved determination of equilibrium magnetizations we must recognize that in many organic solids the one-bond heteronuclear dipolar coupling is larger than the I-I dipolar couplings. In many cases it is even resolved and is primarily responsible for the oscillations in the buildup shown in fig. 6.5[155].

In order to accurately describe such a situation, we must revise the partition of the quasi-invariants. It is convenient to consider the system as a spin pair in a bath of surrounding protons and to partition the tilted-frame Hamiltonian and the density matrix of the $I_1 S$ spin pair into commuting sum and difference terms [153]:

$$H_{\text{pair}} = \omega_{1I} I_{1z} + \omega_{1S} S_z + b_1 2 I_{1y} S_y \,, \tag{6.46}$$

$$H_{\text{pair}} = H_{\Sigma} + H_{\Delta} \,, \tag{6.47}$$

with

$$H_{\Sigma} = \omega_e^{\Sigma} I_e^{\Sigma} \,, \qquad H_{\Delta} = \omega_e^{\Delta} I_e^{\Delta} \,,$$

$$\omega_e^{\Sigma} = \sqrt{(\omega_{1S} + \omega_{1I})^2 + (b_1)^2} \,,$$

$$\omega_e^{\Delta} = \sqrt{(\omega_{1S} - \omega_{1I})^2 + (b_1)^2} \,,$$

$$I_e^{\Sigma} = I_z^{\Sigma} \cos\theta^{\Sigma} + I_x^{\Sigma} \sin\theta^{\Sigma} \,,$$

$$I_e^{\Delta} = I_z^{\Delta} \cos\theta^{\Delta} + I_x^{\Delta} \sin\theta^{\Delta} \,,$$

$$I_z^{\Sigma} = \frac{1}{2}(I_{1z} + S_z), \qquad I_z^{\Delta} = \frac{1}{2}(I_{1z} - S_z),$$

$$I_x^{\Sigma} = \frac{1}{2}(I_1^+ S^+ + I_1^- S^-), \qquad I_e^{\Delta} = \frac{1}{2}(I_1^+ S^- + I_1^- S^+),$$

and where

$$\operatorname{tg}\theta^{\Sigma} = \frac{b_1}{\omega_{1I} + \omega_{1S}} \,, \qquad \operatorname{tg}\theta^{\Delta} = \frac{-b_1}{\Delta\omega} \,. \tag{6.48}$$

To explain the observed equilibrium values we assume that ρ_{Σ} and ρ_{Δ}, the sum and difference terms in the density operator, reach equilibrium at markedly different rates. Indeed we find that the difference term is isolated from the reservoir of remaining protons, while the sum term comes into contact with the sum term of the bath, as shown qualitatively in fig. 6.7. Note that the separation between energy levels of H_{Σ} is close to $2\omega_{1I}$ at match, and hence thermal contact between these terms is achieved by *double-quantum spin diffusion*. Therefore, we postulate a quasi-invariant Q_1 whose expectation value is conserved under this process,

$$Q_1 = \frac{1}{N+2}(\omega_e^{\Sigma} + N\omega_{1I})\left(2I_e^{\Sigma} + \sum_{2}^{N+1} I_{kz}\right), \tag{6.49}$$

where N is the number of I spins in contact with the spin pair. Taking the perturbation

$$V = H_{II}^{\text{nonsec}} + \sum_{2}^{N+1} b_k 2 I_{kx} S_x \,, \tag{6.50}$$

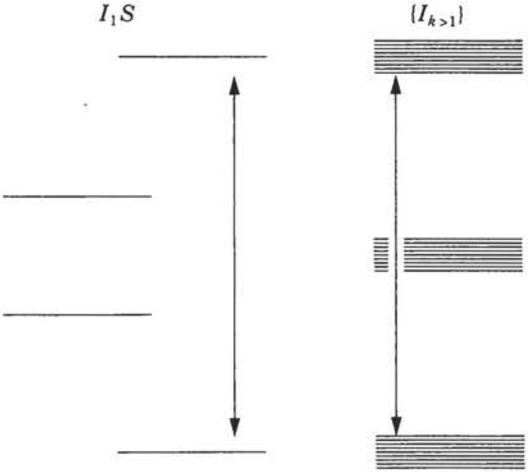

Fig. 6.7. – Schematic representation of the thermodynamic processes responsible for cross-polarization in cases of a resolved heteronuclear coupling. (Adapted from *J. Chem. Phys.*, **84**, 4243 (1986), with permission.)

the remaining quasi-invariants can be derived to be

$$Q_2 = \frac{1}{N+2}(\omega_e^{\Sigma} + 2\omega_{1I})\left(NI_e^{\Sigma} + \sum_2^{N+1} I_{kz}\right) + h_3\Omega_3 \,, \tag{6.51}$$

$$Q_3 = -\omega_e^{\Delta} I_e^{\Delta} \,. \tag{6.52}$$

Assuming strong r.f. fields and making the approximation $\omega_e^{\Sigma} \approx \omega_{1S} + \omega_{1I}$, the quasi-equilibrium density operator may be derived from

$$\rho(t_{\text{qe}}) \approx \frac{\langle \rho(0) | Q_1 \rangle}{\langle Q_1 | Q_1 \rangle} Q_1 + \frac{\langle \rho(0) | Q_2 \rangle}{\langle Q_2 | Q_2 \rangle} Q_2 + \frac{\langle \rho(0) | Q_3 \rangle}{\langle Q_3 | Q_3 \rangle} Q_3 \,. \tag{6.53}$$

The expectation value for the equilibrium S magnetization (in the tilted frame) is found to be

$$\langle S_z \rangle = \frac{\hbar\omega_{0I}}{4kT}\,\frac{1}{2(N+2)}\,\{N\sin^2\theta^{\lambda} + (N+2)\sin^2\theta^{\Delta}\} \tag{6.54}$$

with

$$\operatorname{tg}\theta^{\lambda} = -\frac{\lambda}{\Delta\omega}\sqrt{\frac{2(N+2)}{N}} \,. \tag{6.55}$$

In addition the expectation value for dipolar order can be obtained:

$$\langle 2I_{1y}S_y \rangle = \frac{\hbar\omega_{0I}}{4kT}\,\frac{1}{2}\left\{-\sin\theta^{\Sigma}\left(1 + \frac{N}{N+2}\sin^2\theta^{\lambda}\right) + \sin\theta^{\Delta}\cos\theta^{\Delta}\right\} \tag{6.56}$$

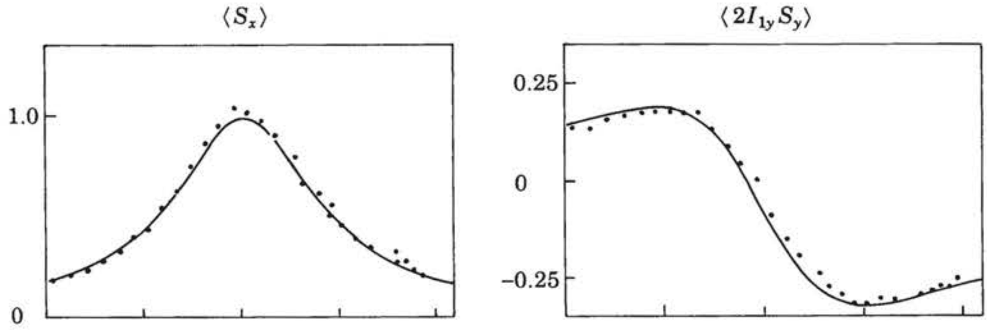

Fig. 6.8. – Dependence of equilibrium S-spin polarization for a single crystal of ferrocene on the S-spin r.f. field. The theoretical curves are predicted using eqs. (6.54) and (6.56), with the dipolar coupling $b_1/2\pi = 10.7\,\text{kHz}$, $N = 10$ and $\lambda/2\pi = 7.0\,\text{kHz}$. (Adapted from *J. Chem. Phys.*, **84**, 4243 (1986), with permission.)

using $\alpha_{0I}\,\text{Tr}\,\{S_x^2\} = \hbar\omega_{0I}/4kT$. As shown in fig. 6.8, these equations give excellent agreement with experiment for the expectation values of both the S magnetization and the dipolar order (which can easily be observed indirectly) in the example of ferrocene. This suggests that the postulated quasi-invariants are a good approximation to reality.

7. – Unitary bounds on spin dynamics.

In this section we shall consider some limits on polarization transfer imposed by the unitary quantum dynamics. Normally, one would expect that the total polarization of the N I spins, which amounts to $\sqrt{N}$ in an $I_N S_M$ system, could be transferred to the M S spins to which they are coupled. This limit is often referred to as the entropy limit since it is the maximum achievable polarization transfer that one can expect from a thermodynamic approach, as we derived in subsect. **6**'3.

In fact *for an isolated system* the amount which can be transferred is always less than the $\sqrt{N}$ limit [156-161]. It has been shown that, if the mechanism for transfer is a unitary transformation, polarization transfer is always incomplete in $I_N S_M$ systems where $M < N$ [156]. The origin of this effect is that we do not expect the finite $I_N S_M$ system to behave thermodynamically unless both N and M are large, or the $I_N S_M$ system is part of an ensemble of coupled $I_N S_M$ systems, or the $I_N S_M$ system is coupled to a bath or thermodynamic reservoir.

7'1. *Unitary evolution.* – The evolution of the density matrix ρ in an $I_N S_M$ system in the absence of dissipative behavior such as relaxation is governed by the Liouville-von Neumann equation [2-5]

$$d\rho/dt = -i[H(t), \rho(t)], \tag{7.1}$$

and, as we have seen when H is time-independent, the solution of eq. (7.1) is simply

$$\rho(t) = U\rho(0)\,U^{-1}\,,$$

where U represents a unitary transformation. Even when H is time-dependent, a solution to eq. (7.1) can be found by dividing $H(t)$ into a series of sufficiently small parts $H_1 H_2 \dots H_n$ such that each part can be considered time-independent. The solution of eq. (7.1) then becomes

$$\rho(t) = U_n \dots U_2 U_1\, \rho(0)\, U_1^{-1} U_2^{-1} \dots U_n^{-1}\,. \tag{7.2}$$

Unitary transforms govern the spin dynamics of all NMR experiments, if we neglect relaxation. The evolution of the density operator describes a trajectory in a Liouville space formed by n^2 orthogonal basis operators Ω_k. At any time the density operator $\rho(t)$ corresponds to a point $(a_1, a_2, \dots, a_{n^2})$ where the a_k are given by

$$a_k = \langle \Omega_k \,|\, \rho \rangle\,. \tag{7.3}$$

7·2. *The entropy limit.* – The amount of spin order in the spin system is given by $\langle \rho \,|\, \rho \rangle$. Since we are considering unitary evolution, this quantity is conserved and evolution satisfies the condition

$$\langle \rho(t) \,|\, \rho(t) \rangle = \langle \rho(0) \,|\, \rho(0) \rangle\,. \tag{7.4}$$

Given the initial density operator

$$\rho(0) = (r(0)\cos\theta(0),\, r(0)\sin\theta(0),\, 0,\, \dots,\, 0)\,, \tag{7.5}$$

then

$$r(0)^2 = r(t)^2 + \sum_{3}^{n^2} a_k^2(t)\,, \tag{7.6}$$

which leads to the constraint

$$|r(t)| \leqslant |r(0)|\,, \tag{7.7}$$

which is known as the entropy bound. For example, this corresponds to the case of $|r(t)| \leqslant \sqrt{N}$ in the $I_N S$ system shown in subsect. 7·7.

7·3. *Bounds on unitary evolution.* – SØRENSEN [156] has shown that the total amount of achievable polarization transfer in a unitary regime is governed by a theorem about normal matrices [162] and that actual bounds on evolution applicable to unitary behavior depend only on the eigenvalue spectra of the relevant operators. Defining $\Lambda(A)$ as an n-dimensional vector containing the n eigenvalues of an operator A ordered from highest to lowest, we make use of the inequality

$$\langle A \,|\, B \rangle \leqslant \Lambda(A) \cdot \Lambda(B)\,, \tag{7.8}$$

which is related to the Schwartz inequality. Since eigenvalues are conserved by unitary transform, $\rho(t)$ satisfies

$$\langle A \,|\, \rho(t) \rangle \leqslant \Lambda(A) \cdot \Lambda(\rho) . \tag{7.9}$$

Equation (7.9) can be summarized as saying that the projection of the density operator onto any operator Ω can never be more than the maximum value obtained by summing products of individual eigenvalues. *This limit is always less than or equal to the entropy limit.* For example, in an I_2S system, the simplest system with $N \neq M$, eq. (7.9) shows that the maximum amount of S polarization achievable using unitary behavior is $1S_z$ rather than the $\sqrt{2}\,S_z$ which corresponds to the entropy limit.

7·4. *Redfield's description of polarization transfer.* – REDFIELD [160] has provided an elegant demonstration of the unitary limit. In subsect. 6·3 we showed how adiabatic demagnetization of the I spin in a two-spin IS system, followed by adiabatic remagnetization of the S spin, resulted in complete polarization transfer. Let us consider the same process in an I_2S system, as illustrated in fig. 7.1. Initially there are two levels with energy approximately $\gamma_I H_I$ ($\hbar = 1$), four with energy zero and two with energy $-\gamma_I H_I$ (left-hand side of fig. 7.1). These sets of levels are not degenerate, being split by the heteronuclear dipolar interaction. We assume that the occupation of the levels is $a - \varepsilon$, a and $a + \varepsilon$, where $a = 1/8$, and their total spin angular-momentum values m_{Ii} are -1, 0 and $+1$, respectively. This yields an initial polarization, defined as the sum over all eight levels of $\Delta_I = \sum_i P_i m_{Ii}$, which equals 4ε.

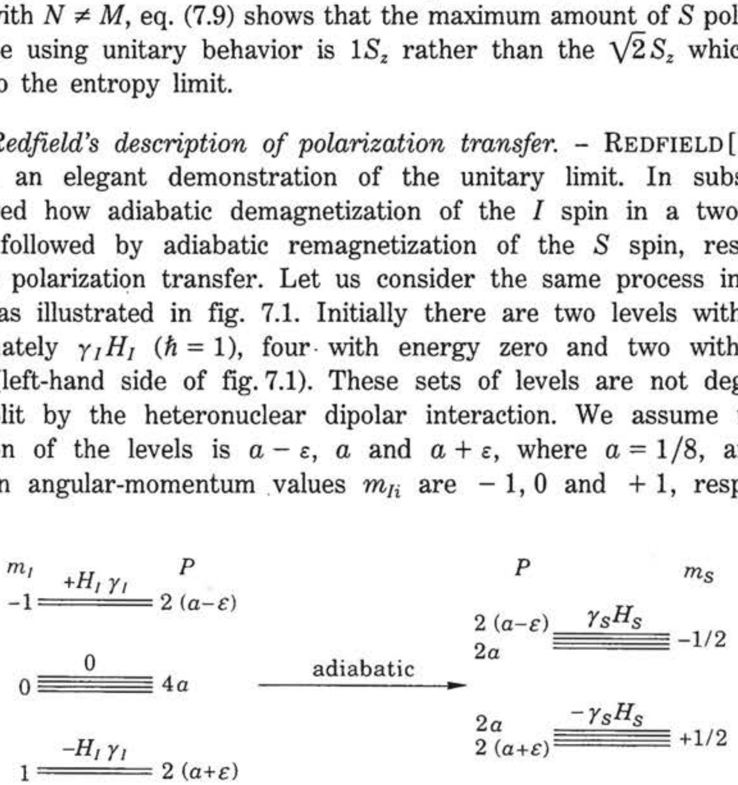

Fig. 7.1. – Energy levels and populations before (left) and after (right) adiabatic demagnetization of the I spins followed by adiabatic remagnetization of the S spin in an I_2S system. Only one unit of I polarization is transferred to the S spin.

After the demagnetization and remagnetization (right-hand side of fig. 7.1), we have two groups of four energy levels separated by energy of approximately $(1/2)\gamma_S H_S$. In this case their total spin angular momentum is $\pm 1/2$, and the populations are determined as described above by retaining the ordering of the populations that existed initially (since the whole process was adiabatic). Thus in the upper group of levels there are two with occupation probability $P_i = a - \varepsilon$ and two with $P_i = a$. Similarly for the lower group, two levels have $P_i = a + \varepsilon$, and two have $P_i = a$. The final polarization, which is the sum $\Delta_S = \sum_i P_i m_{Si}$, is, therefore, equal to 2ε.

Thus there is a net polarization loss by a factor of 0.5, or an efficiency of transfer to single S spin of one unit of initial I-spin polarization. In terms of the norm of the density matrix, this means the polarization has been reduced by a factor $1/\sqrt{2}$ from $P_I = \sqrt{1+1} = \sqrt{2}$ to $P_I = \sqrt{1} = 1$, exactly in agreement with the prediction made in subsect. 7·3.

7·5. *Bounds in $I_N S$ systems.* – We can generalize the results obtained for S polarization in the IS and I_2S cases to I_NS without too much difficulty by deriving the following formulae for the maximum amplitude of S polarization:

$$a^{\max}(N = 2m+1) = a^{\max}(N = 2m+2)\,, \tag{7.10}$$

$$a^{\max}(N = 2m+1) = \binom{2m}{m}(2m+1)\,4^{-m}\,. \tag{7.11}$$

Figure 7.2 shows $a^{\max}/\sqrt{N}$ as a function of the number of I spins. Even in the limit of $N \to \infty$ the amount of S polarization does not reach the entropy limit.

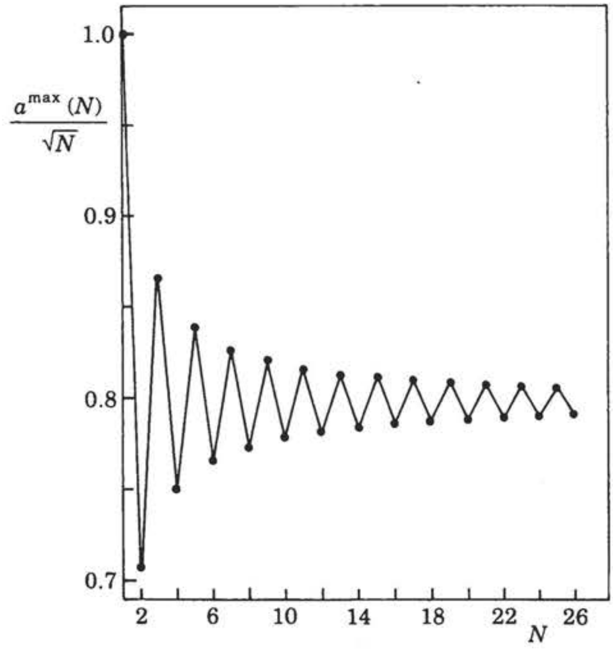

Fig. 7.2. – Illustration of the maximum possible transfer efficiency relative to the efficiency predicted by the entropy bound for the transfer of I-spin polarization to S spins in an I_NS system. (Adapted from *J. Magn. Reson.*, **86**, 435 (1990), with permission.)

Indeed, using Stirling's formula,

$$n! \approx \left(\frac{n}{e}\right)^n \sqrt{2\pi n}\,, \tag{7.12}$$

which is valid for large n, we can derive a comparison of the two bounds for large N:

$$\frac{a^{\max}}{\sqrt{N}} \approx \sqrt{2/\pi} \approx 0.80\,. \tag{7.13}$$

We find that unitary behavior only reproduces the thermodynamic entropy limit when both N and M are large.

7·6. *The thermodynamic limit.* – By extending Redfield's model (subsect. 7·4) to larger spin systems we gain more insight into spin temperature, since the final distribution gets closer and closer to the Boltzmann distribution. For example, in an I_4S_2 system, in analogy to fig. 7.1 the uppermost set of four levels has energy roughly $2\hbar\gamma_I H_I$, quantum number $m_{Ii} = -2$, and $P_i = a - 2\varepsilon$, where $a = 1/64$. The next uppermost set of sixteen levels has $m_{Ii} = -1$ and $P_i = a - \varepsilon$. The middle set of 24 levels has $m_{Ii} = 0$ and $P_i = a$, and the lower levels mirror the upper ones. The spin polarization is 64ε. After adiabatic transfer of polarization the two S spins have three sets of levels. The upper and lower set each contain 16 levels with $-m_{Si} = \pm 1$. The populations of the upper set are 4 levels with $P_i = a - 2\varepsilon$ and 12 with $P_i = a - \varepsilon$. The final polarization this time is 40ε, giving a polarization efficiency of $40/64$, which is greater than for the I_2S case. This is a consequence of the fact that, as the number of I and S spins gets larger, the initial and final distributions of eigenvalues resemble each other and are binomial. Thus Redfield's simple treatment sheds a large amount of light on the connection between spin dynamics of isolated systems and the thermodynamic limit.

To calculate the maximum enhancements for $M > 1$ we remark that the binomial distribution of eigenvalues of the I spins is increasingly well approximated by a normal distribution. Hence the limit $N \to \infty$ was represented by substitution of the binomial for a normal distribution in eq. (7.13). For $M > 1$ we can do this by matching the normal distribution of the I eigenvalues with the binomial distribution of the S eigenvalues, and it can be shown that

$$\frac{a^{\max}(N \to \infty\,, M)}{a^{\text{entropy}}(N \to \infty\,, M)} = \sqrt{\frac{8}{M\pi}}\left\{\sum_{i=0}^{(M-2)/2} \exp\left[-\frac{1}{2}\left(g\left(1 - 2^{-M}\sum_{j=0}^{i}\binom{M}{j}\right)\right)^2\right]\right\}, \tag{7.14}$$

where g is the inverse of the function

$$F(x) = \frac{1}{\sqrt{2\pi}}\int_{-\infty}^{x} \exp[-u^2/2]\,\mathrm{d}u\,. \tag{7.15}$$

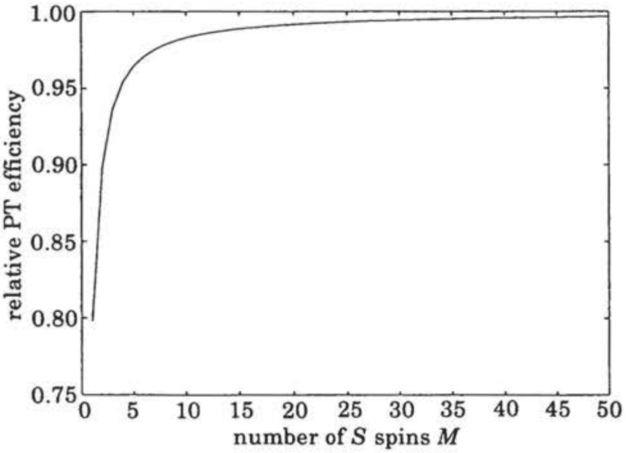

Fig. 7.3. – Relative efficiency of polarization transfer in an $I_N S_M$ spin system as a function of M when N tends to infinity. (Adapted from *J. Magn. Reson.*, **93**, 648 (1991), with permission.)

Equation (7.14) is plotted as a function of M in fig. 7.3, where we see the tendency towards maximum polarization transfer for large M. Indeed, as $M \to \infty$, matching of two normal distributions with standard deviations $\sigma_I = \sqrt{N/2}$ and $\sigma_S = \sqrt{M/2}$ amounts to

$$a^{\max}(N \to \infty, M \to \infty) = \tag{7.16}$$

$$= \frac{(1/\sigma_I \sqrt{2\pi}) \int_{-\infty}^{\infty} u^2 (\sigma_S/\sigma_I) \exp[-u^2/2\sigma_I^2]\, du}{(1/\sigma_S \sqrt{2\pi}) \int_{-\infty}^{\infty} u^2 \exp[-u^2/2\sigma_S^2]\, du} = \frac{\sigma_I \sigma_S}{\sigma_S^2} = \sqrt{\frac{N}{M}},$$

which is the entropy limit.

7·7. *Two-dimensional bounds.* – We make use of a graphical technique recently introduced by LEVITT [161], in which the region of Liouville space accessible through unitary transformation is mapped as a function of two operators Ω_1 and Ω_2. For example, an obvious choice of operators might be

$$\begin{cases} \Omega_1 = \dfrac{1}{\sqrt{N}} I_z \\ \text{and} \\ \Omega_2 = S_z , \end{cases} \tag{7.17}$$

where

$$I_z = \sum_{1}^{N} I_{iz}\,. \tag{7.18}$$

These two operators define a plane in Liouville space, and we can map the accessible states by evaluating eq. (7.9) for the linear combination

$$\Omega_r = \Omega_1 \cos\theta + \Omega_2 \sin\theta \tag{7.19}$$

for all values of θ. In fig. 7.4*a*) we see how this leads to a region of accessible space for a two-spin *IS* system when $\rho(0) = I_{1z}$ for $\Omega_1 = I_z$ and $\Omega_2 = S_z$. In fig. 7.4*b*) we see the region of allowed space for a three-spin system $I_2 S$, which is the simplest system we can consider with $N \neq M$. In this case $\rho(0) = I_{1z} + I_{2z}$ for $\Omega_1 = I_{1z} + I_{2z}$ and $\Omega_2 = S_z$, and we see that the region of allowed states intersects the S_z axis at a value of 1. In the particular plane considered in fig. 7.4*b*) the maximum size of the projection of the spin vector onto the plane is continuously getting smaller as θ gets larger. As we are dealing purely with unitary transformations, the norm of the total spin vector (which represents the degree of spin order and is proportional to the entropy of the system) must be conserved, which indicates that other operators must be involved. Indeed, if we consider instead $\Omega_1 = I_{1z}$ and $\Omega_2 = S_z$, again with $\rho(0) = I_{1z} + I_{2z}$, we note that the size changes in a different way (fig. 7.4*c*)) and there is a combination corresponding to $\Omega_r = I_{1z} + S_z$ which has an amplitude equal to the entropy limit. Thus $\rho(0) = I_{1z} + I_{2z}$ can be completely converted into $\rho(t) = I_{1z} + S_z$. This simple two-dimensional representation can be easily extended to a subspace of three or more dimensions, but we usually find that the two-dimensional projections of fig. 7.4 are the most useful.

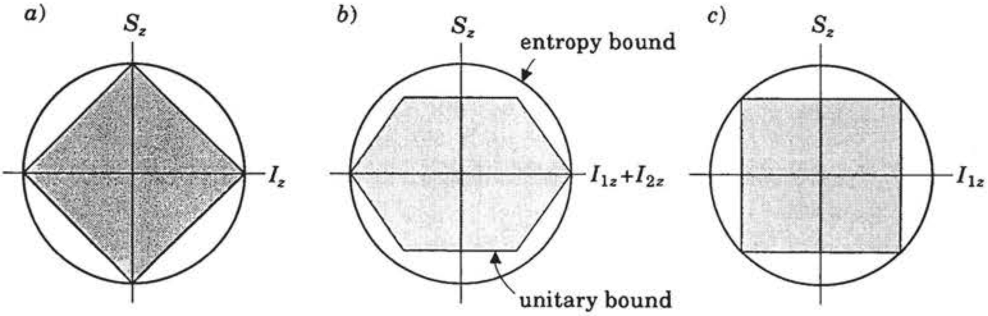

Fig. 7.4. – The shaded regions are projections of the regions of Liouville space accessible within the unitary bound onto planes defined by *a*) S_z and $I_{1z} + I_{2z}$ in an *IS* system with $\rho(0) = I_z$ and *b*) S_z and $I_{1z} + I_{2z}$ for an $I_2 S$ spin system, and *c*) S_z and I_{1z} for an $I_2 S$ spin system. Both *b*) and *c*) have $\rho(0) = I_{1z} + I_{2z}$. The circles correspond to the entropy limit of $\sqrt{N}$ polarization. Note that in both *b*) and *c*) the region intercepts the S_z axis at a value of 1.0, but that in *c*) the region touches the entropy bound for $\Omega_r = I_{1z} + I_z$.

7·8. *Transfer of basis operators.* – In an I_2S system a total of 32 products of Cartesian operators form a basis set. They can be divided into 8 classes:

$$I_{1\alpha},\ I_{2\alpha},\ S_{\alpha},\ 2I_{1\alpha}I_{2\beta},\ 2I_{1\alpha}S_{\beta},\ 2I_{2\alpha}S_{\beta},\ 4I_{1\alpha}I_{2\beta}S_{\gamma},\ 1, \tag{7.20}$$

where α, β, γ are interchangeably x, y, z. Each of the operators within each class share common eigenvalues. If we take a linear combination of two of these operators according to eq. (7.9), we find that, when Ω_1 and Ω_2 belong to the above set, $\Lambda(\Omega_r)$ *is the same for all combinations* Ω_1 *and* Ω_2 with values of

$$\begin{cases} \Lambda_{11} = \Lambda_{22} = \cos\theta + \sin\theta\,, \\ \Lambda_{33} = \Lambda_{44} = \cos\theta - \sin\theta\,, \\ \Lambda_{55} = \Lambda_{66} = \sin\theta - \cos\theta\,, \\ \Lambda_{77} = \Lambda_{88} = -\cos\theta - \sin\theta\,. \end{cases} \tag{7.21}$$

Taking the product $\Lambda(\Omega_r)\cdot\Lambda(\rho(0))$ where $\rho(0) = I_{1z} + I_{2z}$, we find the maximum amplitude of the projection of the spin vector onto the plane $a^{\max} = \sqrt{2}$ for $\theta = 45°$. Thus *any* combination of $\rho(0)$ which consists of a sum of two basis operators can be completely transferred into a sum of *any* other two basis operators, provided the operators within each sum commute with each other. In contrast, two operators cannot be entirely converted into one by unitary behavior. In general we can state the following principle: *Any sum of k commuting basis operators can be entirely converted by unitary transform into a sum of k other commuting basis operators.*

This rule is subject to some restrictions imposed by symmetry in that the sums of operators must belong to the same irreducible representation of the spin Hamiltonian [163]. For example, in an I_2S system the sum $\Omega_r = 2(a_1 I_{1\alpha} I_{2\beta} + a_2 I_{1\alpha} S_\beta + a_3 I_{2\alpha} S_\beta)$ possesses inversion symmetry (*i.e.* it is invariant under the operation of inversion $A' = UAU^{-1}$, where $U = \exp\left[-i\left(\sum_i \pi I_{ix}\right)\right]$ and A is the diagonal matrix of eigenvalues of Ω), and has degenerate eigenvalues, whereas a sum of any other set of three operators in this system, such as $\Omega_r = a_1 I_{1\alpha} + a_2 I_{2\alpha} + a_3 S_\beta$, is antisymmetric under inversion (*i.e.* $A' = -A$) and does not have any degenerate eigenvalues (barring accidental degeneracy if the coefficients are equal). Unitary transformation does not change the symmetry of the density matrix, and cannot, therefore, interconvert these two operators. In order to avoid symmetry-related problems, we shall consider only sums of odd operators (*i.e.* single-spin operators of the type $I_{i\alpha}$), which always belong to the same irreducible representation, in the following examples.

7·9. *Nonunitary evolution.* – To avoid the restrictions of unitary limits we must change the eigenvalues of the density matrix contained in $\Lambda(\rho)$ by invoking a nonunitary transformation. One mechanism of nonunitary transformation is relaxation, which can be seen as a way of increasing the size of the system through the dipolar interaction. As far as polarization transfer experiments are concerned, we may ignore the origins of the relaxation process, as it is only the form of the relaxation matrix R that is important. The equation of motion of the

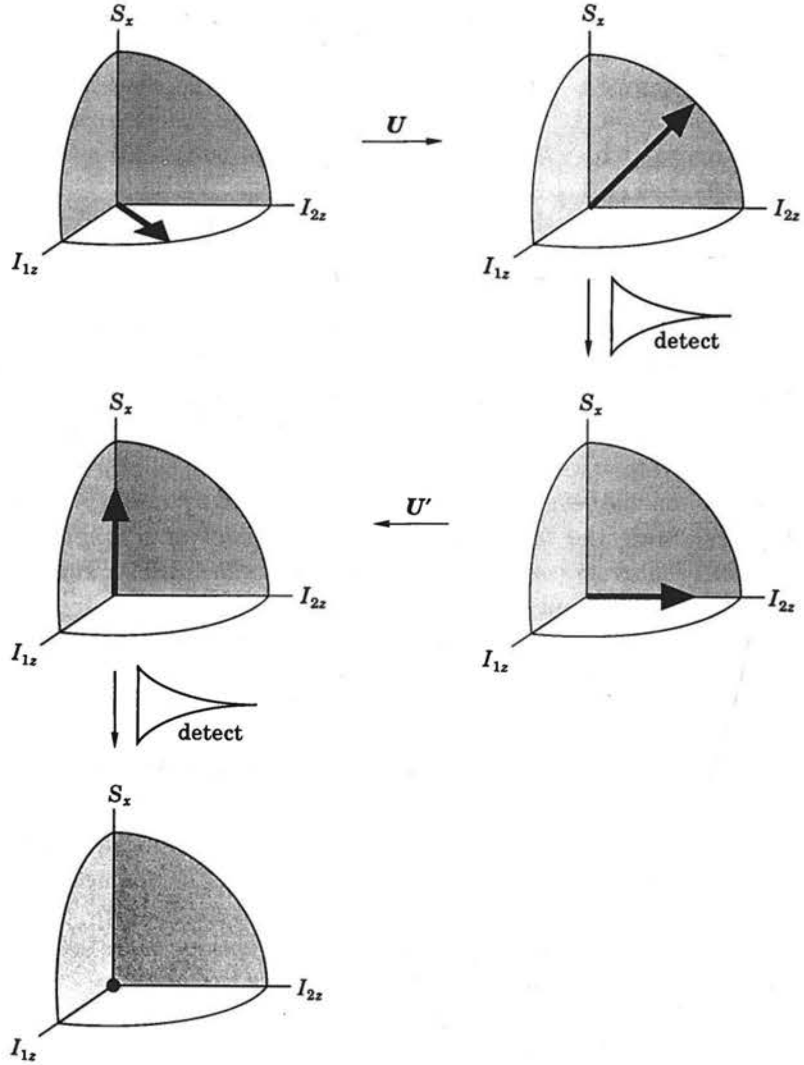

Fig. 7.5. – Schematic representation of an experiment which utilizes transverse relaxation to enhance polarization transfer. In the first step $\rho(0) = I_{1z} + I_{2z}$ is transformed into $\rho = I_{2z} + S_x$ by a unitary transformation U. A signal corresponding to polarization transfer of 1 unit is then acquired as S_x decays to zero through the effect of R. The resulting I_{2z} is then transferred by U' to S_x and a second signal is acquired. The final signal-to-noise ratio is $\sqrt{2}$.

density matrix is modified to become[117, 131, 164]

$$\text{(7.22)} \qquad \mathrm{d}\rho/\mathrm{d}t = -i[H(t), \rho(t)] + R(\rho(t) - \rho(\infty)),$$

where R is a tetradyadic with four subscripts and where the element $R_{ab,\, cd}$ connects the elements ρ_{ab} and ρ_{cd}. If we include only transverse autocorrelation as a relaxation mechanism, R is particularly simple and only contains elements $R_{ab,\, ab}$ $(a \neq b)$ with the result that the off-diagonal elements ρ_{ab} will decay at a rate $-R_{ab,\, ab}$ which depends on the spectral densities. For our purposes it is convenient to adopt a normal-mode analysis[131] where the normal modes of the system are the $n = 2^{N+M}$ Cartesian basis operators of the $I_N S_M$ system. The evolution of the density matrix under the effect of relaxation alone is now given by

$$\text{(7.23)} \qquad \mathrm{d}\rho/\mathrm{d}t = \Gamma\nu(t),$$

where $\nu(t)$ is a vector containing elements $\nu_1 \ldots \nu_n$ corresponding to the n basis operators. In the case under consideration Γ only contains diagonal elements which affect transverse operators. For the moment we wish to observe simply that, if we allow the system to reach equilibrium $(t \to \infty)$, the effect of transverse relaxation is to remove all the transverse components of the density matrix.

We can now envisage the *gedanken* experiment shown in fig. 7.5 which is capable of achieving the thermodynamic limit for polarization transfer. For the sake of convenience we have assumed that the time scale of relaxation is much longer than that of U. We note that, if $\rho = S_x + I_{2z}$, then we can detect S_x (or any other observable), which *simultaneously decays to zero* through T_2, whilst I_{2z} (or any longitudinal state) remains unaffected as long as T_1 is sufficiently long. The action of detection corresponds to a nonunitary operator which removes the transverse components of the spin vector whilst at the same time accumulating a signal of size 1. Thus, after the first detection period in the experiment of fig. 7.5, we are left with a density matrix which only contains one operator; by detecting the signal and allowing transverse relaxation to take effect we have changed the numerical values of the eigenvalues of the density matrix. In the experiment of fig. 7.5 there are two detection periods, during each of which we can acquire a signal of size 1. Thus the total resulting signal of 2, coupled with a total random noise level of $\sqrt{2}$, leads to a final signal-to-noise ratio of $\sqrt{2}$, which is the entropy limit. The most reassuring feature of the experiment *is that by changing the eigenvalues of the density matrix nonunitary dissipative behavior can be used to enhance overall accumulated polarization transfer.*

7·10. *Cross-polarization echoes.* – Before leaving the subject of unitary limits we remark that much of the language in which cross-polarization was discussed in sect. **6** suggests that it is an irreversible process. One speaks loosely of polarization «diffusion» and of projection of the magnetization. However, we have emphasized here that the dynamics are in fact governed by unitary processes. If this is the case, then, although the dynamics are such that forward transfer may be incomplete, reversing the process should be entirely feasible. Therefore, as we saw in subsect. **1**'10, we should be able to apply time-reversal techniques to cross-polarization. Indeed, it is quite obvious that time reversal of both H_{II} and H_{IS} would lead to the formation of a cross-polarization echo.

8. – **Zero-field** NMR.

One of the motivations for doing multiple-quantum NMR described in early sections was to simplify complex spectra. There the complexity of the spectra arose from homogeneous effects, such as the large number of dipolar couplings. But spectra may be intractably complex and broad owing to inhomogeneous broadening as well, which arise from orientational distributions that produce superpositions of inherently simple spectra. This broadening occurs in disordered systems such as polycrystalline solids, amorphous materials, or partially ordered polymers or biological compounds. Because of the anisotropy of the dipolar and quadrupolar interactions, molecules or small groups of spins exhibit different spectra for different orientations; the complete spectrum, therefore, reflects subspectra from all the different orientations, superposed to form a broad, often featureless «powder pattern» from which little information can be obtained.

An example of the proton NMR spectrum of a polycrystalline organic solid, containing four hydrogens per molecule, is shown in fig. 8.1. The situation is similar to that encountered in crystallography by X-ray or neutron diffraction. Although oriented crystals provide diffraction patterns from which structural information can be extracted, a polycrystalline sample yields a considerably less useful powder pattern. We have already considered some methods for removing this broadening in sect. **2** and **5**. Another solution to this problem is to perform the NMR in zero field, using principles well known in other forms of magnetic resonance, for example nuclear quadrupolar resonance (NQR)[165] or optically detected electron paramagnetic resonance (EPR). *In the absence of a magnetic field defining an axis in space, all orientations are equivalent and orientationally disordered materials should provide sharp «crystallike» spectra.* The only problem is to overcome the low sensitivity inherent in the low frequencies of zero-field NMR. To take advantage of the high resolution of zero field and the high sensitivity of high field, we employ adaptations of well-known field-cycling methods[166-173].

A diagram of the simplest field cycle and the corresponding apparatus needed is given in fig. 8.2[174]. Removal of the sample to an intermediate field, followed by a sudden transition to zero field, causes the magnetization carried from the high field to oscillate at frequencies characteristic of local magnetic dipolar or electric quadrupolar interactions. Reapplication of the high field per-

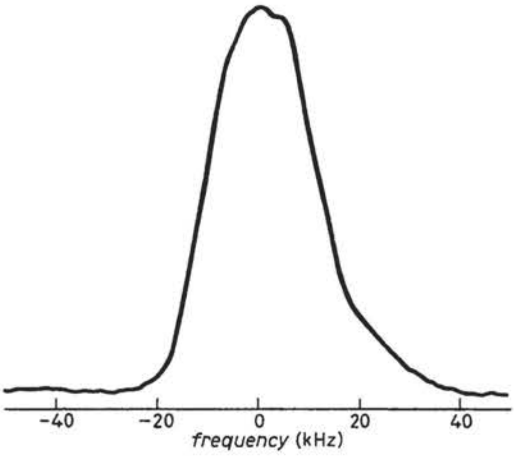

Fig. 8.1. – High-field NMR spectrum of a polycrystalline 1, 2, 3, 4-tetrachloronaphthalene-bis(hexachlorocyclopentadiene) adduct, a four-proton system. As in many dipolar powder patterns, little structure is resolved even though only a small number of spins are strongly coupled together. (Adapted from *J. Chem. Phys.*, 83, 4877 (1985), with permission.)

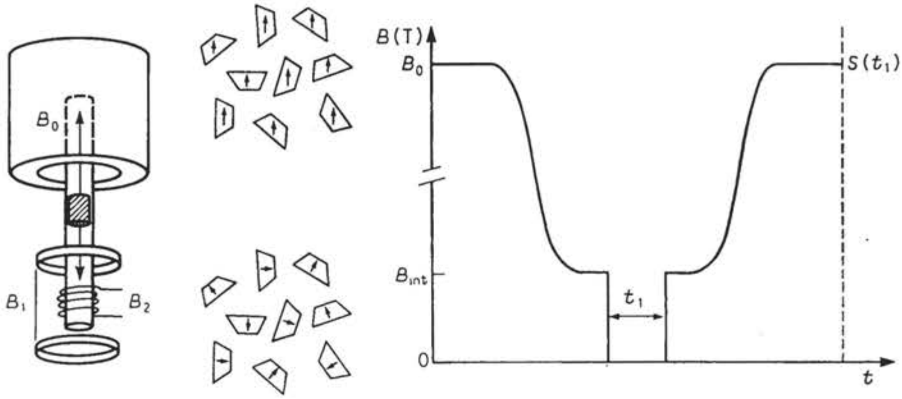

Fig. 8.2. – Zero-field NMR cycle. The applied field is decreased adiabatically by mechanically shuttling the sample out of the bore of a superconducting magnet. The magnetization, preserved in this process, is maintained by an intermediate field, B_1, which is larger than the local internal fields. A second coil produces a pulsed field B_2 that rapidly cancels all other fields and initiates evolution of the spin system in zero field. The local interactions now determine the axis system in zero field and are identical for all crystallites. Reapplication of the intermediate field terminates the zero-field evolution, and the sample is returned to high field, where the magnitude of the signal is measured. The period t_1 is increased incrementally in successive field cycles to produce a time domain signal which produces the zero-field NMR spectrum upon Fourier transformation. (Adapted from *Acc. Chem. Res.*, **20**, 47 (1987), with permission.)

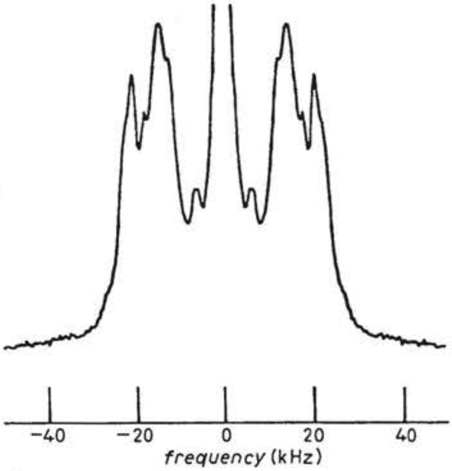

Fig. 8.3. – Zero-field NMR spectrum of the same solid sample shown in fig. 8.1. The sharp peak at zero frequency is truncated for purposes of display. The evolving zero-field magnetization was sampled at 5 μs increments to give an effective zero-field bandwidth of 100 kHz. From the spectrum the configuration of the four-spin central ring could be determined. (Adapted from *J. Chem. Phys.*, 83, 4877 (1985), with permission.)

mits sensitive detection as a function of the time spent in zero field. Fourier transformation of this time domain signal will produce a zero-field frequency domain spectrum with high resolution and full high-field sensitivity. As an example, the zero-field NMR spectrum of a polycrystalline sample of the four-proton spin system of fig. 8.1 is shown in fig. 8.3 [171]. The relative positions of the hydrogens and the conformation of the central cyclohexane ring can be determined from such a spectrum.

8·1. *Zero-field* NQR *of deuterium.* – Frequency domain methods have long been used to observe quadrupolar nuclei ($I \geqslant 1$), where direct detection of the quadrupolar resonance is possible at high frequency. These methods are of limited applicability, however, when the frequencies are low (< 100 kHz), as, for example, with deuterium. Moreover, direct detection requires the use of radiofrequency irradiation in zero field. Clearly, Fourier transform experiments of the type described in the previous section can avoid many of these problems. As an example, the high-field 55.6 MHz deuterium NMR spectrum of perdeuterated polycrystalline diethylterephthalate is shown in fig. 8.4*a*) [175]. Only the most prominent singularities of the methyl, methylate and aromatic lineshapes can be resolved, since the deuterium signal is distributed over a wide bandwidth (although in favorable cases it can be «dePaked»). In contrast, the zero-field deuterium spectrum in fig. 8.4*b*) displays four distinct groups of peaks with sharply resolved fine structure. From such a spectrum resonances from different sites in the molecule can be assigned. In this case, five inequiva-

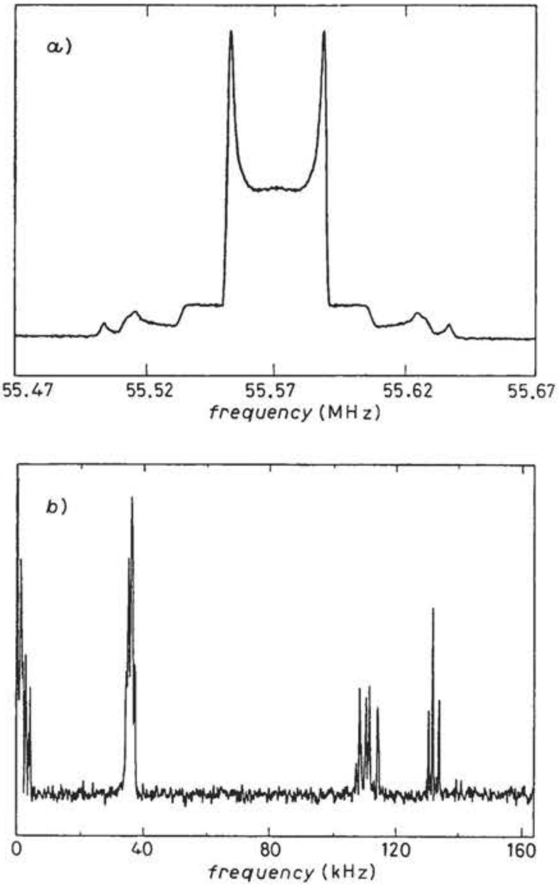

Fig. 8.4. – *a*) Deuterium high-field NMR spectrum of polycrystalline perdeuterated diethylterephthalate, $CD_3CD_2OOCC_6D_4COOCD_2CD_3$. Only the singularities of the methylene and aromatic sites are distinguishable in this broad powder pattern. Three separate quadrupolar sites can be discerned from the overlapping powder lineshapes. *b*) Zero-field deuterium NQR spectrum of the same sample. Four distinct frequency regions with resolved peaks are evident corresponding to, in order of decreasing frequency, the aromatic, methylene, methyl sites and ν_0 lines. Quadrupolar coupling constants and small asymmetry parameters were established for five inequivalent sites in the molecule. (Adapted from *J. Magn. Reson.*, **69**, 243 (1986), with permission.)

lent sites are established: methyl, two inequivalent methylenes and two inequivalent aromatics. The high resolution of the zero-field experiment permits the measurement of very similar quadrupolar coupling constants and small asymmetry parameters. Figure 8.5 shows a further example with perdeuterated solid dimethoxybenzene [176]. The two doublets around 135 kHz arise from the inequivalence of deuteron sites in the aromatic ring created by the frozen solid-state conformation of the molecule. Many nuclei with low quadrupolar fre-

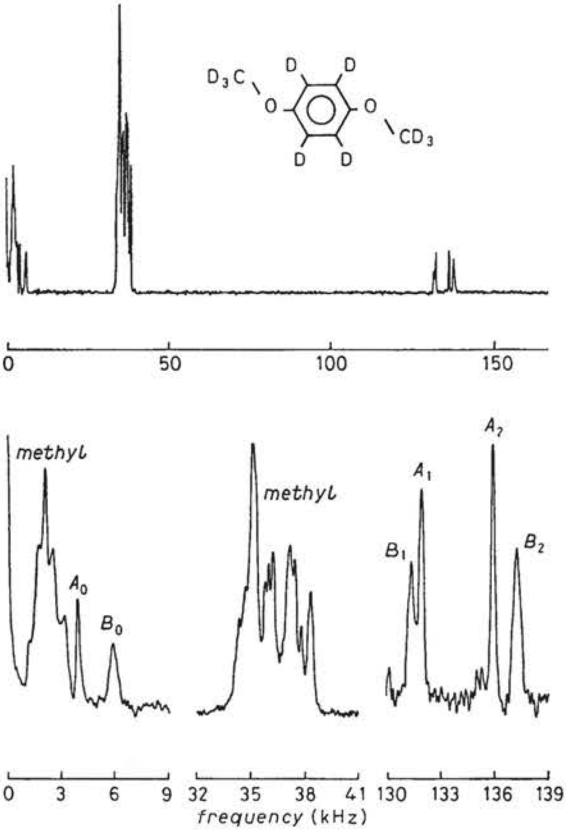

Fig. 8.5. – Fourier transform zero-field deuterium NQR spectrum of polycrystalline perdeuterated 1,4-dimethoxybenzene. The upper plot shows the full spectrum. The lower plot shows expanded views of the three resonance regions assignable to aromatic deuterons, aliphatic deuterons and ν_0 lines. There are two pairs of lines indicating different quadrupole couplings and asymmetry parameters for the aromatic deuterons. The differences are due to the solid-state molecular conformation, which renders pairs of the aromatic positions inequivalent. (Adapted from *J. Chem. Phys.*, **80**, 2232 (1984), with permission.)

quencies are directly accessible by such zero-field NQR studies, and among those studied in our laboratory, in addition to deuterium, are ^{7}Li [175], ^{14}N [177], ^{11}B [178] and ^{27}Al [179].

8·2. *Two-dimensional zero-field* NMR. – Connections between zero-field NMR and NQR transitions (which relate to connections between molecular sites) can be determined by extending the experiment to incorporate two time periods in zero field [174, 180]. The basic idea is to obtain the signal as a function of two independent time variables, t_1 and t_2, and then to Fourier transform

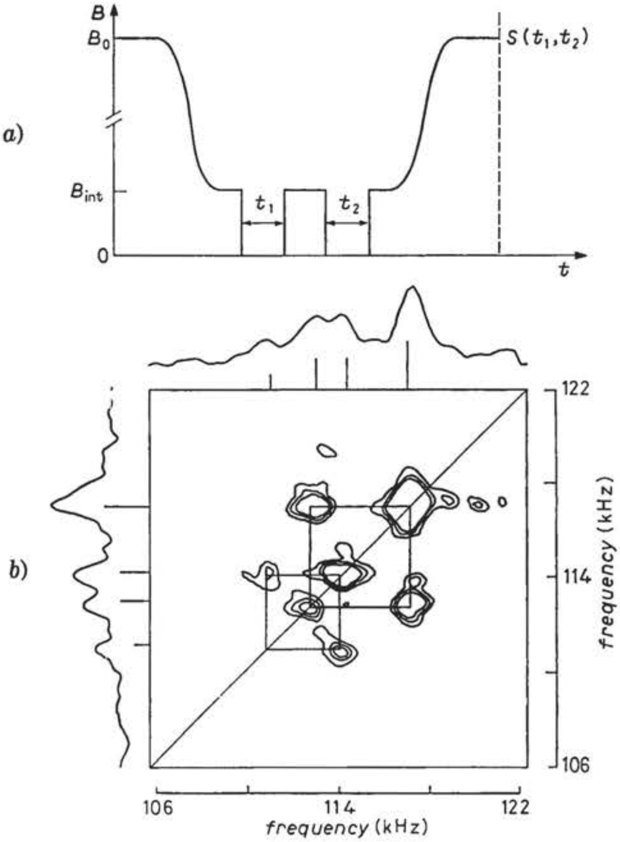

Fig. 8.6. – Two-dimensional zero-field cycle and spectrum of selectively deuterated (CD_2) solid diethylterephthalate. The zero-field spectrum is obtained as a function of two independent time variables, t_1 and t_2, which are separated by application of an intermediate pulsed field. This mixing transfers coherence between the zero-field transitions. As seen in the experimental spectrum, off-diagonal peaks indicate connectivities between the zero-field quadrupolar transitions. In this case, transitions can be assigned to inequivalent deuterium sites in each CD_2 group. (Adapted from *Chem. Phys. Lett.*, **129**, 55 (1986), with permission.)

against both to obtain a two-dimensional zero-field frequency spectrum [5]. An illustration of this experiment is provided in fig. 8.6*a*), where the field cycle shown employs a pulsed-field mixing period between t_1 and t_2. Magnetization able to oscillate at two possible frequencies in the two time periods, for example the ν_+ and ν_- quadrupolar frequencies of a given site, will produce an off-diagonal peak, or «cross-peak», at the intersection of these two frequencies if the mixing sequence transfers coherence between the transitions. An experimental illustration of the connectivities in a spin $I = 1$ system appears in fig. 8.6*b*) which shows the two-dimensional zero-field spectrum of the methylene region of a sample of selectively deuterated diethylterephthalate. This result shows that, among the four lines in the CD_2 region of the spectrum, lines 1 and 3 belong to one deuteron and lines 2 and 4 to the other inequivalent deuteron. *With this kind of experiment one can hope to identify sites by their quadrupole couplings and then determine intersite distances through their dipolar couplings in a two-dimensional spectrum.*

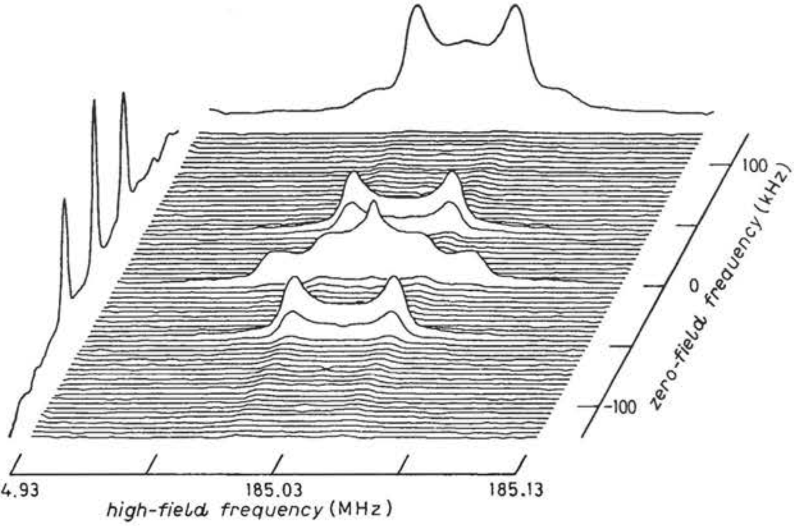

Fig. 8.7. – Two-dimensional zero-field high-field dipolar correlation spectrum of polycrystalline $Ba(ClO_3)_2 \cdot H_2O$. For each of 64 values of t_1, the zero-field interval, the high-field free-induction decay after a solid echo sequence is accumulated and stored. A double real Fourier transform in t_1 and t_2 is applied to the signal $S(t_1, t_2)$. At the left and top are the projections of the zero-field and high-field spectra and in the center the correlations between the two frequency domains. Signals which appear at zero frequency in ω_1 correlate most strongly with signals from orientations of the two-spin system which are near the edges of the high-field powder pattern. Zero-field signals which appear at ~ 42 kHz correlate the orientations which appear near the peaks (at ~ ±21 kHz) of the high-field powder pattern. (Adapted from *J. Chem. Phys.*, 83, 4877 (1985), with permission.)

A different class of two-dimensional experiments reserves zero-field evolution for the period t_1 and high-field evolution for the period t_2 in order to correlate high-field and zero-field NMR transitions. An example, shown in fig. 8.7[171] for two water protons in a polycrystalline hydrate, displays the Pake doublet powder pattern in the high-field dimension and a three-line zero-field spectrum in the other dimension. In principle, one can contemplate obtaining high-resolution chemical shifts in the high-field dimension and sharp dipolar couplings between sites in the zero-field dimension.

8·3. *Zero-field pulses.* – The discussion so far has focused on the sudden removal of an applied field to induce zero-field evolution as in fig. 8.2. This approach, however, suffers from two principal disadvantages. The first derives from the requirement that the intermediate field be larger than the local spin interactions so that the Zeeman interaction dominates. For nuclei with small magnetogyric ratios and large quadrupolar coupling constants, this condition requires that a field of a few hundred to a few thousand gauss be applied for some tens of milliseconds—perhaps a difficult task. The other disadvantage comes from the lack of selectivity in the sudden transition that excites evolution of different isotopes and spins (*e.g.*, protons, deuterium, ^{13}C) in zero field. The experiment can be made selective and more flexible, however, by a simple modification of the field cycle to use pulsed d.c. magnetic fields to excite different

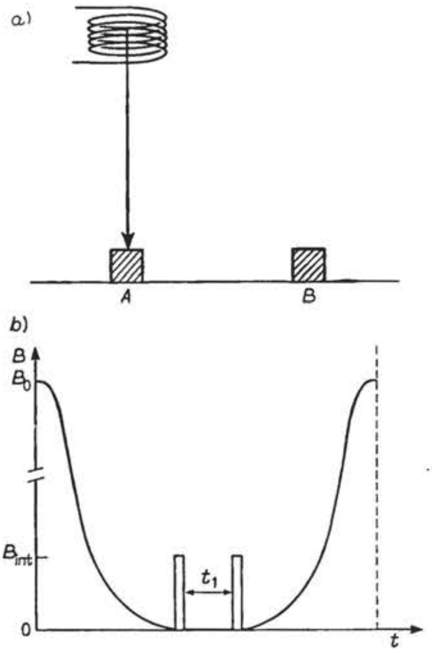

Fig. 8.8. – Pulsed-field cycling with adiabatic demagnetization and remagnetization. *a*) Demagnetized sample *A* differs from one which has resided on zero field for an extended period *B*. Both have no magnetization, but *A* will spontaneously polarize when returned to a field, while *B* requires a time on the order of the spin-lattice relaxation time, T_1, to polarize. It is this zero-field order of *A* which is exploited after demagnetizing to zero field by applying d.c. pulses (for example, $\pi/2$ zero-field pulses) to initiate evolution for the time t_1. The evolution is terminated by a second pulse and the sample is returned to high field for sampling of the magnetization. This field cycle provides flexibility in employing large fields for brief periods of time, as well as in selective excitation of different spins (*e.g.*, ^{13}C *vs.* protons), by varying the magnitude, direction and duration of the pulses and level crossings in heteronuclear spin systems. (Adapted from *J. Chem. Phys.*, 83, 934 (1985), with permission.)

nuclear spins in zero field, as illustrated in fig. 8.8[174, 177, 181]. The sample is first removed completely to zero field through adiabatic demagnetization in the laboratory frame. Application of a pulsed d.c. field at this point then changes the state of the system and induces evolution in zero field for a time t_1. This evolution may be terminated with a second d.c. pulse. The effect is analogous to pulsed NMR in high field, but here the resonant frequency, and, therefore, the frequency of the pulses, is zero. Finally, the sample is adiabatically remagnetized back to high field for normal high-field NMR detection. Different isotopes and spins can be addressed separately by making the zero-field pulses selective, perhaps by using composite pulses that produce 2π rotations for all isotopes except the one of interest.

An additional advantage of pulsed-field cycles of the sort shown in fig. 8.8 is that they permit level crossings between protons and quadrupolar spins during the adiabatic demagnetization and remagnetization. This possibility allows the zero-field evolution of a quadrupolar spin, say deuterium, to be detected by the effect on the more sensitive proton spins. Indirect detection has long been used in traditional field-cycling NQR experiments, but in the usual procedure the protons are made to absorb low-frequency zero-field irradiation directly, by which a low-frequency signal that obscures the NQR lines is produced. The time domain experiment alleviates such problems by using selective d.c. pulsed fields. An example of a ^{14}N zero-field spectrum obtained by selective pulses in zero field and indirect detection through the protons is shown for polycrys-

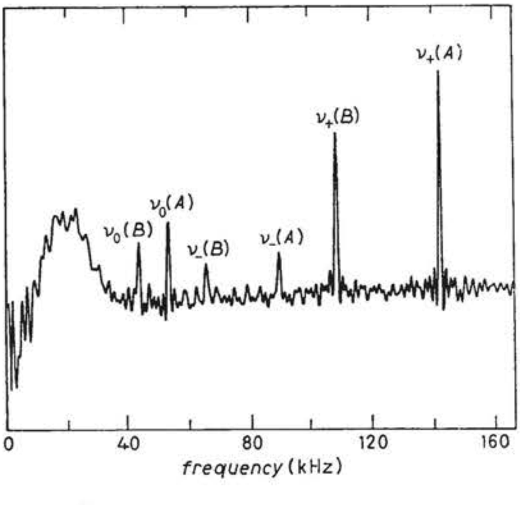

Fig. 8.9. – Pulsed zero-field ^{14}N NQR spectrum of solid $(NH_4)_2SO_4$ using the cycle in fig. 8.8 with selective 2π pulses for the protons. The ^{14}N was detected indirectly by level crossing with the protons. Peaks corresponding to two inequivalent nitrogen sites in the unit cell are labeled *A* and *B*. Residual proton signal appears below 40 kHz, but has been reduced sufficiently to allow for resolution of the low-frequency ^{14}N NQR lines. (Adapted from *J. Chem. Phys.*, 83, 934 (1985), with permission.)

talline ammonium sulfate in fig. 8.9. Such experiments on deuterium and ^{14}N are likely to be useful in the study of biological systems, which are often inherently amorphous or disordered. Recent experiments have demonstrated zero-field analogs to multiple-pulse high-field NMR, including scaling of interactions and time reversal [182-186]. For example, fig. 8.10*a*) shows the sixteen-pulse

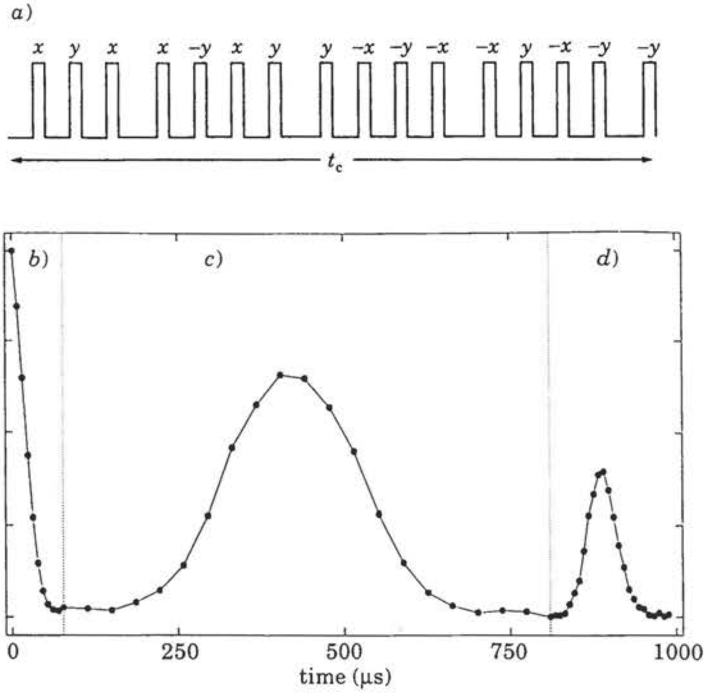

Fig. 8.10. – Isotropic spin echoes for zero-field second-rank interactions. *a*) The second-rank sixteen-pulse time-reversal sequence. (Small interpulse spacings correspond to τ delays, whilst large spacings correspond to 2τ.) *b*) The magnetization of the protons in polycrystalline adamantane decays due to the local isotropic dipole-dipole couplings. *c*) After 74 μs the isotropic time-reversal sequence is applied and the magnetization is retrieved 370 μs later, because the scaling factor is $1/5$. *d*) Free evolution in zero field is resumed at time 810 μs. One sample point is taken per cycle (36.8 μs). The pulse duration is 1 μs. (Adapted from *Phys. Rev. Lett.*, **67**, 1989 (1991), with permission.)

sequence that achieves time reversal of second-rank interactions. The sequence also isotropically scales first-rank interactions by $k = 1/5$. In this process the Hamiltonian is rotated by all of the six $\pi/2$ and the eight $3\pi/2$ rotations of the cubic group with relative weights 2 to 1 (cf. sect. 5). Figures 8.10*b*)-*d*) show the result of applying the sequence to a sample of solid adamantane, generating an echo after the zero-field free-induction decay [185].

8.4. *Calculation of the zero-field spectrum.* – It is instructive to perform a specific calculation of the zero-field signal for a simple case. Consider a molecule or group of spins in a polycrystalline or otherwise disordered sample. The laboratory-based coordinate system is denoted x, y, z as usual, with any high field B_0 along z, and molecule-based axes are labeled $x\mathrm{m}$, $y\mathrm{m}$, $z\mathrm{m}$. We denote by $R(\Omega)$ the operator, or by $\boldsymbol{R}(\Omega)$ the superoperator, that effects the transformation between laboratory and molecular frames. The transformation angles Ω are characterized by a probability distribution $P(\Omega)$ over the sample. $\Omega \equiv (\alpha, \beta)$, where α, β are the two Euler angles, the third angle γ is not required owing to cylindrical symmetry about z in high field and is accordingly set to zero.

In the molecular frame the internal Hamiltonian (dipolar, quadrupolar, etc.) is homogeneous in the sense that it is independent of Ω or position in the sample. For the simple field cycle of fig. 8.2 the initial state of the spin system is given by

$$|\rho(0)\rangle \sim |I_z\rangle, \tag{8.1}$$

and I_z is detected in high field at the end of the cycle. Thus we can use precisely the formalism of previous sections. The zero-field time domain signal (again we write t instead of t_1) is given by

$$f_\Omega(t) = \langle I_z | \boldsymbol{U}_\Omega(t) | I_z \rangle. \tag{8.2}$$

The subscript Ω reminds us that this signal is for a particular orientation of the molecule or spin system in the laboratory. $\boldsymbol{U}_\Omega(t)$ is the zero-field propagator in the laboratory frame. We then write

$$f_\Omega(t) = \langle I_z | \boldsymbol{R}(\Omega)\, \boldsymbol{U}_\mathrm{m}(t)\, \boldsymbol{R}^\dagger(\Omega) | I_z \rangle, \tag{8.3}$$

where

$$\boldsymbol{U}_\mathrm{m}(t) = \boldsymbol{R}^\dagger(\Omega)\, \boldsymbol{U}_\Omega(t)\, \boldsymbol{R}(\Omega) \tag{8.4}$$

is the homogeneous propagator in the molecular frame. $|I_z\rangle$ can easily be expressed in terms of operators in the molecular frame through the Wigner rotation matrices

$$\begin{aligned} \boldsymbol{R}(\Omega)\, I_z \boldsymbol{R}^\dagger(\Omega) &= D^{(1)}_{00}(\Omega)\, I_{z\mathrm{m}} - D^{(1)}_{00}(\Omega) \frac{1}{\sqrt{2}} I_{+\mathrm{m}} + D^{(1)}_{-10} \frac{1}{\sqrt{2}} I_{+\mathrm{m}} = \\ &= I_{z\mathrm{m}} \cos\beta - I_{x\mathrm{m}} \sin\beta \cos\alpha + I_{y\mathrm{m}} \sin\beta \sin\alpha\,. \end{aligned} \tag{8.5}$$

Inserting eq. (8.5) into eq. (8.3) we obtain

$$\begin{aligned} f_\Omega(t) = \langle I_{z\mathrm{m}} \cos\beta - I_{x\mathrm{m}} \sin\beta \cos\alpha + I_{y\mathrm{m}} \sin\beta \sin\alpha \,\cdot \\ \cdot\, | \boldsymbol{X}_\mathrm{m}(t) | I_{z\mathrm{m}} \cos\beta - I_{x\mathrm{m}} \sin\beta \cos\alpha + I_{y\mathrm{m}} \sin\beta \sin\alpha \rangle. \end{aligned} \tag{8.6}$$

8˙5. *Average over orientational distribution.* – Expression (8.6) must now be averaged over the distribution $P(\Omega)$ to give the signal for the sample

$$f(t) = \int f_\Omega(t)\, P(\Omega)\, \mathrm{d}\Omega \,. \tag{8.7}$$

For an isotropic three-dimensional distribution, as in a random powder, all Ω are equally probable, *i.e.*

$$P(\Omega) = \text{const}\,, \tag{8.8}$$

and only three terms in (8.6) survive the integration of (8.7). The result is

$$f(t) = \frac{1}{3}\left(\langle I_{x\mathrm{m}} | \boldsymbol{U}_\mathrm{m}(t) | I_{x\mathrm{m}}\rangle + \langle I_{y\mathrm{m}} | \boldsymbol{U}_\mathrm{m}(t) | I_{y\mathrm{m}}\rangle + \langle I_{z\mathrm{m}} | \boldsymbol{U}_\mathrm{m}(t) | I_{z\mathrm{m}}\rangle\right). \tag{8.9}$$

Expanding (8.9) in an eigenbasis of $\boldsymbol{U}_\mathrm{m}(t)$ in the manner of sect. **1**, we obtain the final expression

$$f(t) = \frac{1}{3} \sum_{jk} \left(|I_{x\mathrm{m}jk}|^2 + |I_{y\mathrm{m}jk}|^2 + |I_{z\mathrm{m}jk}|^2\right) \cos \omega_{jk} t\,, \tag{8.10}$$

where $I_{x\mathrm{m}jk}$ is the (j, k)-th matrix element of $I_{x\mathrm{m}}$. This expression implies that the signal will be linearly polarized along z, and that the Fourier transform spectrum is symmetric around zero frequency. This behavior is expected, of course, because of the axial symmetry around z manifested by eq. (8.8).

8˙6. *Dipolar coupled spin $I = 1/2$ pair or quadrupolar spin $I = 1$.* – We can now evaluate (8.10) explicitly for the most basic cases of zero-field NMR and NQR. Consider two spins $I = 1/2$ with an axially symmetric dipolar coupling. With the molecular z axis along the symmetry axis established by the internuclear vector the molecular-frame Hamiltonian in frequency units is

$$H_{\mathrm{Dm}} = \omega_\mathrm{D}(3 I_{z\mathrm{m}1} I_{z\mathrm{m}2} - \boldsymbol{I}_1 \cdot \boldsymbol{I}_2)\,, \tag{8.11}$$

where the dipolar frequency ω_D is

$$\omega_\mathrm{D} = \gamma^2 / r^3\,. \tag{8.12}$$

The well-known eigenstates of eq. (8.11) are depicted in fig. 8.11*a*): a triplet 1, 2, 3 (with a degenerate pair 1, 2) and a singlet S. The only nonzero matrix elements in eq. (8.10) are within the triplet manifold. The frequencies are

$$\begin{cases} \omega_{12} = 0\,, \\ \omega_{13} = \omega_{23} = \dfrac{3}{2}\omega_\mathrm{D}\,. \end{cases} \tag{8.13}$$

Plugging all this into (8.10) and recalling that we are working with a normalized signal $\langle I_z | I_z \rangle = 1$, as in sect. **1**, we obtain

$$f(t) = \frac{1}{3}\left(1 + 2\cos\frac{3}{2}\omega_\mathrm{D} t\right), \tag{8.14}$$

which predicts a spectrum of lines with equal intensities at 0 and $\pm 3\omega_D/2$, as shown in the lower part of fig. 8.11*a*). Such a spectrum is indeed observed experimentally for a pair of protons, as we saw previously in fig. 8.7. Figure 8.11*b*) reminds us that the situation is entirely analogous to a single spin $I = 1$ (cf. the three-level system of subsect. **1˙13**) if $\eta = 0$. Remember, however, that here we are in the molecular frame for all Ω. The triplet manifold is analogous to that of the dipolar coupled pair and there is no singlet state.

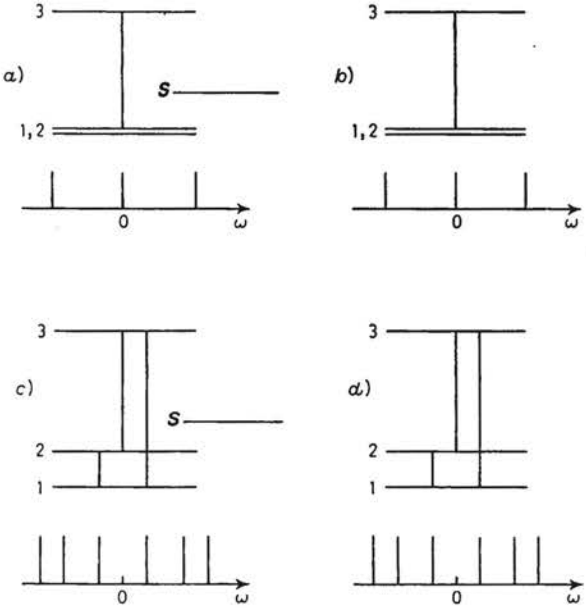

Fig. 8.11. – Energy levels and schematic spectra of two spins $I = 1/2$ and for a spin $I = 1$ in zero field for $\eta = 0$ and for $\eta \neq 0$. Small deviations from local symmetry, or subtle motional effects, lead to small values of η which are easily observable in zero field.

For both the dipolar coupled pair and the single spin $I = 1$, where the asymmetry parameter η is nonzero, the zero-field transitions are split as shown in fig. 8.11*c*) and *d*). The molecular-frame Hamiltonian for the dipolar case is

$$H_{\mathrm{Dm}} = \omega_{\mathrm{D}}[3I_{z\mathrm{m}1}I_{z\mathrm{m}2} - \boldsymbol{I}_1\cdot\boldsymbol{I}_2 + \eta(I_{x\mathrm{m}1}I_{x\mathrm{m}2} - I_{y\mathrm{m}1}I_{y\mathrm{m}2})]\,, \tag{8.15}$$

which splits the ω_{12} transition,

$$\omega_{12} = \eta\omega_{\mathrm{D}}\,. \tag{8.16}$$

For the quadrupolar case, the Hamiltonian is

$$H_{\mathrm{Qm}} = A[3I_{z\mathrm{m}}^2 - \boldsymbol{I}^2 + \eta(I_{x\mathrm{m}}^2 - I_{y\mathrm{m}}^2)]\,, \tag{8.17}$$

with the quadrupole coupling constant

$$A = \frac{e^2 qQ}{4} . \tag{8.18}$$

Thus *the effects of small asymmetry are clearly visible as sharp splittings in the spectrum, although similar effects may be difficult to discern in high-field powder patterns.* This agreeable feature of zero-field NMR was mentioned in subsect. 8·1 and was quite clear in the experimental spectra of fig. 8.4 and 8.5. Consequently, zero-field NMR spectra may provide a useful measure of small-amplitude motions and subtle deviations from local symmetry in disordered systems. Examples of these effects, for example in biaxial smectic phases, have appeared in the literature and might prove useful for biological applications in the future.

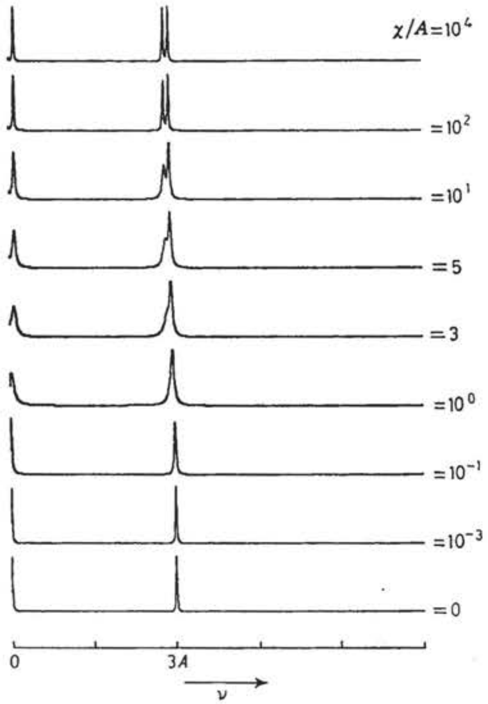

Fig. 8.12. – Simulated zero-field spectra for jumps of symmetry axis of a deuterium spin with $\eta = 0$ between orientations differing by $2\theta = 20°$. Only the positive-frequency halves of the spectra are shown. χ/A, the ratio of the exchange rate to the quadrupolar frequency, varies from the rigid regime (bottom) to the rapid motional limit (top). The ratio of the residual line broadening $(1/T_2)$ to the quadrupolar frequency is 0.02. The onset of line splitting due to the motionally induced asymmetry ($\eta \neq 0$) can be seen at large χ/A. The behavior would be similar for the zero-field NMR of two coupled spins $I = 1/2$. (Adapted from *J. Chem. Phys.*, 85, 4873 (1986), with permission.)

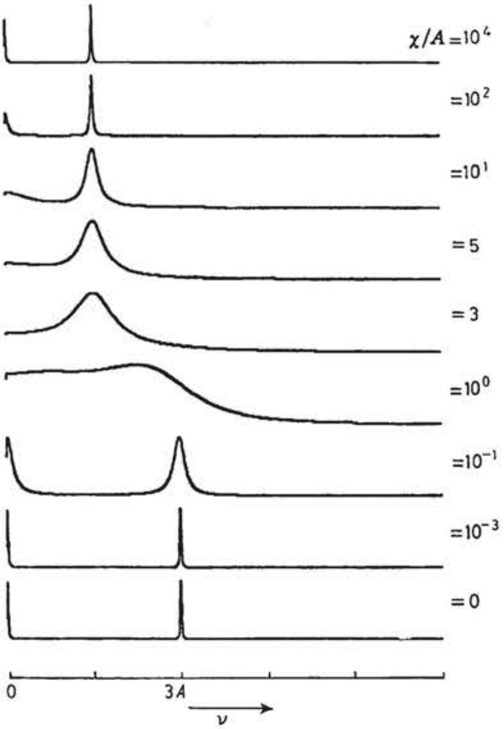

Fig. 8.13. – Same as fig. 8.12 but $2\theta = 90°$. This motion is equivalent to fourfold jumps around an axis, and, therefore, leads to an axially symmetric motionally averaged spectrum. (Adapted from *J. Chem. Phys.*, **85**, 4873 (1986), with permission.)

8'7. *Effects of motion.* – As an example of the effect of introducing a small nonzero asymmetry parameter through motion, consider an axially symmetric dipolar- or quadrupolar-coupling tensor where the symmetry axis jumps randomly through an angle of 2θ. When the jump rate χ increases from zero, the zero-field spectrum should change from the static (axially symmetric) case to the time-averaged case, in analogy to high-field NMR studies of chemical exchange and motion (recall sect. 5) [187].

Examples of spectra simulated for a quadrupolar spin and different relative jump rates (χ/A) are shown in fig. 8.12 for $2\theta = 20°$ and in fig. 8.13 for $2\theta = 90°$; the jumps are equivalent to fourfold jumps around an axis (due to the symmetry of the Hamiltonian under 180° rotations) leading to a time-averaged axially symmetric coupling.

An interesting experimental example of the onset of asymmetry in dipolar couplings occurs in the smectic liquid crystals as shown in fig. 8.14 [188]. The smectic A and B phases are locally uniaxial, and, indeed, the zero-field NMR spectra of methylene chloride (CH_2Cl_2) probe molecules dissolved in these phases display peaks characteristic of axial symmetry. In the smectic E phase,

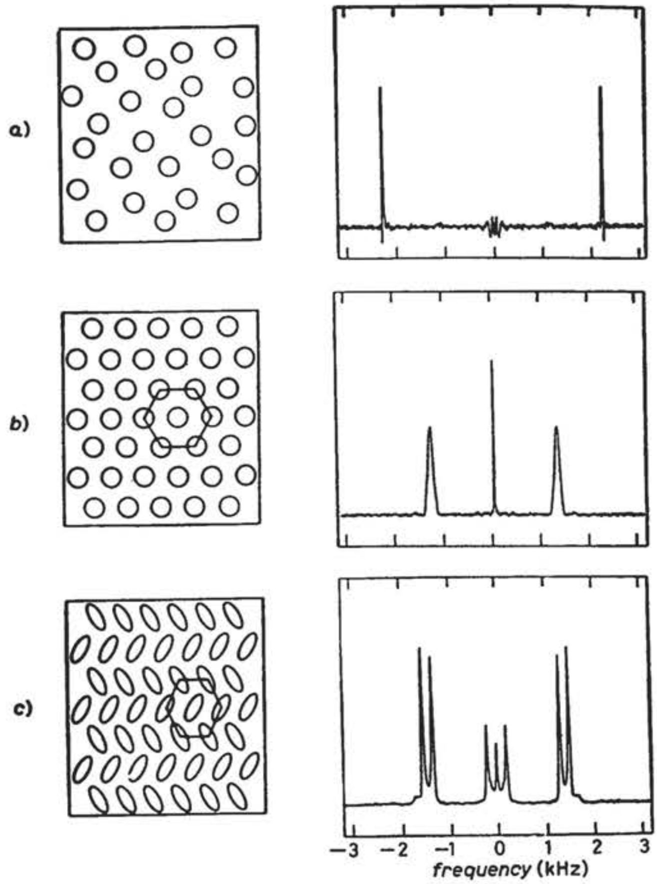

Fig. 8.14. – Zero-field NMR spectra of the proton pairs in methylene chloride (CH_2Cl_2) probe molecules dissolved in smectic *a)* *A*, *b)* *B* and *c)* *E* phases of liquid crystals. The smectic *E* sample exhibits a line splitting characteristic of an asymmetric dipolar coupling, a consequence of the biaxial environment. (Courtesy of M. LUZAR.)

on the other hand, the line splittings reflect an asymmetry in the dipolar-coupling tensor of the proton spin pair induced by the biaxial environment on the smectic layers. It is useful that such subtle asymmetries can be seen directly in powder samples. Similar effects have been seen in solid carboxylic-acid dimers which exhibit correlated proton jumps in the hydrogen bonds.

8·8. *Magnetic resonance with a* SQUID *detector*. – A recent alternative to magnetic-field cycling is the detection of zero-field and low-frequency spectra using a dc-SQUID (superconducting quantum interference device) detector. Following an early rf-SQUID design by DAY [189], the SQUID has been incorporated into both pulsed- and continuous-wave spectrometers by coupling the nuclear magnetic flux in the sample to the SQUID through a superconducting

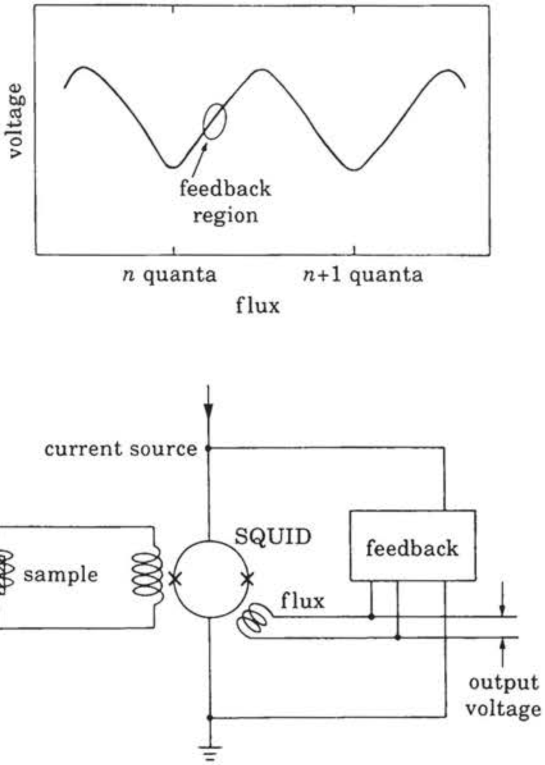

Fig. 8.15. – Schematic representation of a SQUID NMR spectrometer. (Adapted from *Rev. Sci. Instrum.*, **61**, 1059 (1990), with permission.)

transformer as shown in fig. 8.15 [190, 191]. The SQUID spectrometers are quite sensitive and they have been used to detect low-frequency nuclear quadrupole resonances of deuterium, nitrogen-14, boron-10, 11 and aluminum-27 in crystals and glasses, and NMR transitions arising from quantum tunneling of methyl groups at low magnetic field and low temperature shown in fig. 8.16 [191]. Recently a pulsed SQUID spectrometer has been built and used to obtain ^{14}N NQR spectra showing the effects of quantum tunneling of ammonium groups [192].

8·9. *Comment on relationship of spatially selective pulses to zero-field* NMR. – We would like to make a brief comment on the connection between spatial selectivity with a surface coil and the seemingly unrelated area of zero-field NMR. In normal high-field NMR we are accustomed to exciting and detecting different spins (*e.g.*, ^{1}H, ^{13}C, ...) separately and selectively according to their different frequencies. If we wish to work with protons, we may use 400 MHz, for example, and for ^{13}C we would then use 100 MHz. In zero field, however, all

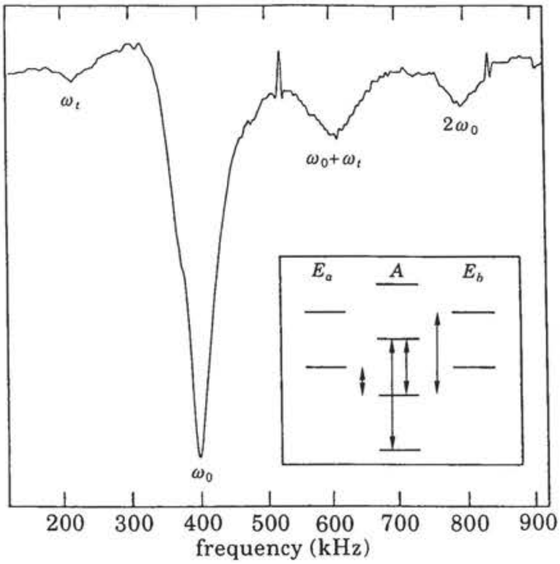

Fig. 8.16. – NMR spectrum arising from quantum tunneling of methyl groups at low magnetic field and low temperature obtained using a SQUID spectrometer. (Adapted from *Rev. Sci. Instrum.*, **61**, 1059 (1990), with permission.)

basic resonance frequencies are zero. So how do we differentiate between different species? The answer is that we use the magnetogyric ratio which is analogous to the r.f. amplitude ω_1 in high-field NMR. If we apply d.c. pulses, the spins respond differently according to their magnetogyric ratios. But is this notion not identical to the idea of spatial selectivity using a surface coil with composite pulses in high-field NMR? The two tubes shown in fig. 1.29 experience different ω_1 fields and this distinction is what is often used to label such regions. Indeed, some of this work in spatial selectivity has been useful in zero-field NMR.

9. – Geometric phases.

9·1. *Context for geometric phases.* – Nuclear spins provide an ideal arena for the demonstration of a class of phenomena related to the so-called geometric phases [193-197], of which Berry's phase is an important example. The general context for the geometric phase arises from the division of a system into two parts, characterized by coordinates or variables that we shall refer to as external and internal. For example, in the case of a classical object, the external coordinates might be the position of the object, and the internal coordinates might describe its orientation. For a quantum spin, the external coordinates might be the direction of the spin and an internal coordinate might be the phase of the wave function. For a Born-Oppenheimer molecule the external coordinates might be the nuclear coordinates, and the internal coordinates would refer to the electronic wave function.

The separation of the system naturally gives rise to a gauge ambiguity, namely the fact that, for each point of the external-coordinate space, it is possible to choose a coordinate system or reference frame for the internal coordinates, *a choice of gauge*, in different (often an infinite number of) ways. But our observations must be invariant to the choice of gauge, a statement of *gauge symmetry* [198, 199]. Now, a common and important question is, what is the change, the *holonomy*, in the internal variables, when the system undergoes a cyclic evolution in the space of its external coordinates, as shown in fig. 9.1.

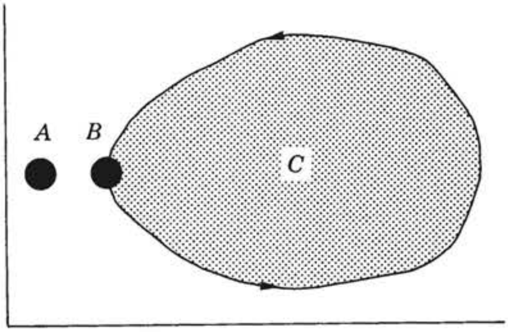

Fig. 9.1. – If a system is characterized by internal and external coordinates, then a change of the internal variables may occur when the system undergoes a cyclic evolution in the external coordinates. For example, if the two twins A and B are initially in the same state and B is taken on a circuit in its external coordinates, the holonomy, or change of internal coordinates of B, can be determined by comparing it with A.

The holonomy (of which the geometric phase is an example) could, of course, be calculated by direct solution (often cumbersome integration) of the appropriate equations of motion, for example the Schrödinger equation. The fact that we can often do better by recognizing the role of geometry and topology is a consequence of gauge symmetry. It is the appreciation of the broad and unifying implications of gauge symmetry that constitutes the basis for the remarkable contributions of Berry's phase and its generalizations. In this section we describe some examples of geometric phases with a view to demonstrating the unification of a diverse range of phenomena, including the phases of spins and of light, the Aharanov-Bohm effect [200, 201], fractional quantum numbers of Jahn-Teller molecules [202-204] and the reorientational kinematics of cats [205-207].

9·2. *Classical holonomy.* – Consider the situation depicted in fig. 9.2; a particle changes its position on the surface of a sphere (the external coordinates)

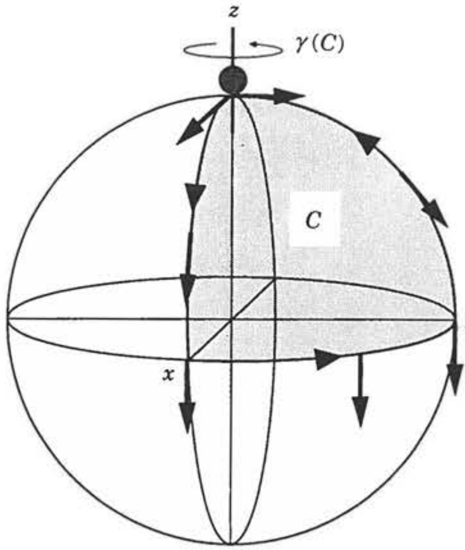

Fig. 9.2. – A simple example of holonomy is obtained by transporting a particle on the surface of a sphere. The direction in which the particle points is indicated by a tangent vector. If the particle is moved around the circuit C in such a way that it maintains a constant angle with the tangent to the path, this corresponds to parallel transport. Upon its return to the north pole, the particle has rotated by an amount $\gamma(C)$, the angle holonomy.

under *parallel transport* [208], namely in such a way that the particle does not rotate locally about its axis, the axis perpendicular to the sphere surface. The orientation of the particle about its axis (the internal coordinate) is indicated by a tangent vector. Under parallel transport on a flat surface, the orientation of the particle would not change; the tangent vector would remain parallel to itself at all times. However, the surface of the sphere is curved, which makes it possible for the orientation of the particle to change under parallel transport. In fact, if the particle undergoes the cyclic trajectory shown in fig. 9.2, starting and ending at the north pole, its orientation changes by [199]

$$\gamma = -\Omega(C), \tag{9.1}$$

where $\Omega(C)$ is the solid angle subtended by the circuit at the origin of the sphere (the area enclosed by the circuit on the surface of a unit sphere), in this case $\pi/2$. This accumulated global rotation, even though there is no local rotation, is a geometric angle, an example of an *angle holonomy*. A famous example of such a classical holonomy is the rotation of the plane of a Foucault pendulum [209] as the Earth rotates.

9·3. *Quantum holonomy.* – The classical angle holonomy derives from the curvature of the sphere, a consequence of its nontrivial topology. Similarly, in

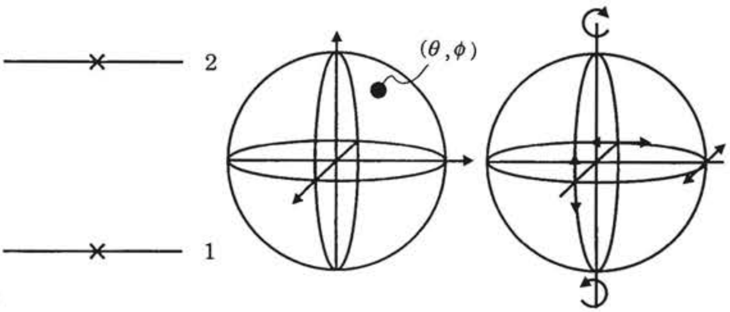

two-level system polarization sphere Poincaré sphere

Fig. 9.3. – Representations of two-level systems. A two-level system can be described by θ and ϕ, the external coordinates indicating the direction of the spin, and φ, the internal coordinate indicating the overall phase. The external coordinates define the surface of a sphere. For a spin $I = 1/2$ the poles correspond to «spin up» and «spin down» z polarizations and the equator represents linear combinations of x and y polarizations. On the sphere of light polarization (the Poincaré sphere (right)) the poles correspond to the two helicity states (circular polarization) and the equator describes states of linear polarization with plane angles from 0° to 180°.

quantum mechanics, the state space of the system may also possess a nontrivial topology. In fact, consider one of the simplest quantum systems, a two-level system, for example the states of a spin $I = 1/2$, or the polarization states of a photon (fig. 9.3). Recalling sect. 4, and following FEYNMAN *et al.* [109, 111, 210], the state of any two-level system can be described by two coordinates indicating the direction of the spin or fictitious spin, and a third coordinate indicating the overall phase of the wave function. Thus any wave function can be written as a product

$$|\psi\rangle = \exp[i\varphi]\,|\tilde{\psi}(\theta, \phi)\rangle, \tag{9.2}$$

where θ and ϕ, the external coordinates, define the surface of a sphere, the polarization sphere (known, for light polarization, as the Poincaré sphere) and φ, the phase, is the internal coordinate. The $|\tilde{\psi}\rangle$ constitute a basis or projective space, the space of spin or polarization states without regard to phase. The choice of $|\tilde{\psi}\rangle$ implies a reference phase for φ, namely a choice of gauge, under changes of which

$$|\tilde{\psi}(\theta, \phi)\rangle \rightarrow \exp[if(\theta, \phi)]\,|\tilde{\psi}(\theta, \phi)\rangle \tag{9.3}$$

any observables must be invariant.

Suppose now that, in analogy to the case of classical holonomy in subsect. **9**˙2, the spin begins at the north pole (along z), and undergoes the cyclic trajectory of fig. 9.4 (pointing successively along x, y and z), returning to the initial state along z. Such an evolution can be accomplished in a variety of ways

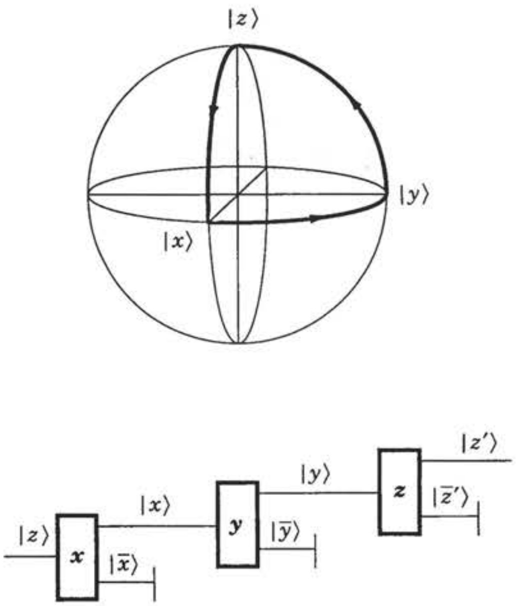

Fig. 9.4. – Quantum (Abelian) holonomy manifests itself as a change in the phase of the wave function when the system undergoes a circuit, in this case on the sphere of polarizations of a spin $I = 1/2$ passing through a series of differently oriented Stern-Gerlach devices.

(for example, by adiabatic following of a magnetic field whose direction changes slowly in a circuit, the situation considered by BERRY[193]). Since the initial and final spin directions are the same, the initial and final wave functions must be the same up to a phase factor:

$$|\psi\rangle_{\text{final}} = \exp[i\varphi]\,|\psi\rangle_{\text{initial}}\,. \tag{9.4}$$

As we show in the next subsection, in addition to the familiar exp $[i\omega t]$ type phase factor (total local phase accumulation)

$$|\psi(t)\rangle = \exp[i\omega t]\,|\psi(0)\rangle\,, \tag{9.5}$$

there is a geometric contribution to the phase, arising from parallel transport of the spin state on the curved surface. The geometric part of the phase factor, γ, the *phase holonomy* (the phase change that would be obtained under parallel transport of the spin),

$$|\psi\rangle \xrightarrow{C} \exp[i\gamma(C)]\,|\psi\rangle\,, \tag{9.6}$$

is given in analogy to eq. (9.1) by

$$\gamma = -m\Omega(C)\,, \tag{9.7}$$

where the solid angle is *multiplied by the spin quantum number m*, in this case ±1/2.

9·4. *Equations for the geometric phase.* – In a specific gauge $\{|\tilde{\psi}\rangle\}$, consider a state

$$|\psi\rangle = \exp[i\varphi]|\tilde{\psi}\rangle . \tag{9.8}$$

Differentiation gives

$$\frac{\mathrm{d}}{\mathrm{d}t}|\psi\rangle = i\frac{\mathrm{d}\varphi}{\mathrm{d}t}|\tilde{\psi}\rangle + \exp[i\varphi]\frac{\mathrm{d}}{\mathrm{d}t}|\tilde{\psi}\rangle , \tag{9.9}$$

and from the Schrödinger equation

$$\frac{\mathrm{d}}{\mathrm{d}t}|\psi\rangle = \frac{-i}{\hbar}H|\psi\rangle . \tag{9.10}$$

Combining eqs. (9.9) and (9.10), followed by multiplication by $\langle\psi|$ and using the fact that $\langle\psi|\psi\rangle = 1$, we arrive at an equation for the evolution of the phase factor:

$$\mathrm{d}\varphi = \frac{1}{\hbar}\langle\psi|H|\psi\rangle\,\mathrm{d}t - i\langle\tilde{\psi}|\mathrm{d}\tilde{\psi}\rangle . \tag{9.11}$$

The first term in this expression corresponds to the local rotation (phase accumulation) due to the eigenvalue of H, the familiar exp $[i\omega t]$ term whose integral around a circuit is

$$\oint \frac{1}{\hbar}\langle\psi|H|\psi\rangle\,\mathrm{d}t = \overline{\omega}t , \tag{9.12}$$

where $\overline{\omega}$ is the average eigenvalue of H over the circuit and serves as a clock for the trajectory. The second term, on the other hand, corresponds to the geometric contribution to the overall phase

$$\gamma = -i\oint\langle\tilde{\psi}|\mathrm{d}\tilde{\psi}\rangle = \oint A . \tag{9.13}$$

$A = -i\langle\tilde{\psi}|\mathrm{d}\tilde{\psi}\rangle$ is a connection [199] (it contains differentially the connections between the $|\tilde{\psi}\rangle$ of the base space, namely the phase factors that define this particular choice of gauge), which behaves exactly like a gauge potential. The geometric phase can be evaluated using Stokes theorem for the integration around a circuit C on a surface s,

$$\oint_C A = \int_s \mathrm{d}A , \tag{9.14}$$

where dA is the curvature of the surface. Figure 9.5 illustrates the circuit of $|\tilde{\psi}\rangle$ and the accompanying circuit of $|\psi\rangle$ with the associated holonomy φ. The values

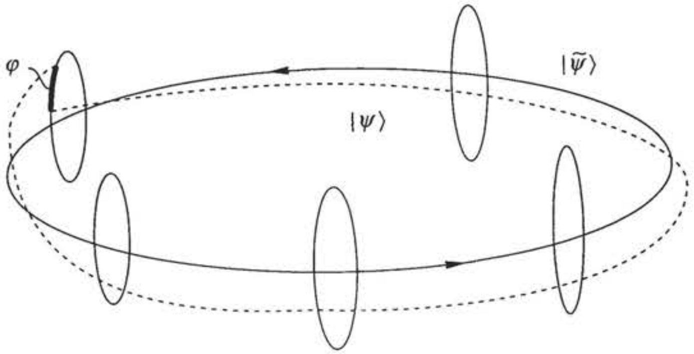

Fig. 9.5. – A circuit in the base space $|\tilde{\psi}\rangle$ and the corresponding circuit of $|\psi\rangle$. At each value of the external coordinate (for each $|\tilde{\psi}\rangle$), the $|\psi\rangle$'s corresponding to different values of the internal coordinates are related to each other by a gauge transformation, eq. (9.8). Since values of the internal coordinates range from 0 to 2π, they are depicted as circles.

of φ range from 0 to 2π and are, therefore, depicted as circles. This construction is the simplest example of a fiber bundle [194], with a fiber circle depicting the internal coordinates (the phase) corresponding to each value of the external coordinates for the base space of $|\tilde{\psi}\rangle$ states. A gauge transformation corresponds to threading the fibers with a different set of $|\tilde{\psi}\rangle$

$$|\tilde{\psi}(s(\theta,\,\phi))\rangle \rightarrow \exp\left[if(s(\theta,\,\phi))\right]|\tilde{\psi}(s(\theta,\,\phi))\rangle\,, \tag{9.15}$$

where $s(\theta,\,\phi)$ represents the coordinates in the base space. The geometric phase of eq. (9.13) is now given by

$$\gamma' = -i\oint\langle\tilde{\psi}\exp[-if(s)]|\,\mathrm{d}(\exp[-if(s)]\tilde{\psi})\rangle\,\mathrm{d}s\,. \tag{9.16}$$

Integration by parts from 0 to T leads to

$$\gamma' = -i\oint\langle\tilde{\psi}\,|\,\mathrm{d}\tilde{\psi}\rangle\,\mathrm{d}s + \langle\tilde{\psi}\,|\tilde{\psi}\rangle(f(T)-f(0))\,, \tag{9.17}$$

so, as expected, γ is gauge invariant since $|\tilde{\psi}\rangle$ is single valued.

The case we have described above refers to an Abelian holonomy (the geometric phase is a single real number). However, geometric phases are not limited to be Abelian, and in general the holonomy may be represented by a transformation matrix of higher dimension operating on the vector $|\psi\rangle$ [197, 211-213]

$$|\psi\rangle \xrightarrow{C} \exp[i\boldsymbol{R}]|\psi\rangle\,. \tag{9.18}$$

9·5. *Explicit calculation for spin* $I=1/2$. – As a base space for spin $I=1/2$, we use the two-component spinors with a choice of gauge corresponding to [214, 215]

$$|\bar{\Psi}\rangle_+ = \begin{pmatrix} \cos\dfrac{\theta}{2}\exp[i\phi] \\ \sin\dfrac{\theta}{2} \end{pmatrix}. \tag{9.19}$$

Note that this gauge is ill defined at $\theta = \pi$, and is, therefore, termed the south-pole gauge; it does not represent an appropriate choice for circuits that pass through the south pole. We can evaluate the gauge potential, eq. (9.13):

$$A = -i\langle\bar{\Psi}\,|\,\mathrm{d}\bar{\Psi}\rangle = -i\left(\cos\frac{\theta}{2}\exp[-i\phi],\ \sin\frac{\theta}{2}\right)\mathrm{d}\begin{pmatrix} \cos\dfrac{\theta}{2}\exp[i\phi] \\ \sin\dfrac{\theta}{2} \end{pmatrix}, \tag{9.20}$$

$$A = \frac{1}{2}(1+\cos\theta)\,\mathrm{d}\phi\,. \tag{9.21}$$

This is precisely the gauge potential of a magnetic monopole of charge $m = 1/2$, a point to which we shall return shortly. The geometric phase can now be evaluated using Stokes theorem (eq. (9.14)) and eq. (9.13) to yield

$$\gamma = -\frac{1}{2}\int_S \sin\theta\,\mathrm{d}\theta\wedge\mathrm{d}\phi = -\frac{1}{2}\Omega(C)\,, \tag{9.22}$$

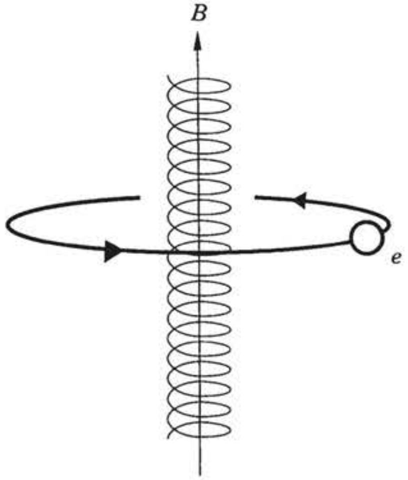

Fig. 9.6.– The Aharonov-Bohm effect involves the change in phase of the wave function of a charged particle transported in a circuit around an (infinitely long) solenoid. Even though there are no forces on the particle, because the magnetic field is zero outside the solenoid, the interaction of the particle charge with the (nonvanishing) electromagnetic gauge potential outside the solenoid gives rise to a phase shift of the particle wave function. The Aharonov-Bohm phase is an example of a geometric phase.

which justifies eq. (9.7) for $m = 1/2$. For a spin I in state m, expression (9.7) is generally valid.

9·6. *The Aharonov-Bohm effect.* – BERRY recognized that what is embodied in expressions (9.8)-(9.18), namely that the geometric phase is the integral of the gauge potential around the circuit, is reminiscent of the phase shift in the famous Aharanov-Bohm effect [109, 200], depicted schematically in fig. 9.6. A

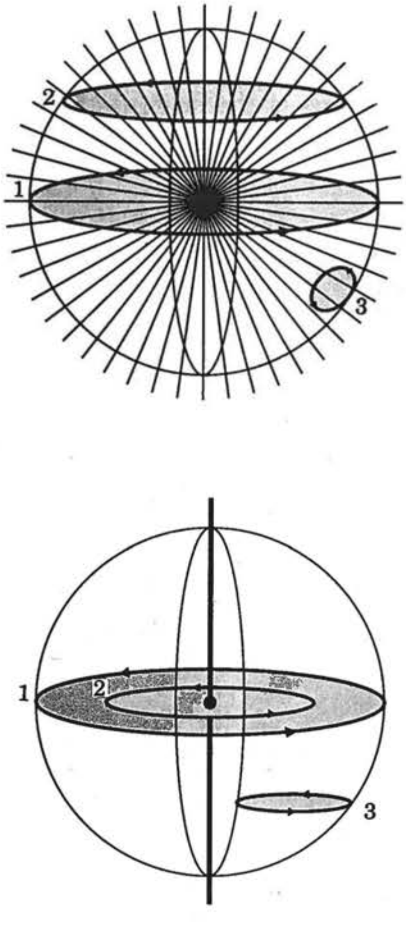

Fig. 9.7. – For a Dirac monopole of strength $m = 1/2$ with flux lines emanating isotropically, a 2π circuit (circle 1) has a geometric phase of $-\pi$ giving rise to the spinor sign change. In the upper figure the phase is proportional to the amount of flux that passes through the circuit $\gamma(C) = -(1/2)\Omega(C)$. The lower picture corresponds to gathering together the lines of flux emanating from the monopole above and below the plane into a flux tube of strength $m = 1/2$. In this case the phase is $\gamma(C) = -(1/2)2\pi = -\pi$ if the circuit encompasses the tube, circles 1 and 2, and $\gamma(C) = 0$ if the circuit does not include the tube, circle 3. (Courtesy of K. T. MUELLER.)

particle of electric charge e is transported in a circuit around an infinitely long solenoid inside which there is magnetic flux m and outside which the electromagnetic field vanishes. Classically, there are no forces on the particle, so there should be no effects due to the solenoid. However, in quantum mechanics, we must consider the electromagnetic gauge (vector) potential A, which does not vanish outside the solenoid (it is only the field, the curl $\mathrm{d}A$ of the potential, that vanishes). The interaction of the particle charge gives rise to a quantum phase shift of the particle wave function given by

$$\gamma = \oint_C A\,,$$

which is proportional to the flux of the magnetic field through the circuit and the particle charge,

$$\gamma = -m2\pi e\,. \tag{9.23}$$

The relationship to the geometric phase can now be made clear by considering the transport of a particle of unit charge in the vicinity of a Dirac monopole [214-216] of strength m, as depicted in fig. 9.7. The phase shift is again given by the integral of the potential around the circuit which is equal to the flux of the (isotropic) magnetic field through the circuit

$$\gamma = \oint_C A = -m\Omega(C)\,,$$

which is precisely the same as eq. (9.7) for $e = 1$. *Thus the geometric phase for a spin looks exactly like the Aharonov-Bohm effect for the circuit of a charged particle near a magnetic monopole.* The curvature of the spin state space is analogous to the magnetic field, and it is the flux of the curvature or field through the circuit that is responsible for the holonomy or geometric phase.

9·7. *Geometric phase in* NMR *interferometry*. – In order to measure the geometric phase in a two-level system, an additional level is required, to provide the phase reference (the twin or copy of fig. 9.1). The simplest system that can be used is a three-level system. For example, in the experiment of fig. 9.8 the holonomy of a circuit C in the 1-2 two-level system appears as a phase shift in the spin echo of a coherent superposition in the 2-3 system [217, 218]. Once again the geometric phase observed in this experiment is given by eq. (9.7). As we mentioned above, the circuit in the 1-2 system is not limited to be adiabatic, it can be nonadiabatic or even nonunitary (see subsect. 9·9), as long as we know what the circuit is. If the trajectory is not a closed circuit, we can complete it with a geodesic line, which does not affect the resulting geometric phase. Once again we may note some special cases (illustrated with the results shown in fig. 9.9). If the 1-2 transition undergoes a circuit with area 2π, we obtain from

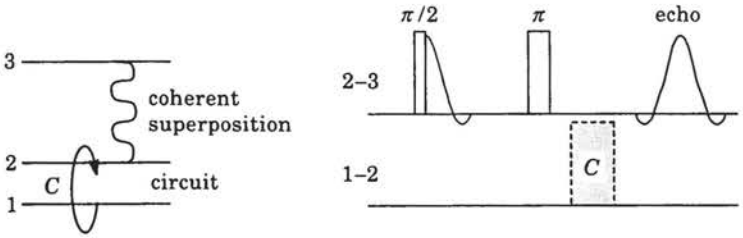

Fig. 9.8. – In NMR interferometry the holonomy of a circuit C in the 1-2 two-level system appears as a phase shift in the spin echo of a coherent superposition in the 2-3 system. (Courtesy of D. SUTER.)

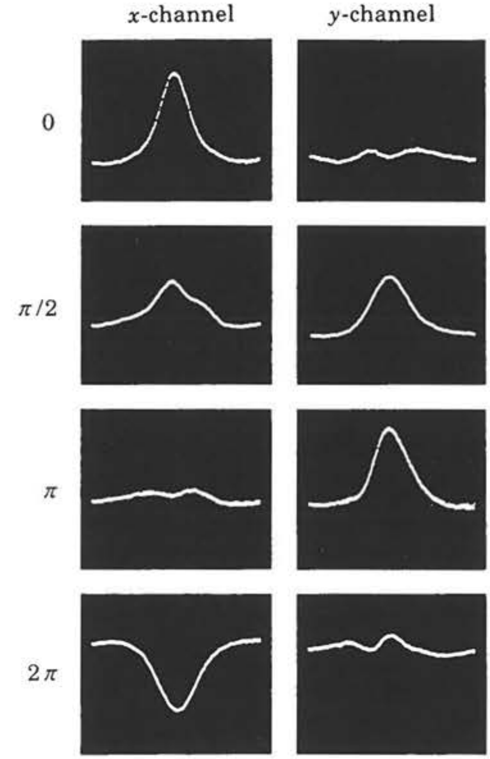

Fig. 9.9. – Holonomy in a two-level system (fig. 9.3) observed in the phase shift of a spin echo. The NMR echo is detected in orthogonal channels of a phase-sensitive detector. The numbers to the left indicate the solid angle of a circuit on the sphere of polarizations for the 1-2 subsystem. The echo arising in the 2-3 superposition moves from one channel to the other as the geometric phase increases from 0° to 90°. (Adapted from *Phys. Rev. Lett.*, **57**, 242 (1986).)

eq. (9.6), for $\exp[-i\gamma(C)] = -1$,

$$|\psi\rangle \xrightarrow{C} -|\psi\rangle, \tag{9.24}$$

which is the well-known spinor sign change; one would need a circuit with an area of 4π for the 1-2 transition to leave the system unchanged. *In fact, we see that the famous spinor sign change is just a special case of the geometric phase for a circuit with area* 2π. Similarly, if the 1-2 spin system undergoes a circuit with area π, we obtain

$$|\psi\rangle \xrightarrow{C} i|\psi\rangle \tag{9.25}$$

and the signal is shifted into the imaginary channel of the phase-sensitive detector.

9·8. *Fractional quantum numbers.* – As shown in fig. 9.10, the molecule Na_3 undergoes a Jahn-Teller distortion in which the electronic degeneracy (corresponding to the molecular symmetry E representation of the electronic wave functions) is lifted by vibronic interaction with the vibrational degeneracy (corresponding to the e representation of the nuclear wave functions). This is entirely analogous to the lifting of a spin-1/2 degeneracy in the presence of a magnetic field [197, 204]. The distorted triangle can undergo an isoenergetic pseu-

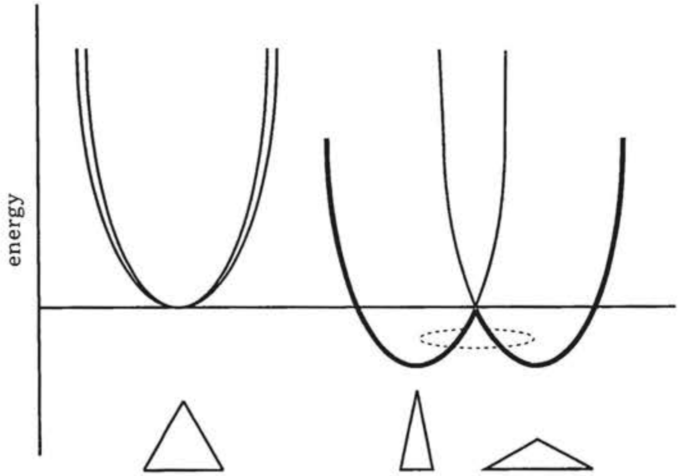

Fig. 9.10. – Born-Oppenheimer potentials for the Jahn-Teller $E \otimes e$ system, shown by taking a slice through the axially symmetric surfaces. Energy is plotted as a function of displacements in the degenerate nuclear vibration. On the left are the surfaces with no vibronic interaction; the degeneracy of these surfaces is lifted, as shown on the right, at all but a single point. The two surfaces diverge linearly from one another at the origin (the point of electronic degeneracy), with the lower surface showing stabilization for certain distorted geometries. The conical intersection at the degeneracy is the source of the geometric phase for the evolution of adiabatic states. (Adapted from *Annu. Rev. Phys. Chem.*, **41**, 601 (1990).)

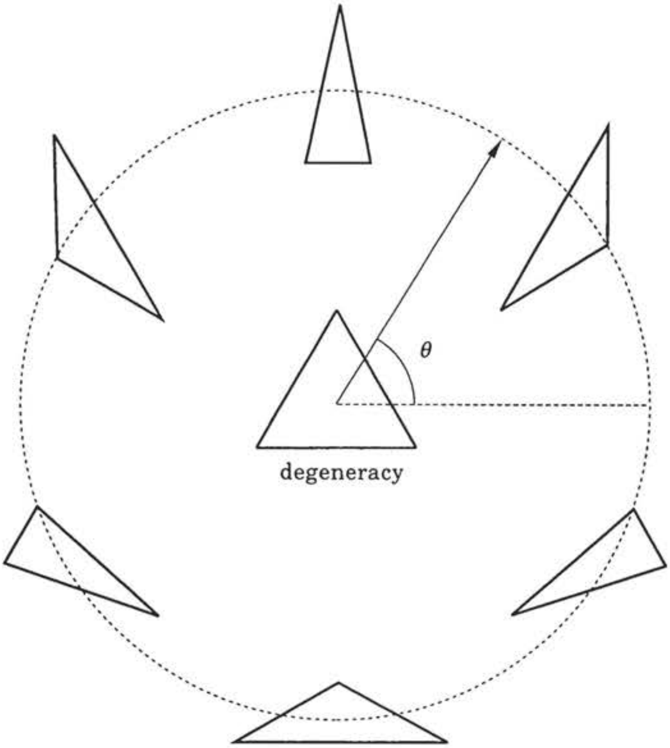

Fig. 9.11. – Pseudorotation in a trimer. The electronic degeneracy occurs at the symmetric configuration, shown as the equilateral triangle in the center. The lower-energy shapes are distorted triangles. Low-lying vibronic states are transported around the degeneracy by the pseudorotation, which results in a closed circuit in parameter space (the space of nuclear shapes) and a corresponding Berry's phase, giving rise to fractional pseudorotation quantum numbers. (Adapted from *Annu. Rev. Phys. Chem.*, **41**, 601 (1990).)

dorotation as shown in fig. 9.11. Within the Born-Oppenheimer approximation, the wave function can be written

$$|\psi\rangle = |\psi_{\text{electronic}}\rangle \otimes |\psi_{\text{nuclear}}\rangle \tag{9.26}$$

with $|\psi_{\text{electronic}}\rangle$ following the nuclear configuration adiabatically:

$$|\psi_{\text{electronic}}\rangle = |\psi_{\text{electronic}}(\theta)\rangle\,, \tag{9.27}$$

where θ is the pseudorotation angle. The pseudorotation angle can be considered the external coordinate, and the phase of the electronic wave function the internal coordinate, in analogy to the quantum mechanics of a spin $I = 1/2$ adiabatically following a magnetic field. The geometry is that of a 2π circuit in the plane about a monopole (since we are restricted to the plane) of strength $1/2$ and associated geometric phase factor -1. *Thus the nuclear pseudorotation must be quantized over a 4π circuit*, leading to a pseudorotation quantum number J which is half-integer rather than the normal integer quantum number associated with rotation. This observation is borne out by more closely spaced lines in the optical spectroscopy of Na_3 [204]

9·9. *Nonunitary behavior, quantum projection.* – As we mentioned in subsect. 9·7, the evolution of $|\psi\rangle$ does not necessarily have to be unitary to give rise to a geometric phase. Indeed, PANCHARATNAM [219] considered two states $|\psi_1\rangle$ and $|\psi_2\rangle$ in which, for example, $|\psi_2\rangle$ may be obtained from $|\psi_1\rangle$ by means of some projection or filtering. A natural way to compare the phases of $|\psi_1\rangle$ and $|\psi_2\rangle$ is by means of the inner product:

$$\langle\psi_1|\psi_2\rangle = r\exp[i\alpha]. \tag{9.28}$$

The vectors $|\psi_1\rangle$ and $|\psi_2\rangle$ are said to be in phase or parallel if $\alpha = 0$, so $\langle\psi_1|\psi_2\rangle$ is real. SAMUEL and BHANDARI [220] point out that $|\psi_1\rangle$ and $|\psi_2\rangle$ are parallel if $|\psi_2\rangle$ is obtained from $|\psi_1\rangle$ (aside from any nonunitary shrinkage) by transport of the associated density operator along a geodesic in the projective space, the Pancharatnam connection. In the limit of unitary evolution this connection reduces to the adiabatic connection.

As an example of the Pancharatnam phase consider a sequence of (perhaps quantum) filtering measurements on spin $I = 1/2$ particles, as illustrated schematically in fig. 9.4. A beam of particles originally polarized along z with initial state vector $|z\rangle$ is split into a reference channel and a second beam. The second beam enters a Stern-Gerlach apparatus oriented along x and splits into two orthogonal components ($|x\rangle$ and $|\bar{x}\rangle$):

$$|\psi_{\text{initial}}\rangle = |z\rangle = |x\rangle\langle x|z\rangle + |\bar{x}\rangle\langle\bar{x}|z\rangle. \tag{9.29}$$

The $|\bar{x}\rangle$ component is discarded, leaving the filtered component $|x\rangle\langle x|z\rangle$ which is in phase with the original state ($\langle z|x\rangle\langle x|z\rangle = 1/2$ is real). Thus the filtering or projection from $|z\rangle$ to $|x\rangle$ is consistent with parallel transport (together with a shrinkage by $1/2$ and ignoring any dynamical phases) along a geodesic from z to x of the type shown in fig. 9.4. Following the geometry of the geodesic connections in fig. 9.4, the beam now enters a Stern-Gerlach apparatus oriented along y (in which the $|\bar{y}\rangle$ component is discarded) and finally a Stern-Gerlach [221] apparatus oriented along z (in which the $|\bar{z}'\rangle$ component is discarded). The final beam has the same polarization as the original beam (and $1/8$ the intensity), and its state is given by

$$|\psi_{\text{final}}\rangle = |z'\rangle\langle z'|y\rangle\langle y|x\rangle\langle x|z\rangle. \tag{9.30}$$

Although $|z\rangle$ is in phase with $|x\rangle$, $|x\rangle$ is in phase with $|y\rangle$, and $|y\rangle$ is in phase with $|z'\rangle$, it is clear that $|z\rangle$ and $|z'\rangle$ are not in phase; they differ by an holonomy

$$|z'\rangle = \exp[i\gamma(C)]|z\rangle, \tag{9.31}$$

where

$$\gamma(C) = -\frac{1}{2}\Omega(C) = -\frac{\pi}{4}\,. \tag{9.32}$$

The Pancharatnam phase is thus just Berry's phase for the geodesic triangle and it can be measured by interference with the original beam (whose phase is on record in the reference channel). Note that the limit of a continuous (densely spaced circuit) of quantum filtering measurements is equivalent to unitary evolution along the circuit, and in this limit the Pancharatnam phase reduces to the unitary geometric phase of subsect. 9'4.

9'10. *Geometry of light.* – The same result as that described for the Stern-Gerlach-type experiments can be obtained from a circuit of polarizations of light. As shown in fig. 9.12, a beam of light which is initially circularly polarized is passed through a polarizer so that it is subsequently linearly polarized along z, a second polarizer polarizes the light along x, and a final polarizer returns the light to circular polarization. As can be appreciated from the Poincaré sphere of fig. 9.3, such a circuit of polarizations is exactly analogous to the example of the Stern-Gerlach experiments given above, and gives rise to a phase shift of the light corresponding to a monopole $m = 1/2$ given by the expression in eq. (9.32).

A slightly different situation applies to a circuit of *directions* of light (fig. 9.12). For example, a circuit in the directions of propagation of light guided by mirrors or an optical fiber. In this case the light behaves as a particle of spin $I = 1$, and parallel transport of, say, polarized neutrons around, for example, an optical fiber along one of the trajectories shown in fig. 9.12 results in an accumulated geometric phase [222, 223]

$$\gamma(C) = -\Omega(C)\,,$$

corresponding to a monopole $m = 1$.

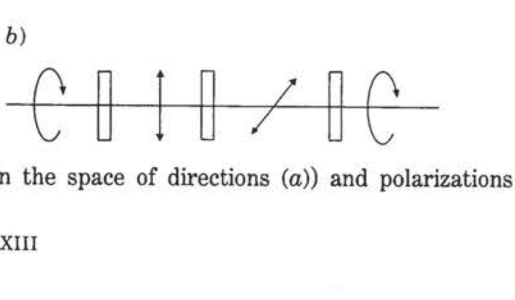

Fig. 9.12. – Circuits in the space of directions (a)) and polarizations (b)) of light.

9·11. *Rotation of cats.* – The acrobatics of a falling cat may seem a far cry from the preceding discussions of spins, light and molecules, but they share a lot in common and present a beautiful example of holonomy and gauge symmetry. Consider the falling cat of fig. 9.13 beginning with its feet up and maneuvering to land with its feet down. Since there are no external torques, angular momentum must be conserved and the cat cannot just «turn itself upside down»; its only recourse is to change its shape. In fact, if the cat begins and ends with the same shape, the «canonical cat shape», it has executed a circuit in its space of (unoriented) shapes. The question is, what is the angle of rotation of the cat given the circuit of shapes? The question is entirely analogous to those we have treated in previous sections: if we expand the cat shape in spherical harmonics, the coefficients can be considered external coordinates, the space of shapes is the base space, the orientation of the cat comprises the internal coordinates, and the gauge potential connects reference orientations for each of the shapes. SHAPERE and WILCZEK[206] and MONTGOMERY[207] have shown that for a deformable body the angle of rotation is the holonomy of the gauge potential over the circuit of shapes. In general the holonomy is non-Abelian, but a

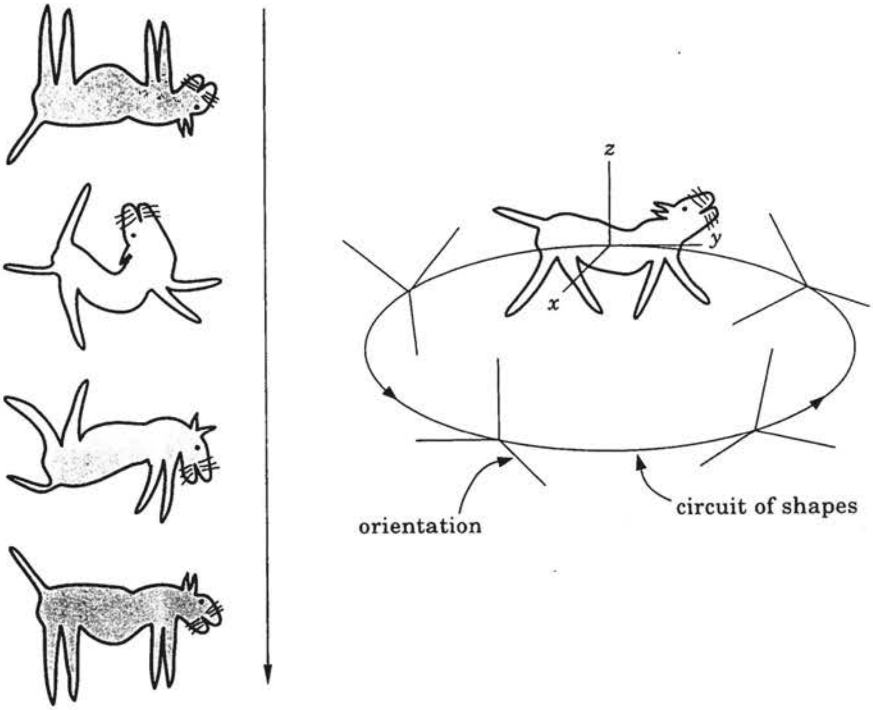

Fig. 9.13. – The reorientational dynamics of a falling cat can be treated by dividing the system into the external coordinates determining the shape of the cat, and the internal coordinates determining the orientation of the cat. In the absence of external torques, the cat can only land on its feet by reorientating through a sequence of shapes. The angle of rotation is the holonomy over the circuit of shapes.

simple Abelian example, the ~~binary cat (~~following BHANDARI [205]), illustrates the essence of the problem.

The simplest approximation to the cat shape is a rigid sphere or cylinder, which obviously cannot reorient. The next approximation is the binary cat, shown in fig. 9.14, two cylinders joined with muscle fibers allowing *two degenerate bends*; the shape space of this construction corresponds to the surface of a sphere, as shown in fig. 9.14, and the problem is identical to the case of classical holonomy of subsect. 9·2. The angle of rotation is equal to the area enclosed by the circuit swept out on the surface of a unit sphere by a vector on one of the binary-cat cylinders.

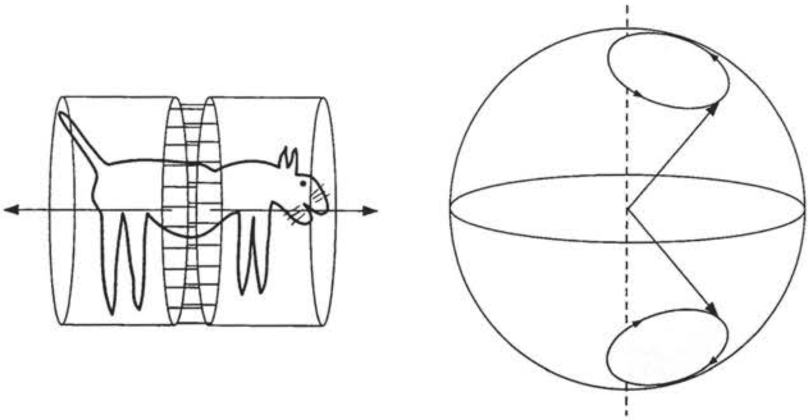

Fig. 9.14. – The binary cat, approximated by two rigid cylinders allowing two degenerate bends, has two external coordinates corresponding to the surface of a sphere. The angle of rotation of the binary cat is the solid angle subtended by the circuit of the cylinder vector at the origin, in analogy to the quantum holonomy of a spin $I = 1$ (Adapted from *Phys. Lett. A*, **133**, 1 (1988).)

A quantum version of the binary cat that corresponds to the classical behavior can be modeled by taking each half (cylinder) of the cat as a spin $I = 1$. Adopting a three-component spinor representation of the spin $I = 1$ [224], we have in the pole gauge for the base space

$$|\tilde{\Psi}\rangle_+ = \begin{pmatrix} \cos^2\dfrac{\theta}{2}\exp[-i\phi] \\ \sqrt{2}\sin\dfrac{\theta}{2}\cos\dfrac{\theta}{2} \\ \sin^2\dfrac{\theta}{2}\exp[+i\phi] \end{pmatrix}, \tag{9.33}$$

from which we calculate the gauge potential

$$A = -i\langle\tilde{\Psi}\,|\,\mathrm{d}\tilde{\Psi}\rangle = \cos\theta\,\mathrm{d}\phi \tag{9.34}$$

and the curvature

$$dA = -\sin\theta\, d\theta \wedge d\phi\,. \tag{9.35}$$

The geometric phase is the angle of rotation of the cat and is given by

$$\gamma = \oint_C dA = -\Omega(C) \tag{9.36}$$

exactly equal to the area of the circuit, as mentioned in subsect. **9·2** and corresponding to the case of a monopole of strength $m = 1$ in subsect. **9·6**. Indeed, binary cats are appreciative of the gauge kinematics, and they tend to execute essentially circular trajectories in the space of shapes in order to maximize the flux of curvature through a given length of circuit.

* * *

We should like to thank the group in Berkeley for providing the stimulating atmosphere in which these lectures were prepared. We are grateful to PH. J. GRANDINETTI, A. C. KOLBERT, Y. K. LEE, J. R. SACHLEBEN, J. SHORE and K. SCHMIDT-ROHR for comments on the second edition manuscript. We should also like to thank Prof. M. H. LEVITT and A. G. REDFIELD for their comments. We are also grateful to P. CARLSON and D. CARMICHAEL for invaluable assistance in the preparation of the manuscript and figures. This work was supported by the Miller Institute for Basic Research in Science, and the Director, Office of Energy Research, Office of Basic Energy Sciences, Materials Sciences Division of the U.S. Department of Energy under Contract No. DE-AC03-76SF00098.

REFERENCES

[1] A. PINES: in *Proc. S.I.F.*, Course C (North-Holland, Amsterdam, 1988), p. 43.
[2] A. ABRAGAM: *Principles of Nuclear Magnetism* (Clarendon Press, Oxford, 1961).
[3] C. P. SLICHTER: *Principles of Nuclear Magnetic Resonance*, 3rd edition (Springer-Verlag, New York, N.Y., 1990).
[4] M. MEHRING: *High Resolution NMR in Solids* (Springer-Verlag, New York, N.Y., 1983).
[5] R. R. ERNST, G. BODENHAUSEN and A. WOKAUN: *Principles of Nuclear Magnetic Resonance in One and Two Dimensions* (Clarendon Press, Oxford, 1987).
[6] G. E. PAKE: *J. Chem. Phys.*, **16**, 327 (1948).
[7] F. CREUZET, A. MCDERMOTT, R. GEBHARD, K. VANDER HOEF, M. B. SPIJKER-ASSIAK, J. HERZFELD, J. LUGTENBERG, M. H. LEVITT and R. G. GRIFFIN: *Science*, **251**, 783 (1991).
[8] J. H. OK, R. G. S. SPENCER, A. E. BENNET and R. G. GRIFFIN: *Chem. Phys. Lett.*, **197**, 389 (1992).
[9] A. SAUPE: *Z. Naturforsch., Teil A*, **20**, 572 (1965).

[10] P. DIEHL and C. L. KHETRAPAL: *NMR Basic Principles and Progress*, **1**, 1 (1969).
[11] W. S. WARREN, D. P. WEITEKAMP and A. PINES: *J. Chem. Phys.*, **73**, 2084 (1980).
[12] S. YATSIV: *Phys. Rev.*, **113**, 1522 (1959).
[13] W. A. ANDERSON, R. FREEMAN and C. A. REILLEY: *J. Chem. Phys.*, **39**, 1518 (1963).
[14] J. I. MUSHER: *J. Chem. Phys.*, **40**, 983 (1964).
[15] G. BODENHAUSEN: *Prog. NMR Spectrosc.*, **14**, 137 (1981).
[16] D. WEITEKAMP: *Adv. Magn. Reson.*, **11**, 111 (1983).
[17] M. MUNOWITZ and A. PINES: *Science*, **233**, 525 (1986).
[18] M. MUNOWITZ and A. PINES: *Adv. Chem. Phys.*, **57**, 1 (1987).
[19] J. JEENER: in *Ampère International Summer School*, Basko Polje, Yugoslavia, 1971.
[20] W. G. BREILAND, C. B. HARRIS and A. PINES: *Phys. Rev. Lett.*, **30**, 158 (1973).
[21] J. B. MURDOCH, W. S. WARREN, D. P. WEITEKAMP and A. PINES: *J. Magn. Reson.*, **60**, 205 (1984).
[22] U. FANO: *Rev. Mod. Phys.*, **29**, 74 (1957).
[23] R. BALIAN: *From Microphysics to Macrophysics* (Springer-Verlag, Paris, 1991).
[24] J. JENEER: *Adv. Magn. Reson.*, **10**, 2 (1982).
[25] F. DYSON: *Phys. Rev.*, **75**, 486 (1949).
[26] I. J. LOWE and R. E. NORBERG: *Phys. Rev.*, **107**, 46 (1957).
[27] S. VEGA and A. PINES: *J. Chem. Phys.*, **66**, 5624 (1977).
[28] A. WOKAUN and R. R. ERNST: *J. Chem. Phys.*, **67**, 1752 (1977).
[29] S. VEGA: *J. Chem. Phys.*, **68**, 5518 (1978).
[30] O. W. SØRENSEN, G. W. EICH, M. H. LEVITT, G. BODENHAUSEN and R. R. ERNST: *Prog. NMR Spectrosc.*, **16**, 163 (1983).
[31] K. J. PACKER and K. M. WRIGHT: *Mol. Phys.*, **50**, 797 (1983).
[32] F. J. M. VAN DER VEN and C. W. HILBERS: *J. Magn. Reson.*, **54**, 512 (1983).
[33] H. KESSLER, M. GEHRKE and C. GRIESINGER: *Angew. Chem., Int. Ed. Engl.*, **27**, 490 (1988).
[34] B. C. SANCTUARY: *J. Chem. Phys.*, **64**, 4352 (1976).
[35] R. G. GORDON: *Adv. Magn. Reson.*, **3**, 1 (1968).
[36] E. L. HAHN: *Phys. Rev.*, **80**, 580 (1950).
[37] J. BAUM, M. MUNOWITZ, A. N. GARROWAY and A. PINES: *J. Chem. Phys.*, **83**, 2015 (1985).
[38] D. N. SHYKIND, J. BAUM, S.-B. LIU, A. PINES and A. N. GARROWAY: *J. Magn. Reson.*, **76**, 149 (1988).
[39] G. DROBNY, A. PINES, S. SINTON, D. P. WEITEKAMP and D. WEMMER: *Faraday Symp. Chem. Soc.*, **13**, 49 (1979).
[40] G. BODENHAUSEN, R. L. VOLD and R. R. VOLD: *J. Magn. Reson.*, **37**, 93 (1980).
[41] H. HATANAKA, T. TERAO and T. HASHI: *J. Phys. Soc. Jpn.*, **39**, 835 (1975).
[42] H. HATANAKA and T. HASHI: *J. Phys. Soc. Jpn.*, **39**, 1139 (1975).
[43] E. L. HAHN: in *Ampère International Summer School II, Pulsed Magnetic and Optical Resonance*, Basko Polje, Yugoslavia, 1971.
[44] R. MCNAMARA, C. H. WU and S. J. OPELLA: *J. Magn. Reson.*, **100**, 559 (1992).
[45] E. L. HAHN: *NMR Basic Principles and Progress*, **13**, 31 (1976).

[46] M. GOCHIN, K. V. SCHENKER, H. ZIMMERMAN and A. PINES: *J. Am. Chem. Soc.*, **108**, 6813 (1986).

[47] G. CELEBRE, G. DELUCA, M. LONGERI and J. W. EMSLEY: *J. Phys. Chem.*, **96**, 2466 (1992).

[48] L. DIBARI, M. PERSICO and C. A. VERACINI: *J. Chem. Phys.*, **96**, 4782 (1992).

[49] B. F. CHMELKA, J. G. PEARSON, S. B. LIU, R. RYOO, L. C. DE MENORVAL and A. PINES: *J. Phys. Chem.*, **95**, 303 (1991).

[50] J. BAUM, K. K. GLEASON, A. PINES, A. N. GARROWAY and J. REIMER: *Phys. Rev. Lett.*, **56**, 1377 (1986).

[51] D. H. LEVY and K. K. GLEASON: *J. Phys. Chem.*, **96**, 8125 (1992).

[51bis] S. LACELLE: *Adv. Magn. Opt. Res.*, **16**, 173 (1991).

[52] M. MUNOWITZ, M. MEHRING and A. PINES: *J. Chem. Phys.*, **86**, 3172 (1987).

[53] B. E. SCRUGGS and K. K. GLEASON: *Chem. Phys.*, **166**, 367 (1992).

[54] B. E. SCRUGGS and K. K. GLEASON: *J. Magn. Reson.*, **99**, 149 (1992).

[55] D. P. WEITEKAMP, J. R. GARBOW, J. B. MURDOCH and A. PINES: *J. Am. Chem. Soc.*, **103**, 3578 (1981).

[56] M. GOCHIN, D. P. WEITEKAMP and A. PINES: *J. Magn. Reson.*, **63**, 431 (1985).

[57] J. R. GARBOW, D. P. WEITEKAMP and A. PINES: *Chem. Phys. Lett.*, **93**, 504 (1982).

[58] A. BAX: *J. Magn. Reson.*, **53**, 517 (1983).

[59] U. HAEBERLEN: *High Resolution NMR in Solids: Selective Averaging, Advances in Magnetic Resonance, Supplement 1* (Academic, New York, N.Y., 1976).

[60] W. MAGNUS: *Commun. Pure Appl. Math.*, **7**, 649 (1954).

[61] J. H. VAN VLECK: *Phys. Rev.*, **33**, 467 (1929).

[62] N. BLOEMBERGEN, E. M. PURCELL and V. POUND: *Phys. Rev.*, **73**, 679 (1948).

[63] M. GOLDMAN, P. J. GRANDINETTI, A. LLOR, Z. OLEJNICZAK and J. R. SACHLEBEN: *J. Chem. Phys.*, **97**, 8947 (1992).

[64] M. H. LEVITT: *Prog. NMR Spectrosc.*, **18**, 61 (1986).

[65] A. J. SHAKA and J. KEELER: *Prog. NMR Spectrosc.*, **19**, 47 (1987).

[66] R. TYCKO: *Phys. Rev. Lett.*, **51**, 775 (1983).

[67] R. TYCKO, J. GUCKENHEIMER and A. PINES: *J. Chem. Phys.*, **83**, 2775 (1985).

[68] J. S. WAUGH: *J. Magn. Reson.*, **49**, 517 (1982).

[69] Y. S. YEN and A. PINES: *J. Chem. Phys.*, **78**, 3579 (1983).

[70] H. Y. CARR and E. M. PURCELL: *Phys. Rev.*, **94**, 630 (1954).

[71] E. R. ANDREW, A. BRADBURY and R. G. EADES: *Nature (London)*, **182**, 1659 (1958).

[72] E. O. STEJSKAL, J. SCHAEFER and R. A. MCKAY: *J. Magn. Reson.*, **25**, 569 (1977).

[73] J. S. WAUGH, L. M. HUBER and U. HAEBERLEN: *Phys. Rev. Lett.*, **20**, 180 (1968).

[74] C. H. WANG and J. D. RAMSHAW: *Phys. Rev. B*, **6**, 3253 (1972).

[75] P. MANSFIELD: *Phys. Lett. A*, **32**, 485 (1970).

[76] P. MANSFIELD: *J. Phys. C*, **4**, 1444 (1971).

[77] W. K. RHIM, D. D. ELLEMAN and R. W. VAUGHAN: *J. Chem. Phys.*, **58**, 1772 (1972).

[78] D. P. BURUM, M. LINDER and R. R. ERNST: *J. Magn. Reson.*, **44**, 173 (1981).

[79] D. P. BURUM and W. K. RHIM: *J. Chem. Phys.*, **71**, 944 (1979).

[80] D. G. CORY: *J. Magn. Reson.*, **94**, 526 (1991).

[81] C. A. FYFE: *Solid State NMR for Chemists* (CFC Press, Guelph, Ont., 1983).

[82] B. C. GERSTEIN and C. R. DYBOWSKI: *Transient Techniques in NMR of Solids* (Academic Press, Orlando, Fla., 1985).

[83] M. M. MARICQ and J. S. WAUGH: *J. Chem. Phys.*, **70**, 3300 (1979).
[84] S. F. DEC, R. A. WIND, G. E. MACIEL and F. E. ANTHONIO: *J. Magn. Reson.*, **70**, 355 (1986).
[85] J. ACKERMAN, R. ECKMAN and A. PINES: *Chem. Phys.*, **42**, 423 (1979).
[86] H. J. JAKOBSEN, J. SKIBSTED, H. BILDSØE and N. C. NIELSEN: *J. Magn. Reson.*, **85**, 173 (1989).
[87] R. K. HARRIS and P. JACKSON: *Chem. Rev.*, **91**, 1427 (1991).
[88] A. JURKIEWICZ, C. E. BRONNIMAN and G. E. MACIEL: *Fuel*, **69**, 804 (1990).
[89] S. GANAPATHY, S. SCHRAMM and E. OLDFIELD: *J. Chem. Phys.*, **77**, 4360 (1982).
[90] S. GANAPATHY, J. SHORE and E. OLDFIELD: *Chem. Phys. Lett.*, **169**, 301 (1990).
[91] B. F. CHMELKA and A. PINES: *Science*, **246**, 71 (1989).
[92] A. LLOR and J. VIRLET: *Chem. Phys. Lett.*, **152**, 248 (1988).
[93] A. SAMOSON, E. LIPPMAA and A. PINES: *Mol. Phys.*, **65**, 1013 (1988).
[94] B. Q. SUN, J. H. BALTISBERGER, Y. WU, A. SAMOSON and A. PINES: *Solid State NMR*, **1**, 267 (1992).
[95] Y. WU, B. F. CHMELKA, A. PINES, M. E. DAVIS, P. J. GROBET and P. A. JACOBS: *Nature (London)*, **346**, 6284 (1990).
[96] J. S. WAUGH: *J. Magn. Reson.*, **50**, 30 (1982).
[97] M. H. LEVITT and R. FREEMAN: *J. Magn. Reson.*, **43**, 502 (1981).
[98] M. H. LEVITT, R. FREEMAN and T. FRENKIEL: *J. Magn. Reson.*, **47**, 328 (1982).
[99] A. J. SHAKA, J. KEELER, T. FRENKIEL and R. FREEMAN: *J. Magn. Reson.*, **52**, 335 (1983).
[100] A. J. SHAKA, J. KEELER and R. FREEMAN: *J. Magn. Reson.*, **53**, 313 (1983).
[101] L. C. SNYDER and S. MEIBOOM: *J. Chem. Phys.*, **58**, 5096 (1973).
[102] A. PINES, D. J. RUBEN, S. VEGA and M. MEHRING: *Phys. Rev. Lett.*, **36**, 110 (1976).
[103] C. COHEN-TANNOUDJI, B. DIU and F. LALOË: *Quantum Mechanics* (Wiley, Paris, 1977).
[104] R. C. HEWITT, S. MEIBOOM and L. C. SNYDER: *J. Chem. Phys.*, **58**, 5089 (1973).
[105] J. W. EMSLEY, J. C. LINDON and J. M. TABONY: *J. Chem. Soc. Faraday Trans.*, **269**, 10 (1973).
[106] A. PINES, S. VEGA and M. MEHRING: *Phys. Rev. B*, **18**, 112 (1978).
[107] R. J. WITTEBORT, M. G. USHA, D. J. RUBEN, D. E. WEMMER and A. PINES: *J. Am. Chem. Soc.*, **110**, 5668 (1988).
[108] L. ALLEN and J. H. EBERLY: *Optical Resonance and Two-Level Atoms* (Wiley, New York, N.Y., 1975).
[109] R. P. FEYNMAN, F. L. VERNON and R. W. HELLWARTH: *J. Appl. Phys.*, 28, 49 (1957).
[110] E. T. JAYNES and F. W. CUMMINGS: *Proc. I.R.E.*, **51**, 89 (1963).
[111] J. J. SAKURAI: *Modern Quantum Mechanics* (Benjamin-Cummings, Menlo Park, Cal., 1985).
[112] W. H. LOUISELL: *Quantum Statistical Properties of Radiation* (Wiley, New York, N.Y., 1973).
[113] I. I. RABI, J. R. ZACHARIAS, S. MILLMAN and P. KUSH: *Phys. Rev.*, **53**, 318 (1938).
[114] Y. AHARONOV and L. SUSSKIND: *Phys. Rev.*, **158**, 1237 (1967).
[115] M. P. SILVERMAN: *Eur. J. Phys.*, **1**, 116 (1980).

[116] S. HAROCHE: *Ann. Phys. (N.Y.)*, **6**, 327 (1971).

[117] A. G. REDFIELD: *Adv. Magn. Reson.*, **1**, 1 (1965).

[118] J. BAUM, R. TYCKO and A. PINES: *Phys. Rev. A*, **32**, 3435 (1985).

[119] M. ALEXANDER: private communication.

[120] J. C. S. JOHNSON: *Adv. Magn. Reson.*, **1**, 223 (1965).

[121] A. HAGEMEYER, K. SCHMIDT-ROHR and H. W. SPIESS: *Adv. Magn. Reson.*, **13**, 85 (1989).

[122] P. RIGNY: *Physica*, **59**, 707 (1971).

[123] S. ALEXANDER, A. BARAM and Z. LUZ: *Mol. Phys.*, **27**, 441 (1974).

[124] A. BARAM, Z. LUZ and S. ALEXANDER: *J. Chem. Phys.*, **64**, 4321 (1976).

[125] D. E. WEMMER: Ph. D. Thesis, University of California, Berkeley, 1978.

[126] R. K. WANGSNESS and F. BLOCH: *Phys. Rev.*, **89**, 728 (1953).

[127] H. S. GUTOWSKY, D. W. MCCALL and C. P. SLICHTER: *J. Chem. Phys.*, **21**, 279 (1953).

[128] H. S. GUTOWSKY and C. HOLM: *J. Chem. Phys.*, **25**, 1228 (1956).

[129] H. M. MCCONNELL: *J. Chem. Phys.*, 28, 430 (1958).

[130] M. HAMMERMESH: *Group Theory and Its Application to Physical Problems* (Dover, New York, N.Y., 1962).

[131] L. G. WERBELOW and D. M. GRANT: *Adv. Magn. Reson.*, **9**, 189 (1977).

[132] D. E. WEMMER, D. J. RUBEN and A. PINES: *J. Am. Chem. Soc.*, **103**, 28 (1981).

[133] J. WANG and P. D. ELLIS: *J. Am. Chem. Soc.*, **115**, 212 (1993).

[134] R. D. JOHNSON, D. S. BETHUNE and C. S. YANNONI: *Acc. Chem. Res.*, **25**, 169 (1992).

[135] S. E. BARRETT and R. TYCKO: *Phys. Rev. Lett.*, **69**, 3754 (1992).

[136] P. J. STEINHARDT, D. R. NELSON and R. RONCHETTI: *Phys. Rev. B*, **28**, 784 (1983).

[137] A. BAX, N. M. SZEVERENYI and G. MACIEL: *J. Magn. Reson.*, **52**, 147 (1983).

[138] Z. H. GAN: *J. Am. Chem. Soc.*, **114**, 8307 (1992).

[139] K. T. MUELLER, A. SAMOSON, B. Q. SUN, G. C. CHINGAS, J. W. ZWANZIGER, T. TERAO and A. PINES: *J. Magn. Reson.*, **86**, 470 (1990).

[140] J. H. BALTISBERGER, S. L. GANN, E. W. WOOTEN, T. H. CHANG, K. T. MUELLER and A. PINES: *J. Am. Chem. Soc.*, **114**, 7489 (1992).

[141] A. BAX, N. M. SZEVERENYI and G. MACIEL: *J. Magn. Reson.*, **55**, 494 (1983).

[142] R. TYCKO, G. DABBAGH and P. A. MIRAU: *J. Magn. Reson.*, **85**, 265 (1989).

[143] I. FARNAN, P. J. GRANDINETTI, J. H. BALTISBERGER, J. F. STEBBINS, U. WERNER, M. A. EASTMAN and A. PINES: *Nature (London)*, 358, 31 (1992).

[144] R. DUPREE and R. F. PETTIFER: *Nature (London)*, **308**, 523 (1984).

[145] L. FRYDMAN, G. C. CHINGAS, Y. K. LEE, P. J. GRANDINETTI, M. A. EASTMAN, G. A. BARRALL and A. PINES: *J. Chem. Phys.*, **97**, 4800 (1992).

[146] L. FRYDMAN, Y. K. LEE, L. EMSLEY, G. C. CHINGAS and A. PINES: *J. Am. Chem. Soc.*, **115**, 4825 (1993).

[147] M. GOLDMAN: *Spin Temperature and Nuclear Magnetic Resonance in Solids* (Clarendon Press, Oxford, 1970).

[148] J. JEENER: *Adv. Magn. Reson.*, **3**, 205 (1968).

[149] S. R. HARTMANN and E. L. HAHN: *Phys. Rev.*, **128**, 2042 (1962).

[150] A. PINES, M. G. GIBBY and J. S. WAUGH: *J. Chem. Phys.*, **59**, 569 (1973).

[151] A. G. ANDERSON and S. R. HARTMANN: *Phys. Rev.*, **128**, 2023 (1962).

[152] M. H. LEVITT: in *Pulsed Magnetic Resonance: NMR, ESR, and Optics*, edited by D. M. S. BAGGULEY (Clarendon Press, Oxford, 1992), p. 184.

[153] M. H. LEVITT, D. SUTER and R. R. ERNST: *J. Chem. Phys.*, **84**, 4243 (1986).

[154] J. R. FRANZ and C. P. SLICHTER: *Phys. Rev.*, **148**, 287 (1966).

[155] L. MÜLLER, A. KUMAR, T. BAUMANN and R. R. ERNST: *Phys. Rev. Lett.*, **32**, 1402 (1974).

[156] O. W. SØRENSEN: *Prog. NMR Spectrosc.*, **21**, 503 (1989).

[157] N. C. NIELSEN, H. BILDSØE, H. J. JAKOBSEN and O. W. SØRENSEN: *J. Magn. Reson.*, **85**, 359 (1989).

[158] O. W. SØRENSEN: *J. Magn. Reson.*, **86**, 435 (1990).

[159] O. W. SØRENSEN: *J. Magn. Reson.*, **93**, 648 (1991).

[160] A. G. REDFIELD: *J. Magn. Reson.*, **92**, 642 (1991).

[161] M. H. LEVITT: *J. Magn. Reson.*, **99**, 1 (1992).

[162] G. STRANG: *Linear Algebra and its Applications*, 3rd edition (Harcourt Brace Jovanovich, San Diego, Cal., 1988).

[163] P. L. CORIO: *Structure of High-Resolution NMR Spectra* (Academic Press, New York, N.Y., 1966).

[164] R. L. VOLD and R. R. VOLD: *Prog. NMR Spectrosc.*, **12**, 79 (1978).

[165] T. P. DAS and E. L. HAHN: *Solid State Phys. Suppl.*, **1**, 18 (1958).

[166] N. F. RAMSEY and R. V. POUND: *Phys. Rev.*, **81**, 278 (1951).

[167] R. L. STROMBOTNE and E. L. HAHN: *Phys. Rev. A*, **133**, 1616 (1964).

[168] R. BLINC: *Adv. Nuc. Quad. Reson.*, **2**, 71 (1975).

[169] D. T. EDMONDS: *Phys. Rep.*, **29**, 233 (1977).

[170] D. P. WEITEKAMP, A. BIELECKI, D. ZAX, K. ZILM and A. PINES: *Phys. Rev. Lett.*, **50**, 1807 (1983).

[171] D. ZAX, A. BIELECKI, K. ZILM, A. PINES and D. P. WEITEKAMP: *J. Chem. Phys.*, **83**, 4877 (1985).

[172] J. W. HENNEL, A. BIRCZYNSKI, S. F. SAGNOWSKI and M. STACHUROWA: *Z. Phys. B*, **56**, 133 (1984).

[173] R. BLINC and J. SELIGER: *Z. Naturforsch.*, **47**, 333 (1992).

[174] A. M. THAYER and A. PINES: *Acc. Chem. Res.*, **20**, 47 (1987).

[175] J. M. MILLAR, A. M. THAYER, H. ZIMMERMAN and A. PINES: *J. Magn. Reson.*, **69**, 243 (1986).

[176] A. BIELECKI, J. B. MURDOCH, D. P. WEITEKAMP, D. B. ZAX, K. W. ZILM, H. ZIMMERMAN and A. PINES: *J. Chem. Phys.*, **80**, 2232 (1984).

[177] J. M. MILLAR, A. M. THAYER, A. BIELECKI, D. B. ZAX and A. PINES: *J. Chem. Phys.*, **83**, 934 (1985).

[178] C. CONNOR, J. W. CHANG and A. PINES: *J. Chem. Phys.*, **93**, 7639 (1990).

[179] D. ZAX, A. BIELECKI, A. PINES and S. W. SINTON: *Nature (London)*, **312**, 351 (1984).

[180] A. M. THAYER, J. M. MILLAR and A. PINES: *Chem. Phys. Lett.*, **129**, 55 (1986).

[181] R. KREIS, D. SUTER and R. R. ERNST: *Chem. Phys. Lett.*, **118**, 120 (1985).

[182] R. TYCKO: *J. Magn. Reson.*, **75**, 193 (1987).

[183] R. TYCKO: *Phys. Rev. Lett.*, **60**, 2734 (1988).

[184] R. TYCKO: *J. Chem. Phys.*, **192**, 5776 (1990).

[185] A. LLOR, Z. OLEJNICZAK, J. SACHLEBEN and A. PINES: *Phys. Rev. Lett.*, **67**, 1989 (1991).

[186] A. LLOR, Z. OLEJNICZAK and A. PINES: *Phys. Rev. B*, in press (1993).

[187] Y. A. SEREBRENNIKOV and M. I. MAJITOV: *Chem. Phys. Lett.*, **157**, 462 (1989); Y. A. SEREBRENNIKOV: *Adv. Magn. Reson.*, **17**, 47 (1992).

[188] P. JONSEN, M. LUZAR, A. PINES and M. MEHRING: *J. Chem. Phys.*, **85**, 4873 (1986).

[189] E. P. DAY: *Phys. Rev. Lett.*, **29**, 540 (1972).

[190] J. Chang, C. Connor, E. L. Hahn, H. Huber and A. Pines: *J. Magn. Reson.*, **82**, 387 (1989).

[191] C. Connor, J. Chang and A. Pines: *Rev. Sci. Instrum.*, **61**, 1059 (1990).

[192] M. D. Hurliman, C. H. Pennington, N. Q. Fan, J. Clarke, A. Pines and E. L. Hahn: *Phys. Rev. Lett.*, **69**, 684 (1992).

[193] M. V. Berry: *Proc. R. Soc. London, Ser. A*, **392**, 45 (1984).

[194] B. Simon: *Phys. Rev. Lett.*, **51**, 2167 (1983).

[195] Y. Aharonov and J. Anandan: *Phys. Rev. Lett.*, **58**, 1593 (1987).

[196] A. Shapere and F. Wilczek: *Geometric Phases in Physics* (World Scientific, Singapore, 1989).

[197] J. W. Zwanziger, M. Koenig and A. Pines: *Annu. Rev. Phys. Chem.*, **41**, 601 (1990).

[198] K. Moriyasu: *An Elementary Primer for Gauge Theory* (World Scientific, Singapore, 1983).

[199] N. Nash and S. Sen: *Topology and Geometry for Physicists* (Academic Press, London, 1983).

[200] Y. Aharonov and D. Bohm: *Phys. Rev.*, **115**, 485 (1959).

[201] R. P. Feynman, R. B. Leighton and M. Sands: *The Feynman Lectures on Physics* (Addison-Wesley, Reading, Mass., 1963).

[202] G. Herzberg and H. C. Longuet-Higgins: *Dicuss. Faraday Soc.*, **35**, 77 (1963).

[203] C. A. Mead and D. G. Truhlar: *J. Chem. Phys.*, **70**, 2284 (1979).

[204] G. Delacrétaz, E. R. Grant, R. L. Whetten, L. Wöste and J. W. Zwanziger: *Phys. Rev. Lett.*, **56**, 2598 (1986).

[205] R. Bhandari: *Phys. Lett. A*, **133**, 1 (1988).

[206] A. Shapere and F. Wilczek: *J. Fluid Mech.*, **198**, 557 (1987).

[207] R. Montgomery: *Commun. Math. Phys.*, **120**, 269 (1988).

[208] C. W. Misner, K. S. Thorne and J. A. Wheeler: *Gravitation* (W. H. Freeman and Co., New York, N.Y., 1973).

[209] H. Goldstein: *Classical Mechanics* (Addison-Wesley, Reading, Mass., 1950).

[210] G. Baym: *Lectures on Quantum Mechanics* (Benjamin-Cummings, Reading, Mass., 1973).

[211] F. Wilczek and A. Zee: *Phys. Rev. Lett.*, **52**, 2111 (1984).

[212] A. Zee: *Phys. Rev. A*, **38**, 1 (1988).

[213] R. Tycko: *Phys. Rev. Lett.*, **58**, 2281 (1987).

[214] C. N. Yang: *Ann. N.Y. Acad. Sci.*, **294**, 86 (1977).

[215] S. Coleman: *Les Houches 1981: Session 37 Gauge Theories in High Energy Physics* (North-Holland, Amsterdam, 1983).

[216] P. A. M. Dirac: *Proc. R. Soc. London, Ser. A*, **133**, 60 (1931).

[217] M. E. Stoll, A. G. Vega and R. W. Vaughan: *Phys. Rev. A*, **16**, 1521 (1977).

[218] D. Suter, A. Pines and M. Mehring: *Phys. Rev. Lett.*, **57**, 242 (1986).

[219] S. Pancharatnam: *Proc. Ind. Acad. Sci.*, **44**, 247 (1956).

[220] J. Samuel and R. Bhandari: *Phys. Rev. Lett.*, **60**, 2339 (1988).

[221] W. Gerlach and O. Stern: *Ann. Phys. (Leipzig)*, **74**, 673 (1924).

[222] R. Chiao and Y. Wu: *Phys. Rev. Lett.*, **57**, 933 (1986).

[223] R. Chiao, A. Antaramian, K. M. Ganga, H. Jiao, S. R. Wilkinson and H. Nathel: *Phys. Rev. Lett.*, **60**, 1214 (1988).

[224] C. Bouchiat and G. W. Gibbons: *J. Phys. Paris*, **49**, 187 (1988).